UNIVERSITY OF ALBERTA

Low-Noise Amplifier Design With Peltier Cooled HEMTs

by

Gavin Keith Miller

A THESIS
SUBMITTED TO THE FACULTY OF GRADUATE STUDIES AND RESEARCH IN PARTIAL FULFILLMENT OF THE REQUIREMENTS FOR THE DEGREE OF
Master of Science

Department of Electrical Engineering

EDMONTON, ALBERTA
Fall 1991

National Library
of Canada

Bibliothèque nationale
du Canada

Canadian Theses Service

Service des thèses canadiennes

Ottawa, Canada
K1A 0N4

The author has granted an irrevocable non-exclusive licence allowing the National Library of Canada to reproduce, loan, distribute or sell copies of his/her thesis by any means and in any form or format, making this thesis available to interested persons.

L'auteur a accordé une licence irrévocable et non exclusive permettant à la Bibliothèque nationale du Canada de reproduire, prêter, distribuer ou vendre des copies de sa thèse de quelque manière et sous quelque forme que ce soit pour mettre des exemplaires de cette thèse à la disposition des personnes intéressées.

The author retains ownership of the copyright in his/her thesis. Neither the thesis nor substantial extracts from it may be printed or otherwise reproduced without his/her permission.

L'auteur conserve la propriété du droit d'auteur qui protège sa thèse. Ni la thèse ni des extraits substantiels de celle-ci ne doivent être imprimés ou autrement reproduits sans son autorisation.

ISBN 0-315-69934-5

Canada

UNIVERSITY OF ALBERTA

RELEASE FORM

NAME OF AUTHOR Gavin Keith Miller

TITLE OF THESIS Low-Noise Amplifier Design with Peltier Cooled HEMTS

DEGREE FOR WHICH THESIS WAS PRESENTED Master of Science

YEAR THIS DEGREE WAS GRANTED Fall 1991

Permission is hereby granted to the UNIVERSITY OF ALBERTA LIBRARY to reproduce single copies of this thesis and to lend or sell such copies for private, scholarly or scientific research purposes only.

The author reserves other publication rights, and neither the thesis nor extensive extracts from it may be printed or otherwise reproduced without the author's written permission.

(SIGNED) Gavin Miller

ADDRESS:

805, 10155 - 116 st.
Edmonton, AB
Canada T5K 1W2

DATED Sept. 24, 1991

UNIVERSITY OF ALBERTA

FACULTY OF GRADUATE STUDIES AND RESEARCH

The undersigned certify that they have read, and recommend to the Faculty of Graduate Studies and Research, for acceptance, a thesis entitled Low-Noise Amplifier Design with Peltier Cooled HEMTs submitted by Gavin Keith Miller in partial requirements for the degree of Master of Science.

J Vaneldik
....
Co-Supervisor

Thomas Landecker
....
Co-Supervisor

D. Routledge
....

R. Vermeulen
....

....

Date 10th September 1991

Abstract

The development of a low noise amplifier (LNA) employing the concept of cooling only the critical components, as opposed to bulk cooling, is the focus of this thesis. The design incorporates high electron mobility transistors (HEMTs) and a Peltier device for refrigeration. It was shown that integration of the thermal and electrical designs produced substantial improvement in LNA performance, even with only moderate cooling.

A FORTRAN program was developed to assist in proper selection of transistor terminations and feedback conditions. This program was employed in conjunction with a microwave circuit design package, Touchstone®, to produce the RF design of the LNA. A thermal analysis was carried out to minimize the refrigerator heat load. An LNA enclosure was produced to meet both the thermal and RF requirements of the amplifier.

Severe stability problems were encountered with the HEMTs. In order to overcome these problems it was necessary to make modifications which compromised the thermal design. The LNA did not meet the objective noise temperature. It did, however, demonstrate that the new concept of cooling only particular components in an LNA was possible and that large gains in performance could be achieved without cryogenic refrigeration. The ultimate cold temperature

achieved by the HEMT was 225 Kelvin. This 25% decrease in physical temperature corresponded with an approximate 25% decrease in HEMT noise temperature.

There are several alternate approaches to this LNA design for possible use in future projects of this nature. These approaches include the use of Joule-Thompson refrigeration, cooling of multiple LNAs with a single refrigerator, and possible means of improving LNA stability.

The concepts investigated herein show tremendous potential for use in radio-telescopes employing multiple antennas and receivers. Peltier cooling of only the critical components allows for LNAs which are cheaper, lighter, and easier to maintain than the conventional, bulk cryogenically cooled LNAs.

Acknowledgements

The author would like express his gratitude to his supervisors, Dr. D. Routledge, Dr. F. Vaneldik, and Dr. T.L. Landecker for their advice, encouragement, and financial support. The author also wishes to thank Dr. F. Vermuelen and Dr. G. S. H. Lock for serving on the examining committee. The financial support provided by NSERC and the Department of Electrical Engineering is also deeply appreciated.

This project was carried out with the technical assistance of many people who the author wishes to give his sincere thanks; R. Schmaus for his assistance in the laboratory, B. Arnold for his work in the optics shop, R. Lipiecki for his excellent machining, and G. Mckinnon and Y. Loke for their generous assistance at the Alberta Microelectronics Centre. The author would also like to thank H. Johansen and Dr. E. Valk for their many helpful discussions and suggestions.

The author sincerely thanks his parents, family and friends for their support and encouragement. The author would especially like to thank his fiancee, S. Treasure, for her love, patience, and encouragement, without whom this project would never have been completed.

TABLE OF CONTENTS

Chapter Page

1. Introduction

1.0 Introduction 1

1.1 Overview of Current LNA Technology 1

1.2 Goals of this Thesis 3

2. LNA Design Theory and Technique

2.0 Introduction 8

2.1 Radio-telescope Sensitivity 9

2.2 Noise in Two-Port Networks 15

2.3 High Electron Mobility Transistors 20

2.4 RF Design Theory 23

2.4.1 Gain Definitions 26

2.4.2 Stability 27

2.4.3 Source Inductive Feedback 31

2.4.4 Design Procedure 35

2.5 Initial RF Design 39

2.6 Conclusions 44

3. Thermal Integration and LNA Fabrication

3.0 Introduction 45

3.1 Thermoelectricity 45

3.2 Thermal Model 60

3.2.1 HEMT Carrier Design 63

3.2.2 Conduction Heat Load 74

3.2.3 Convection Heat Load 77

3.2.4 Radiation Heat Load 82
3.2.5 Total Heat Load 84
3.3 LNA Enclosure Design 85
3.4 Conclusions 88

4. Results

4.0 Introduction 89
4.1 Noise Measurement Theory 89
4.2 S-Parameter Test-Set 91
4.3 Modified L-Band LNA 93
4.4 LNA with Peltier Cooled First Stage 95
4.4.1 Second and Third Stage Testing 96
4.4.2 First Stage Testing 101
4.4.3 Discussion 125
4.5 Conclusions 127

5. Future LNA Development

5.0 Introduction 129
5.1 Future LNA Development with Peltier Cooling 129
5.1.1 Problems with this Project 130
5.1.2 Hybrid LNA Design 131
5.1.3 Alternative Source Impedance 133
5.2 Joule-Thompson Cooling in LNA Design 134
5.3 Cooling Multiple LNAs with a Single Refrigerator 137
5.4 Thermal Insulation with RF Conduction 138
5.5 Conclusion 140
6. Conclusions 142

References 145

Appendices

1.1 LNA Design Program Listing 150

1.2 LNA Design Program Output Data 156

2.1 Procedure for Etching Gold Pattern on Quartz 162

List of Tables

Table		page
2.1	System noise temperature breakdown for DRAO synthesis telescope at L-band.	15
3.2.1.1	Thermal and electrical properties of various dielectrics.	65
3.2.2.1	Gate, source, and drain inductor lengths and associated thermal resistances.	76
3.2.3.1	Mean free path of air for various pressures.	78
4.4.2.1	Some possible resonant cavity modes in the LNA enclosure and their associated frequencies.	108
4.4.2.2	1420MHz S-parameter measurements with externally tuned LNA.	119
4.4.2.3	1420MHz noise temperatures and gains of externally tuned LNA and associated components.	120

List of Figures

Figure		Page
1.1	Noise temperatures of various devices versus frequency including natural limits.	3
2.1.1	Typical Superheterodyne radiotelescope receiver.	13
2.2.1	Model of noisy two-port.	17
2.2.2	Noise figure of cascaded two-ports.	19
2.3.1	Structure of the HEMT.	21
2.4.1	Scattering Matrix representation of a two-port network.	25
2.4.3.1	Equivalent circuit for NE32000 HEMT with external source inductance.	33
2.4.3.2	NE32000 HEMT normalized input impedance (z_{in}) with varying source inductance (L_s).	33
2.4.3.3	Effect of source lead inductance on stability circles at 1.4GHz for NE32000 HEMT (as shown on normalized impedance plots).	34
2.4.4.1	Flowchart for LNA design program.	38
2.5.1	Three stage LNA block diagram.	40
2.5.2	L-band LNA schematic.	42
2.5.3	LNA performance obtained from Touchstone®.	43
3.1.1	Simple thermoelectric circuit.	47
3.1.2	Simple thermoelectric refrigerator.	49
3.1.3	One branch of thermoelectric refrigerator.	50
3.1.4	Variation of thermoelectric figure of merit with temperature for various materials.	55
3.1.5	Typical cascaded thermoelectric refrigerator.	57

3.1.6 Temperature difference (ΔT) versus current of Marlow MI6030 6 stage refrigerator for various heat loads. 59

3.2.1 Heat loading on Peltier device. 61

3.2.1.1 Initial evaporation technique. 68

3.2.1.2 Modified evaporation technique. 69

3.2.1.3 Thermal blocking input capacitor. 70

3.2.1.4 Physical layout of NE32000 chip HEMT. 72

3.2.1.5 Mask for quartz HEMT carrier with HEMT and bonding wire postions. 72

3.2.1.6 Mask for 9 quartz HEMT carriers. 73

3.2.3.1 Peltier device test in Bell jar. 80

3.2.3.2 Peltier device temperature differential versus pressure. 81

3.2.4.1 HEMT carrier surrounded by LNA enclosure. 83

3.3.1 Cross-section of L-band LNA enclosure. 86

4.1.1 Noise temperature measurement using the hot/cold source technique. 90

4.1.2 Typical noise measurement configuration. 91

4.2.1 S-parameter measurement system. 92

4.3.1 LNA noise and gain measurement configuration. 93

4.3.2 Measured gain and noise temperature of DRAO L-band LNA. 94

4.4.1.1 Printed circuit layout of second and third LNA stages. 97

4.4.1.2 Schematic of second and third LNA stages. 97

4.4.1.3 Stages 2 and 3 test configuration. 100

4.4.1.4 Measured and predicted gain and noise temperature of second and third LNA stages. 101

4.4.2.1 Printed circuit layout of input tuning circuit and associated components. 102

4.4.2.2 Test to determine if first stage HEMT is tuned to Γ_{opt}. 105

4.4.2.3 Impedance of source inductance in parallel with various RC bypass networks. 106

4.4.2.4 Parasitic capacitive coupling between HEMT drain and gate. 110

4.4.2.5 Reduction of extrinsic gate-to-drain coupling. 112

4.4.2.6 Space blanket between Peltier device and HEMT carrier. 114

4.4.2.7 Thermal mounting of LNA. 115

4.4.2.8 Test configuration for optimizing input tuning network. 117

4.4.2.9 Dual realizations of input tuning network for source reflection coefficient equal to Γ_{opt}. 121

4.4.2.10 Test configuration for first stage LNA with internal tuning network. 122

4.4.2.11 LNA S-parameters at 300K and at 225K. 123

4.4.2.12 Available gain and noise temperature for LNA first stage with HEMT at 300K and 225K. 124

4.4.2.13 Noise temperature improvement due to cooling as measured and predicted by Pospieszalski [5] and Mochizuki [6]. 125

5.2.1 Temperature-entropy diagram for Joule-Thompson effect with precooling. 135

5.3.1 Cooling of multiple LNAs with single refrigerator. 138

Chapter 1

1.0 Introduction

In radioastronomy the signals received by the radio-telescope are very weak. The receiver performance is a very important factor in determining the overall sensitivity, or ability to detect weak signals, of the telescope. The front-end of the receiver, usually a low-noise amplifier (LNA), is the component of the receiver which has the most effect on its sensitivity. Therefore, since the beginnings of radioastronomy around fifty years ago, a great deal of effort has been expended in the improvement of LNA technology and performance. As a result, radioastronomy has served as a leader in this technology which can also be applied to satellite communications, radar, terrestrial communications, and military applications.

1.1 Overview of Current LNA Technology

There is a vast number of technologies available today in the design of receiver front-ends. Since the radio spectrum used in radioastronomy stretches from a few megahertz up to hundreds of gigahertz , it is not surprising that one particular technology is not suitable for all applications. Below about 500 MHz bipolar junction transistors are generally used because in that range, noise produced by background galactic radiation dominates over any noise produced by the receiver itself. Above 40 GHz, Schottky and superconductor-insulator-superconductor (SIS) mixers are normally used. However, this lower frequency is continually being pushed up due to improvements in transistor technology. Between 500 MHz and 40 GHz, where galactic emission is at a minimum, the greatest variety of LNA technologies are used such as: parametric amplifiers (paramps), Masers (microwave amplification by stimulated emission of radiation) and field-effect transistors (FETs).

Masers can achieve the lowest noise performance of any type of LNA [1]. However, they are expensive, complicated and require operation at liquid helium temperatures [2]. Thus, they see limited use in radio-telescopes.

Until the early 1980's paramps saw the most use as receiver front-ends in radio-telescopes [3]. They are difficult to match, require power oscillators at several times their operational frequencies and also require cryogenic operation to optimize their performance.

Due to the shortcomings of masers and paramps and the tremendous advances in transistor technology, FET amplifiers are quickly taking over as the leader in most LNA applications. They are easy to use, have a large bandwidth, are relatively cheap and today challenge the noise performance of the best paramps.

The most recent innovation in FET technology has been the development of high electron mobility transistors

(HEMTs). HEMTS, due to their extremely large gain bandwidths and low noise performance, are becoming the transistor of choice in most LNA designs [1,4]. Figure 1.1 gives a plot of the noise temperatures versus frequency for several of the mentioned devices.

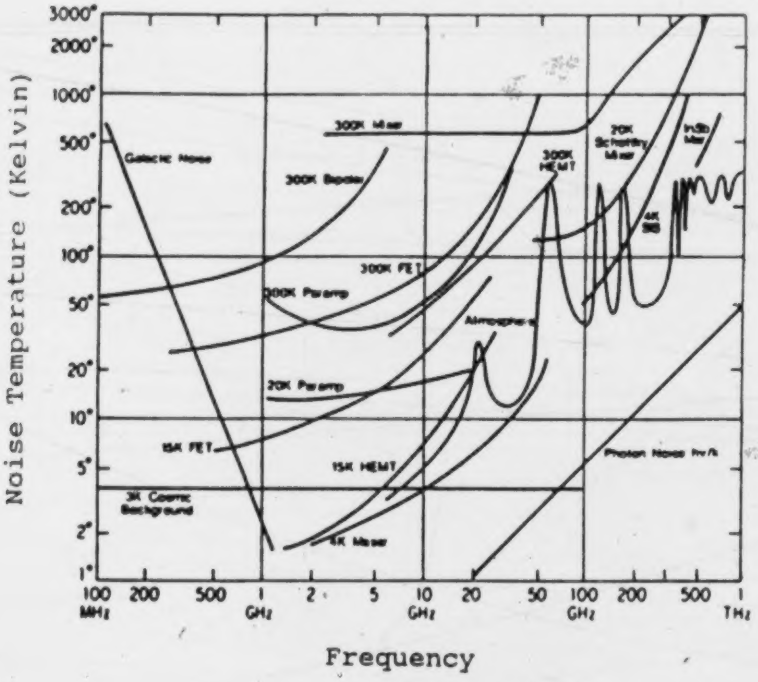

Figure 1.1: Noise temperatures of various devices versus frequency including natural limits. Modified from Weinreb et al. [1].

1.2 Goals of this Thesis

It is well known that the noise performance of transistors improves as the physical temperature is decreased. Pospieszalski et al. [5] predict that the noise temperature (T_n) of a HEMT will decrease linearly with physical temperature until a T_n of zero is reached at zero degrees Kelvin. Mochizuki et al. [6] demonstrated that the noise temperatures of HEMTs decrease with temperature roughly as a power law, with the exponent dependent on frequency from 1.76 at 20 GHz to 1.91 at 2 GHz. This result was far more optimistic than that of Pospieszalski. Work described later in this thesis has shown that the conclusions of Pospieszalski are correct, which places the results of Mochizuki et al. in question.

Traditionally, in order to achieve this improved performance, LNAs have been bulk cooled to cryogenic temperatures (≤100K). This normally involves the use of closed-cycle helium refrigerators. However, in addition to being bulky and maintenance intensive, these refrigerators often dominate the cost of the LNA. Amplifier parts typically cost less than $200, whereas the refrigerator costs around $10,000. If a multiple antenna system is desired, such as the 100 telescope array proposed by the National Research Council of Canada's Herzberg Institute of Astrophysics, the total cost of the refigerators would be immense and their maintainance requirements would be nearly unmanageable. Therefore, a very definite need exists for low-cost, maintenance free LNAs provided that their noise performance is close to that of cryogenically cooled LNAs.

HEMTs perform so well that it is tempting to use them in uncooled amplifiers. However, in radio-telescopes where decreases in system noise temperature are difficult to achieve, any significant improvement in noise performance is highly desirable. Fortunately, as mentioned above, the performance of FETs and HEMTs improves substantially even with moderate cooling.

If one were to cool only the critical components of an LNA, such as the first stage transistor, the required cooling capacity of the refrigerator would be greatly reduced. This would enable the use of much simpler refrigerators which require less maintenance, or, a single powerful refrigerator to cool the critical components of several LNAs. Marlow Industries [7] in Dallas, U.S.A, manufactures a thermoelectric refrigerator which has a maximum temperature differential of 130K. Also, recently available on the market are microminiature Joule-Thompson refrigerators [8] with moderate cooling capacities. They can operate at any temperature from ambient down to 77K and have very slow boil off rates of their working fluid, usually nitrogen.

Thermoelectric, or Peltier, cooling has long been used in LNA applications [9,10,11,12]. However, its primary use has been that of a bulk refrigerator unit, cooling the entire LNA. Some such units are commercially available through Berkshire Technologies [13]. In general, these designs sacrifice the lowest temperatures available through Peltier cooling for high heat capacity in refrigerators required to bulk cool an entire LNA.

The main thrust of this thesis is the investigation of the application of thermoelectric cooling to the first stage of an LNA using the Marlow refrigerator. Several problems arise from the concept of cooling only particular components. The thermal design must be fully integrated with the microwave design. That is, the RF characteristics of the refrigerator must be compensated for or eliminated. Proper RF paths must exist and at the same time, the cooled components must be thermally isolated. This results in the need for materials which are good electrical conductors but poor thermal conductors, properties which are normally physically contradictory.

The immediate concern is to produce LNAs for use at 1.42GHz, the primary observation frequency at the Dominion Radio Astrophysical Observatory (DRAO) in Penticton, British Columbia. Currently DRAO employs LNAs based on a design by Weinreb et al. [14] and modified by Walker et al. [15] with HEMTs in the first stage. These are operated at room temperature in the synthesis telescope [16] and are cryogenically cooled in the single 26-metre telescope [15].

DRAO is currently planning to build a 100 antenna telescope to operate at multiple frequencies [17]. The availability of simple and inexpensive refrigeration schemes in the design of high performance LNAs would be very beneficial to this project. With this in mind, the possibility of applying alternative cooling techniques such as Peltier or Joule-Thompson to one or more LNAs will be investigated.

Chapter 2: LNA Design Theory and Technique

2.0 Introduction

The receiver is the primary radio-telescope component over which the system designer has control and where improvements in sensitivity can be realized. Of all the receiver components, the front-end (usually an LNA) has the most impact on sensitivity.

Several factors must be taken into account in the design of LNAs. They must be optimized for noise performance and at the same time have sufficient gain to reduce the noise contribution of subsequent receiver stages to insignificant levels. The LNA must be stable, not only at the operation frequency, but at all frequencies, since oscillations severely degrade the amplifier performance. A computer program will be described in this chapter which was developed to assist in choosing the optimum matching and feedback conditions necessary to achieve the above design objectives.

HEMTs currently have the best noise performance of any solid-state devices and will be used in this project. The low noise performance does, however, come at a cost. HEMTs are intrinsically unstable devices and have almost purely reactive input impedances. This necessitates the use of feedback and other techniques to ensure stability and to optimize noise and gain performance. A further complication in the design which is the topic of this thesis is that, in order to cool only the HEMT, it must be thermally isolated and the effects of the refrigerator on RF performance must be compensated for or eliminated.

2.1 Radio-telescope Sensitivity

Before proceeding further with the discussion of LNA design, it is important to explain how the receiver performance affects the radio-telescope's overall sensitivity. The sensitivity of the telescope can be defined as a measure of the weakest source it can detect. Several factors influence the sensitivity of the telescope, including: receiver performance, observing time, antenna characteristics and the sky region to be observed. Measurement error and the limits of detection are determined by fluctuations in voltage at the output of the receiver. These fluctuations are caused by the signal itself, the medium between the telescope and the source, unwanted interfering signals, receiver noise, and variations in receiver performance.

Although not all the sources of interest to radio astronomers are thermal in origin, they all share some of the statistical characteristics of thermal black body radiation. That is, the energy flux measured at any one point fluctuates randomly about a mean value called its 'intensity' or 'flux density'. In the case of thermal black body radiation the flux density is given by Planck's Law as follows [18]:

$$B = \frac{2hf^3}{c^2} \frac{1}{e^{hf/kT}-1}, \qquad (2.1.1)$$

where 'B' is the brightness (watts m^{-2} Hz^{-1} rad^{-2}), 'h' is Planck's constant (6.63×10^{-34} joule sec), 'f' is frequency (Hz), 'c' is the speed of light (3×10^{8} m sec^{-1}), 'k' is Boltzmann's constant (1.38×10^{-23} joule K^{-1}), and 'T' is temperature (Kelvin). At radio frequencies the product 'hf' is much less than 'kT' so that $e^{hf/kT}-1$ is approximately equal to hf/kT and (2.1.1) can be reduced to [18]:

$$B = 2kT/\lambda^2, \qquad (2.1.2)$$

where λ is wavelength. Equation (2.1.2) is better known as the Rayleigh-Jeans Law. It implies that a source can be assigned a temperature (T_B) which has no relation to its physical temperature but is an indication of its brightness or intensity.

The interstellar medium between the source and the telescope contains clouds of ionized gas. This gas can cause scintillation of sources which have small angular diameters. However, most problems are produced by the Earth's atmosphere itself, especially at the extremes of the radio spectrum. At long wavelengths (metre and decimetre), ionospheric variations have detrimental effects while at the short wavelengths (centimetre and millimetre) the lower atmosphere causes attenuation and scattering of the signal.

Aside from the main beam, all radio-telescopes have sidelobes which are unintentionally directed at sources other than the source under observation. These unwanted sources are radiation from the rest of the sky, thermal emission from the Earth, or man-made interference such as television signals or radar. The first two sources are normally of the same statistical nature as the wanted signal and can be measured and corrected for using calibration techniques. Man-made interference can be partially overcome by locating the telescope in remote areas with mountains and the curvature of the Earth acting as natural shields against the unwanted signals.

All electronic circuits generate noise in varying degrees. In a radiotelescope receiver, this noise is added to that received by the antenna. Noise power is typically expressed as a noise temperature. The noise power per unit bandwidth available from a resistor at temperature T is given by Nyquist's formula [19];

$$p = kT \quad (\mathrm{W\ Hz}^{-1}), \qquad (2.1.3)$$

where k is Boltzmann's constant and T is temperature in Kelvin. Therefore, the receiver's noise contribution can be modelled by a resistor at its input having temperature T_{RX}, its equivalent noise temperature.

Equipment instabilities such as drifts or jumps in gain can be a large source of measurement error. When signals are detected in the presence of millions of times more unwanted noise, a very small change in gain results in a huge false deflection at the output. These undesired effects can be reduced substantially with correlation or switched receiver techniques [20].

When discussing the sensitivity of a telescope it is usually assumed that all the unwanted signals are of the same statistical nature as thermal black-body radiation. Although we know this is not entirely true, in practice it is an ideal which can nearly be reached and which greatly simplifies mathematical analysis.

In general, radio astronomers are interested in determining the average flux density per unit bandwidth. The true average can only be found by measuring the randomly fluctuating output power from the antenna over an infinite period of time. However, since this is not very practical, finite integration times can be employed which yield sufficiently accurate values of average flux density.

In a typical receiving system as shown in figure 2.1.1, with a bandwidth Δf, variations in amplitude much faster than $1/\Delta f$ cannot be detected. Since the amplitude of the signal follows a Gaussian distribution with standard deviation σ, the central limit theorem states that if N samples are taken (yielding a total integration time of τ =

N/Δf), the output will have the same mean and also be Gaussian in nature with

$$\sigma_G = \sigma/\sqrt{N} = \sigma/\sqrt{\tau\Delta f}, \qquad (2.1.4)$$

where σ_G is the resulting standard deviation. Therefore, the average of N measurements is $\sqrt{N}$ times more accurate than a single measurement of the same length as one of the N samples. Also, the r.m.s error in a single measurement period is inversely proportional to the square root of the receiver bandwidth.

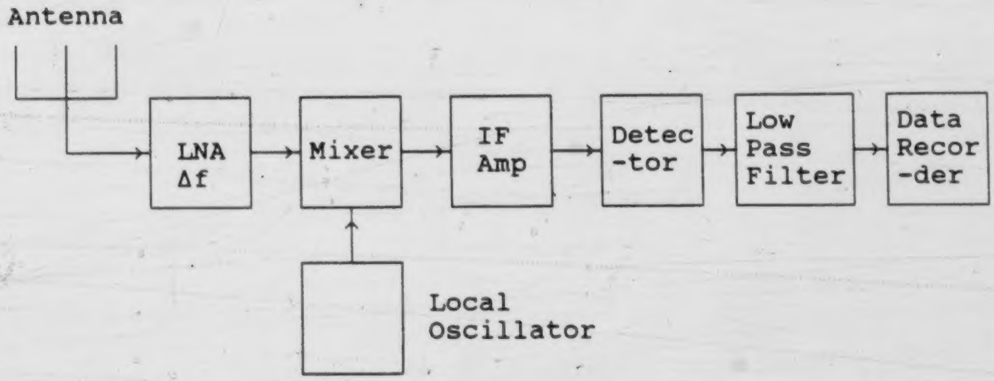
Antenna
LNA
Δf
Mixer
IF
Amp
Detec
-tor
Low
Pass
Filter
Data
Recor
-der
Local
Oscillator

Figure 2.1.1: Typical Superheterodyne radio-telescope receiver.

If the detector shown in figure 2.1.1 has a square-law transfer characteristic, the mean level of the output voltage will be proportional to the detected noise power, which is proportional to the system noise temperature plus the equivalent noise temperature of the input signal. The output r.m.s. fluctuation level referred to the input ($\Delta T_{r.m.s.}$) can be given by [20]:

$$(\Delta T_{r.m.s.}) \propto T_{sys}/\sqrt{\tau \Delta f}, \qquad (2.1.5)$$

where T_{sys} is the system noise temperature due to the receiver noise, galactic background radiation, atmospheric attenuation, cosmic black-body radiation, antenna spillover and the source itself. In actual radiotelescopes, the factor $\tau\Delta f$ is usually very large ($\cong 10^4$ or greater). This means that fluctuations in the receiver output will represent powers which are very small compared to the system temperature, enabling the detection of sources much smaller than the noise from the rest of the sky, the receiver, etc. In general, an output deflection of 3 x $\Delta T_{r.m.s.}$ or greater provides adequate certainty that a source has indeed been detected.

The expression for $\Delta T_{r.m.s.}$ (2.1.5) shows that the output fluctuation level of the radiotelescope is directly proportional to the system temperature. Of all the sources of noise, the system designer has control over only antenna spillover and receiver noise. Table 2.1 gives the current system noise temperature breakdown for the DRAO Synthesis Telescope at its L-band observation frequency [21]. It employs room temperature HEMT LNAs in its receiver

Source	T_N
Receiver	50-53
Spillover	14
Leakage	1.5-6
Atmosphere	4
Sky	5
Total	75-82

Table 2.1: System Noise Temperature Breakdown for DRAO Synthesis Telescope at L-band [21].

front-ends. At present, the LNA dominates the system noise temperature. Reducing the noise temperature of the LNAs by half, to say 25K, would correspond to more than a 30 percent drop in the system temperature or a 30 percent increase in telescope sensitivity.

2.2 Noise in Two-Port Networks

All active two-port networks (and lossy passive networks) will produce a measurable output power even in the absence of an input signal. In the case of an amplifier, this power is referred to as the amplifier noise power. When there is a signal present at the amplifier input, the output power will be a combination of the amplified input power and the amplifier noise power.

As shown in figure 2.2.1, the noise input to the amplifier can be represented by an equivalent noisy resistor producing thermal or Johnson noise. The noise power produced by a resistor is given by [19]:

$$P_{Ni} = kTB, \qquad (2.2.1)$$

where k is Boltzmann's constant, T is the temperature of the resistor in Kelvin and B is the noise bandwidth in Hertz. The resistor can then be replaced by a noiseless resistor in series with a noise generator producing an r.m.s. voltage given by

$$V_N = \sqrt{4kTBR_N}. \qquad (2.2.2)$$

The total noise power available at the output of the amplifier is then

$$P_{No} = G_A P_{Ni} + P_{Nrx}, \qquad (2.2.3)$$

where P_{Nrx} is the noise produced inside the amplifier referred to the output and G_A is the available gain of the amplifier.

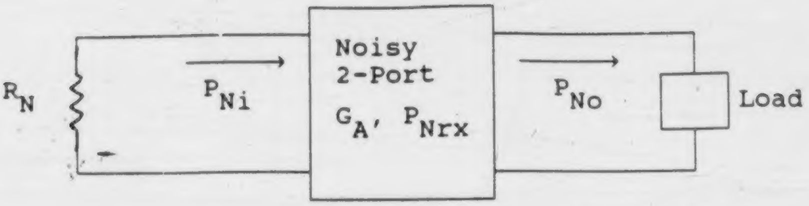

Figure 2.2.1: Model of Noisy Two-Port.

The noise figure (F) of an amplifier gives a quantitative description of its noise performance and is defined [22] as the ratio of the total available noise power at the output to the noise power at the output due only to the fictitious resistor R_N. Thus the noise figure is given by:

$$F = \frac{P_{No}}{P_{Ni}G_A} \quad . \qquad (2.2.4)$$

Since the available gain, G_A, is defined as the ratio of available signal power at the output (P_{So}) to the available signal power at the input (P_{Si}), or

$$G_A = P_{So}/P_{Si} \quad , \qquad (2.2.5)$$

the noise figure can be expressed as follows:

$$F = \frac{P_{Si}/P_{Ni}}{P_{So}/P_{No}} \quad , \quad (2.2.6)$$

which is simply the ratio of the input signal to noise ratio (SNR) over the output SNR and can be rewritten as,

$$F = 1 + \frac{P_{Nrx}}{G_A kTB}. \quad (2.2.7)$$

For the case of two cascaded two-ports (figure 2.2.2), the above analysis can be extended to show that the composite noise figure is given by:

$$F = F_1 + \frac{F_2 - 1}{G_{A1}} \quad , \quad (2.2.8)$$

where F_1 is the noise figure of network 1 and F_2 is the noise figure of network 2. For n cascaded two-ports the noise figure is as follows [22]:

$$F = F_1 + \frac{F_2 - 1}{G_{A1}} + \frac{F_3 - 1}{G_{A1} G_{A2}} + \ldots + \frac{F_n - 1}{G_{A1} G_{A2} \ldots G_{An}} \quad . \quad (2.2.9)$$

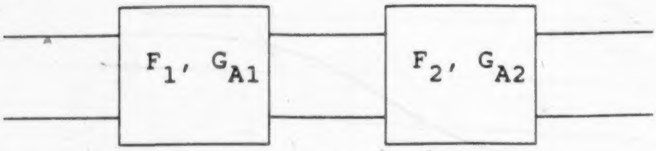

$$F = F_1 + (F_2 - 1)/G_{A1}$$

Figure 2.2.2: Noise Figure of Cascaded Two-Ports

Equation 2.2.9 shows that the noise figure of a cascaded system is dominated by the noise figure of the first stage and that the noise contributions of subsequent stages are diminished as the available gains of the preceding stages are increased. In the design of LNAs, this leads to the necessity of optimizing the noise performance and gain of the first stage in order to achieve the minimum overall noise temperature.

The noise performance of any two-port network can be characterized by its four noise parameters. These parameters can be represented in several different forms. The most common representation used by device manufacturers is: r_n, the equivalent normalized noise resistance ($r_n = R_N/Z_o$), F_{min}, the minimum noise figure of the device, and Γ_o, the complex source reflection coefficient which results in F_{min}. The device noise figure is given as a function of these parameters by [23].

$$F = F_{min} + \frac{4r_n|\Gamma_s-\Gamma_o|^2}{(1-|\Gamma_s|^2)|1+\Gamma_o|^2} \quad , \qquad (2.2.10)$$

where Γ_s is the actual source reflection coefficient. In a three-dimensional plot of noise figure versus source impedance (source impedance is plotted on a two-dimensional complex plane), the result is a quasi-parabolic surface of revolution with the minimum, F_{min}, occurring at Z_s equal to Z_{opt}, the source impedance resulting in Γ_o. Movement of Z_s away from Z_{opt} in any direction results in an increase in the noise figure, F. The noise figure can also be expressed in terms of the optimum source impedance, Z_{opt}, as follows [24]:

$$F = F_{min} + \frac{r_n|Z_s - Z_{opt}|^2}{r_s|Z_{opt}|^2} \qquad (2.2.11)$$

where r_s is the normalized source resistance. The noise figure can easily be converted to a noise temperature using the following relationship:

$$T = (F-1) \times 290K. \qquad (2.2.12)$$

2.3 High Electron Mobility Transistors

Until the advent of HEMTs (high electron mobility transistors), MESFETs (MEtal-Semiconductor Field Effect Transistors) yielded the best noise performance of any transistor. HEMTs have surpassed them in the two critical figures of merit for microwave transistors: current-gain cut-off frequency (f_t) and noise figure [25]. Not only do HEMTs give excellent performance in microwave applications, they also show potential in high speed digital applications once the technology for their large scale integration is developed. They are touted as the technology which will form the basis of the fifth generation of supercomputers [26].

Several acronyms have been created for HEMTs, all of which describe their operation or fabrication technique. Some of these acronyms are: MODFET (MOdulation Doped FET), TEGFET (Transverse Electron Gas FET), 2DEGFET (Two-Dimensional Electron Gas FET) ,and SDHT (Selectively Doped Heterojunction Transistor).

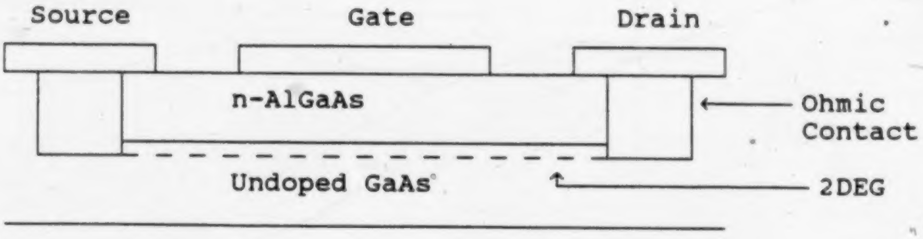

Figure 2.3.1: Structure of the HEMT (modified from [26]).

The structure of a HEMT (see figure 2.3.1) is similar to that of an n-MOSFET except that it consists of layers of compound semiconductors instead of silicon. The bulk silicon is replaced by a layer of undoped Gallium Arsenide

(GaAs) while the silicon dioxide is replaced by a layer of n-doped AlGaAs. Electrons from the doped AlGaAs move through the crystal until they reach the lowest energy state allowed to them. This energy level is found just to the GaAs side of the heterojunction interface where the electrons accumulate on a two-dimensional plane (hence TEGFET or 2DEGFET) on which they are free to move laterally. This physical separation of the conduction electrons from their parent donor impurities significantly reduces the rate of scattering and randomization in the drain-source channel, thus increasing the electron mobility. The end result is a faster transistor with a lower noise figure. The ability to obtain a large sheet concentration of conduction electrons without the penalty of a large scattering rate is the main advantage of HEMTs over MESFETs [26].

In producing a very fast low noise transistor, several inherent design problems are created. The high f_t of HEMTs means that the devices have gain up to tens of gigahertz [27,28] and thus are susceptible to oscillations over that entire range. Designers must therefore ensure stability at all frequencies up to f_t. Also, in order to produce a low noise transistor, loss in the gate of the transistor must be kept to a minimum. This results in a very reactive input impedance and subsequently an input reflection coefficient close to unity (closer to unity at lower microwave frequencies). This makes input matching difficult and contributes to the inherent instability of the device.

The Nippon Electric Company (NEC) [29] quotes a minimum noise temperature of 24 Kelvin for their NE320 series HEMTs at 1.4 GHz. This compares favourably with a T_{min} of about 40 Kelvin for Mitsubishi's MFG1412 GaAsFETs which are commonly used in L-band LNAs [14,30-32]. For a quick verification of the NE32084 performance, the first stage MFG1412 GaAsFET in one of the amplifiers currently used at DRAO [15] was replaced by the NEC HEMT. With minor modifications to the input tuning network, a minimum noise temperature of 31 Kelvin was achieved compared to a typical value of 50 Kelvin for LNAs employing MFG1412s in their first stage. The LNA was then bulk cooled down to -56°C with dry ice resulting in a T_{min} of 18 Kelvin. These results, however impressive, were very narrowband and thus demonstrated the need for extensive development. The above results will be discussed in more detail in Chapter 4 and were mentioned here as a justification for further use of the NEC HEMT.

2.4 RF Design Theory

Several factors must be taken into account in the design of an amplifier. Most importantly, in the case of LNAs, the noise figure must be minimized. Other considerations are the gain, bandwidth, input and output matching, and not insignificantly, the stability. In general, the optimum input match condition for noise performance does not coincide with that for a conjugate match. However, feedback techniques can be employed to move the conflicting matching positions closer together. The first step in the design process should be to determine the source and load reflection coefficients (Γ_S and Γ_L respectively) and the required feedback which will simultaneously achieve the desired gain and noise figure, and maintain stability.

The *scattering parameters* or S-parameters are commonly used in microwave applications to characterize a two-port network and will be used extensively in this thesis. They are based on waves incident on, or reflected by a two-port network (shown in figure 2.4.1) as opposed to voltages and currents used in the definition of most other parameter sets. The *scattering matrix* is represented as follows:

$$\begin{bmatrix} S \end{bmatrix} = \begin{bmatrix} S_{11} & S_{12} \\ S_{21} & S_{22} \end{bmatrix} .$$

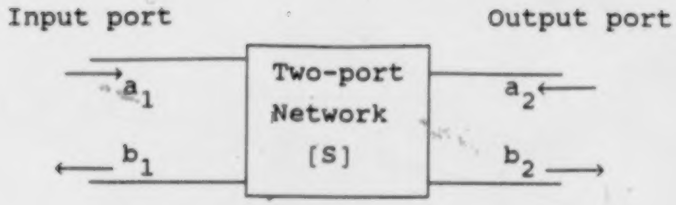

$$b_1 = S_{11}a_1 + S_{12}a_2$$

$$b_2 = S_{21}a_1 + S_{22}a_2$$

Figure 2.4.1: Scattering Matrix representation of a two-port network.

A very useful tool which graphically assists in solving or analysing microwave problems is the Smith Chart. It is a representation of impedances or admittances in the reflection coefficient plane, or Γ plane. The transformation equations used are

$$\Gamma = \frac{Z - Z_o}{Z + Z_o} = \frac{Y_o - Y}{Y_o + Y} \qquad (2.4.1)$$

where Z and Y are all values of impedances and admittances such that *Re*[Z] and *Re*[Y] are greater than or equal to zero and Z_o and Y_o are the characteristic impedance or admittance of a transmission line, or a reference value. On the Smith Chart impedances and admittances are plotted as normalized values. The transformation equations then become

$$\Gamma = \frac{z - 1}{z + 1} = \frac{1 - y}{1 + y} \qquad (2.4.2)$$

where $z = Z/Z_o$ and $Y = Y/Y_o$. A unity circle defines the Smith Chart region formed by setting $|\Gamma| = 1$ within which all the impedances and admittances with positive real parts must lie.

2.4.1 Gain Definitions

Three different gain formulas commonly used in RF amplifier design are derived by Gonzalez [23], using Mason's rule and two-port S-parameters. The transducer power gain, G_T, is a function of Γ_S, Γ_L, and the device S-parameters; operating power gain, G_P, is a function of Γ_L and the S-parameters; available power gain, G_A, is a function of Γ_S and the S-parameters. They are defined as follows:

$$G_T = \frac{P_L}{P_{AVS}} = \frac{\text{power delivered to load}}{\text{power available from source}}$$

$$= \frac{1 - |\Gamma_S|^2}{|1 - S_{11}\Gamma_S|^2} |S_{21}|^2 \frac{1 - |\Gamma_L|^2}{|1 - \Gamma_{OUT}\Gamma_L|^2} \qquad (2.4.1.1)$$

$$G_P = \frac{P_L}{P_{IN}} = \frac{\text{power delivered to load}}{\text{power input to network}}$$

$$= \frac{1}{1 - |\Gamma_{IN}|^2} |S_{21}|^2 \frac{1 - |\Gamma_L|^2}{|1 - S_{22}\Gamma_L|^2} \qquad (2.4.1.2)$$

$$G_A = \frac{P_{AVN}}{P_{AVS}} = \frac{\text{power available from network}}{\text{power available from source}}$$

$$= \frac{1 - |\Gamma_S|^2}{|1 - S_{11}\Gamma_S|^2} |S_{21}|^2 \frac{1}{1 - |\Gamma_{OUT}|^2} \qquad (2.4.1.3)$$

where Γ_{IN} and Γ_{OUT} are the input and output reflection coefficients of the network, respectively, and are given by [23]:

$$\Gamma_{IN} = S_{11} + \frac{S_{12}S_{21}\Gamma_L}{1 - S_{22}\Gamma_L} \qquad (2.4.1.4)$$

and

$$\Gamma_{OUT} = S_{22} + \frac{S_{12}S_{21}\Gamma_S}{1 - S_{11}\Gamma_S} . \qquad (2.4.1.5)$$

2.4.2 Stability

Network stability is a measure of the circuit's resistance to oscillation. A network is unstable if the real part of its input or output impedance is negative, that is, if $|\Gamma_{IN}|$ or $|\Gamma_{OUT}|$ is greater than unity. If the network is potentially unstable it means that there exist possible terminations Γ_S and Γ_L which make it unstable. A quantitative measure of stability, the 'K' factor, can be derived [23] using the stipulations that $|\Gamma_{IN}|$ and $|\Gamma_{OUT}|$ be less than unity. The stability factor is given by:

$$K = \frac{1 - |S_{11}|^2 - |S_{22}|^2 + |\Delta|^2}{2|S_{12}S_{21}|} \qquad (2.4.2.1)$$

where $|\Delta| = |S_{11}S_{22} - S_{21}S_{12}|$.

The necessary conditions for unconditional stability are:

$$K > 1$$

$$|\Delta| < 1$$

$$|\Gamma_S| < 1$$

$$|\Gamma_L| < 1$$

The maximum value of gain which can be achieved and still enable a stable circuit is defined as follows [23]:

$$G_{MSG} = |S_{21}|/|S_{12}| \qquad (2.4.2.2)$$

A graphical technique exists which assists in choosing appropriate termination reflection coefficients for potentially unstable devices. Setting the magnitudes of Γ_{IN}

and Γ_{OUT} (equations 2.4.1.4 and 2.4.1.5) equal to unity results in a pair of circles on the Smith chart. The perimeters of these stability circles are the values of Γ_S or Γ_L for which $|\Gamma_{OUT}| = 1$ or $|\Gamma_{IN}| = 1$. The equations for the input and output stability circles are as follows [23]:

$$r_L = \left| \frac{S_{12}S_{21}}{|S_{22}|^2 - |\Delta|^2} \right| \qquad (2.4.2.3)$$

$$C_L = \frac{(S_{22} - \Delta S_{11}^*)^*}{|S_{22}|^2 - |\Delta|^2} \qquad (2.4.2.4)$$

$$r_S = \left| \frac{S_{12}S_{21}}{|S_{11}|^2 - |\Delta|^2} \right| \qquad (2.4.2.5)$$

$$C_S = \frac{(S_{11} - \Delta S_{22}^*)^*}{|S_{11}|^2 - |\Delta|^2} \qquad (2.4.2.6)$$

where r_L and r_S are the radii and C_L and C_S are the centers of the respective stability circles. It is then necessary to determine whether or not the stable regions are inside or outside the circles. This can easily be accomplished by evaluating $|\Gamma_{IN}|$ or $|\Gamma_{OUT}|$ at the center of the Smith chart (ie. $\Gamma_L=0$ and $\Gamma_S=0$). If they are less than one and inside (outside) a circle, then the unstable region is outside (inside) that circle. The opposite holds true for values of $|\Gamma_{IN}|$ and $|\Gamma_{OUT}|$ greater than unity when evaluated at the origin.

Ensuring stability throughout the active range of the HEMT is extremely challenging since the characteristics of the terminations are not necessarily known at the frequency extremes. Several techniques have been developed to improve out-of-band stability. Weinreb et al. [14] found it necessary to employ high-pass gain roll-off circuitry as well as ferrite toroids in the signal path to ensure stable terminations at all frequencies and to minimize increases in the reverse transmission parameter, S_{12}, created by circuitry external to the transistor. Weinreb et al. [14] used wide band attenuators (typically 6 dB) at the output of the LNA to isolate the amplifier stages from unpredictable loading conditions.

Another consideration in maintaining amplifier stability is the actual physical dimensions of its enclosure, which is normally a highly conductive metal. At high frequencies, the wavelength is of the same order as the size of the enclosure, making it possible for several resonant modes to exist. If the device still has gain at the resonant frequencies, instability may result. A possible method of overcoming this problem is to insert lossy material at strategic locations in the cavity to damp the resonance.

2.4.3 Source Inductive Feedback

In general, the match condition for minimum noise figure in a microwave device does not coincide with that for maximum power transfer, that is, $\Gamma_o \neq \Gamma_{IN}^*$. The consequence of matching simply for minimum noise performance is a large input standing wave ratio (SWR), which causes gain ripples across the pass band and makes broadband designs difficult. This effect is greatly magnified in the case of HEMTs at L-band since, in that frequency range, the HEMT input impedance is almost purely reactive. Lossless source inductance has long been known to assist in moving Γ_{IN}^* closer to Γ_o [14,15,33,34], and if kept below a critical value, to have negligible effect on device noise performance. The end result is the possibility of simultaneously matching for both optimal noise performance as well as for a small input reflection coefficient.

Two additional benefits arise from the use of source inductive feedback in this application. One advantage is that it may increase the in-band stability for L-band HEMTS. The other is that it allows for a thermal break in the source leads which otherwise would be connected directly to ground. This effect will discussed in more detail in chapter 3.

Anastassiou and Strutt [33] showed that lossless source inductance, L_s, in a GaAsFET has negligible effect on the minimum noise temperature at L-band for values of inductance up to about 4nH. This was further demonstrated by Vendelin [34] who determined that the optimum source impedance for a noise match, Z_{opt}, is altered by an amount approximately equal to $-j2\pi fL_s$ at each frequency or,

$$Z_{opt} \cong Z_{opt} - j2\pi fL_s . \qquad (2.4.1.3)$$

A microwave circuit analysis package for PCs, Touchstone®, was used to quantify the effects of lossless source inductive feedback on the NE32000 HEMT. The equivalent circuit model (provided by NEC Corp.) of the HEMT is given with the added source inductance in figure 2.4.3.1. The device S-parameters, also provided by NEC, served as the input for Touchstone®. Figure 2.4.3.2 shows how the HEMT input impedance at 1.4 GHz becomes more real as L_s is increased. The normalized HEMT input impedance, $\mathfrak{z}_{IN}$, is easily determined from the modified input reflection coefficient, S_{11}, (obtained from Touchstone®) using the following relationship:

$$\mathfrak{z}_{IN} = \frac{1 - S_{11}}{1 + S_{11}} . \qquad (2.4.3.2)$$

Here Touchstone® assumes a normalized load impedance equal to unity. Figure 2.4.3.3 shows how the input stability circle moves towards the outside of the Smith chart as L_s is increased, thus making the device more stable at L-band.

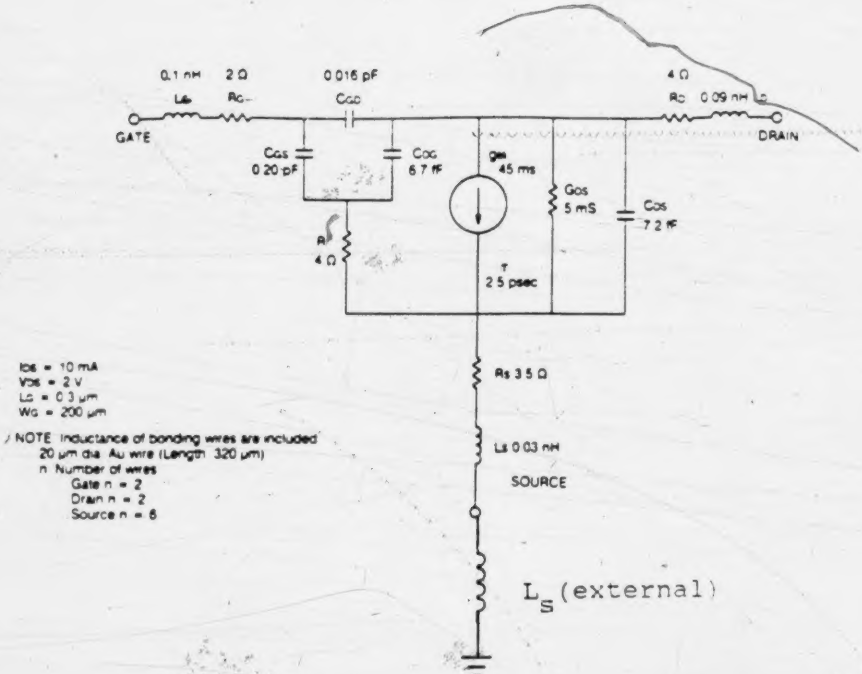
0.1 nH
2 Ω
0.016 pF
Lg
Rg
Cgd
GATE
Cgs
0.20 pF
Cdc
6.7 fF
gm
45 ms
Ri
4 Ω
τ
2.5 psec
Gds
5 mS
Cds
7.2 fF
4 Ω
Rd
0.09 nH
Ld
DRAIN
Rs 3.5 Ω
Ls 0.03 nH
SOURCE
IDS = 10 mA
VDS = 2 V
LG = 0.3 μm
WG = 200 μm
NOTE Inductance of bonding wires are included
20 μm dia. Au wire (Length 320 μm)
n Number of wires
Gate n = 2
Drain n = 2
Source n = 6
L_s (external)

Figure 2.4.3.1: Equivalent circuit for NE32000 HEMT with external source inductance. Modified from NEC [29].

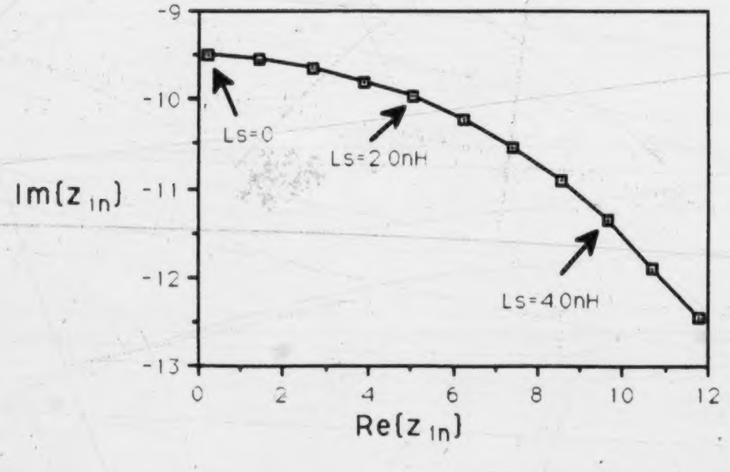

Figure 2.4.3.2: NE32000 HEMT normalized input impedance (z_{in}) with varying source inductance (L_s) and unity normalized load impedance.

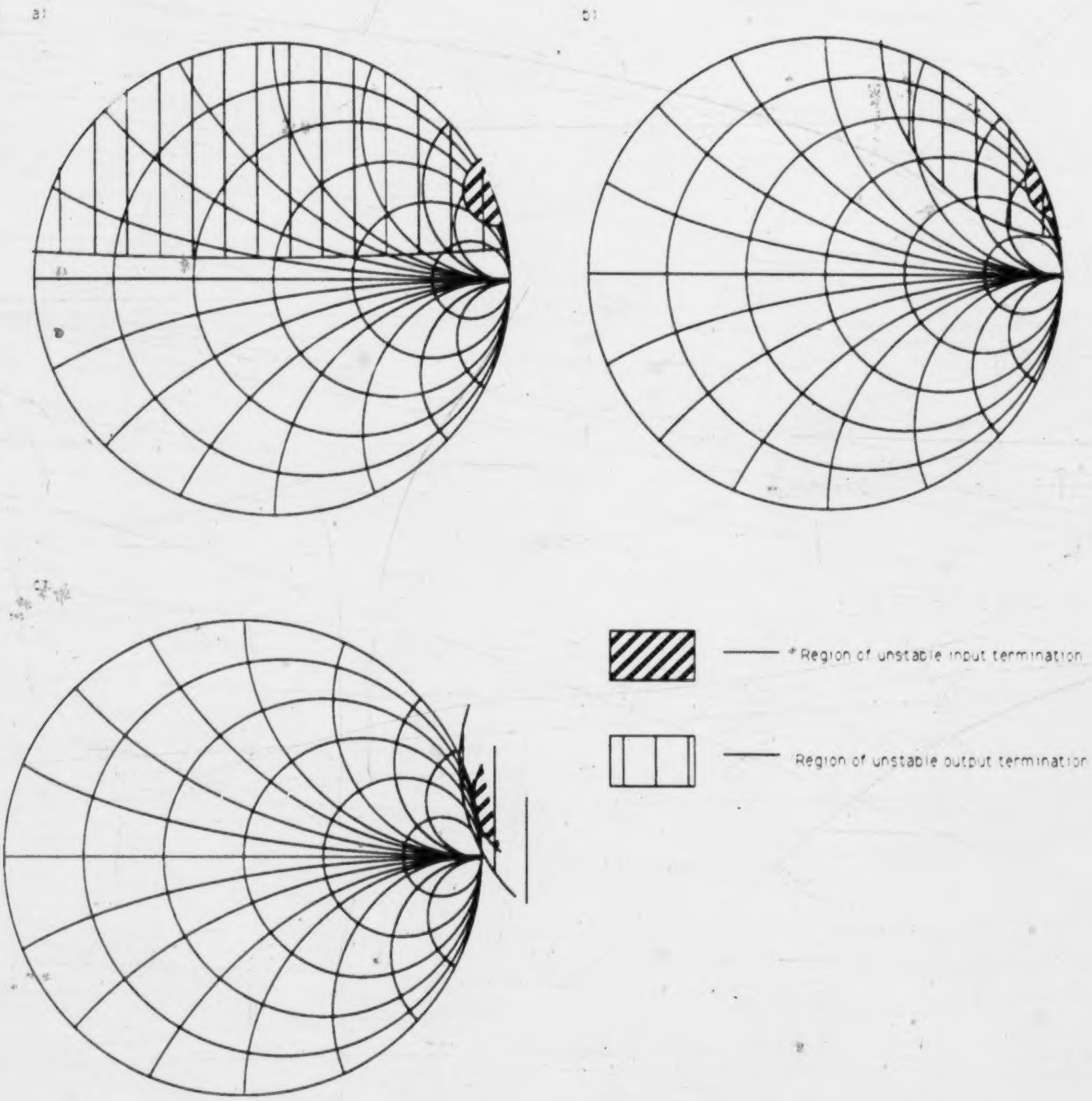

Figure 2.4.3.3: Effect of source lead inductance on stability circles at 1.4GHz for NE32000 HEMT (as shown on normalized impedance plots). a) L_s=0.0nH, b) L_s=1.0nH, c) L_s=3.5nH.

2.4.4 Design Procedure

The theory discussed above will be used in formulating a general approach for low noise amplifier design with bilateral devices ($S_{12}\neq 0$). The method incorporates a program written in FORTRAN (appendix 1.1) which assists in choosing the optimum values for source inductance (L_s) as well as the input and output reflection coefficients (Γ_S and Γ_L). Subsequent to the development of this program, a very similar procedure was published by Albinsson [35] indicating the need for such design tools. The general design approach is outlined below:

1. Using the FORTRAN program, determine the values of Γ_L, Γ_S, and L_s which yield the desired gain, minimum noise figure, and in-band stability.
2. Design the rough input and output matching networks to achieve the desired Γ values.
3. Optimize the design using Touchstone.
4. Determine the out-of-band stability and modify the matching networks if necessary.
5. Determine the component sensitivity using a Monte Carlo analysis.

The fact that a device is bilateral has one advantage in that it is possible to affect the input tuning through the load it sees ($\Gamma_{IN} = f(S,\Gamma_L)$). The program developed here uses this fact to advantage, enabling Γ_L to be variable but constrained to a set of values determined by the desired gain. For every value of Γ_L (if $|\Gamma_L| \le 1$), there exists a Γ_S which will result in a conjugate match at the input. Allowing L_s to vary provides a means of effectively altering the S-parameters of the device ($S' = f(S, L_s)$) until the point $\Gamma_{IN} \approx \Gamma_o^*$, is reached for a particular Γ_L.

The operating power gain, G_P, is the gain to be specified in the program as it is a function of only the device S-parameters and the load ($G_P = f(S', \Gamma_L)$). It is possible to draw a circle of constant operating gain [24] on the Smith chart. By rewriting equation 2.4.1.2 in the form

$$G_P = \frac{|S_{21}|^2 (1 - |\Gamma_L|^2)}{\left(1 - \left|\frac{S_{11} - \Gamma_L \Delta}{1 - S_{22}\Gamma_L}\right|^2\right) |1 - S_{22}\Gamma_L|^2} \qquad (2.4.4.1)$$

a gain parameter, g_P, can be defined using $G_P = |S_{21}|^2 g_P$ and written as

$$g_P = \frac{1 - |\Gamma_L|^2}{1 - |S_{11}|^2 + |\Gamma_L|^2 (|S_{22}|^2 - |\Delta|^2) - 2Re(\Gamma_L C_2)} \qquad (2.4.4.2)$$

where $C_2 = S_{22} - S_{11}^* \Delta$. Setting $\Gamma_L = U_L + jV_L$ and substituting into equation 2.4.4.2 produces, after some manipulation, a family of circles in the U_L:V_L plane (ie. the Smith chart). The centers of the circles are given by

$$C_P = \frac{g_P C_2^*}{1 + g_P(|S_{22}|^2 - |\Delta|^2} \qquad (2.4.4.3)$$

and the radii by

$$R_P = \frac{\left[1 - 2K|S_{21}S_{12}|g_P + |S_{21}S12|^2 g_P{}^2\right]^{1/2}}{\left|1 + g_P(|S_{22}|^2 - |\Delta|^2)\right|}\ , \qquad (2.4.4.4)$$

where K is given by equation 2.4.2.1. Using equations 2.4.4.3 - 2.4.4.4 and the device S parameters (modified by L_s), the program calculates values for Γ_L spaced along the perimeter of the circle for a given G_P. For each Γ_L, the Γ_S resulting in a conjugate match ($\Gamma_S = \Gamma_{IN}{}^*$) is then calculated using equation 2.4.1.4. The noise temperature T_N for each value of Γ_S is calculated using equations 2.2.10 - 2.2.11 where Γ_o is modified by L_S. Figure 2.4.4.1 gives a flowchart representation of how the program actually works.

The output of the program is a set of tables (Appendix 1.2) listing the Γ_S values required for a conjugate input match along with the corresponding values of Γ_L and T_N. The process is repeated for incremental values of L_S and again entirely, if desired, for different gains. From these results it is possible to visually select a match condition and a source inductance that produces a circuit which is stable at the design frequency, easy to implement, and which has a low noise temperature.

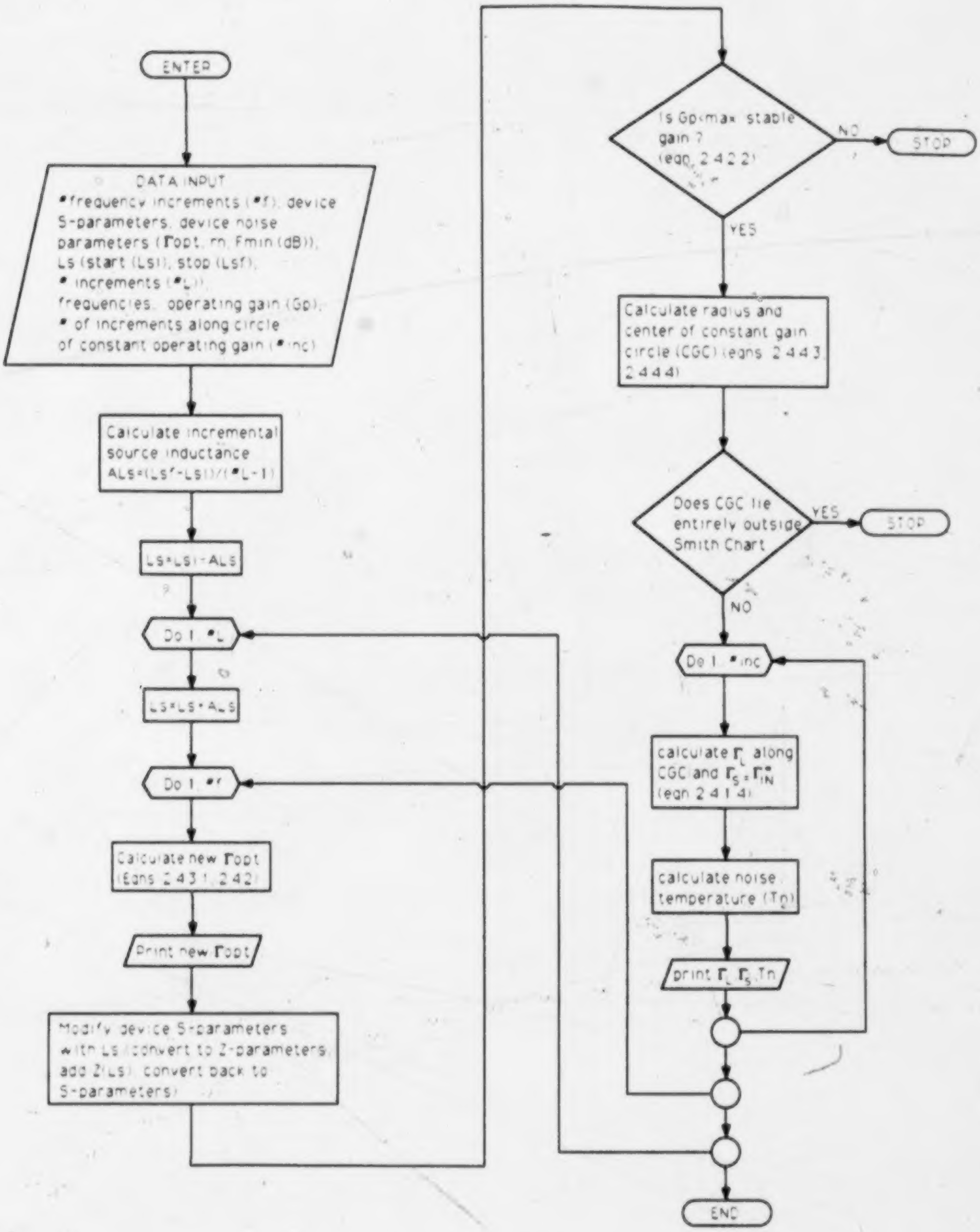
ENTER
DATA INPUT
#frequency increments (#f), device S-parameters, device noise parameters (Γopt, rn, Fmin (dB)), Ls (start (Lsi), stop (Lsf), # increments (#L)), frequencies, operating gain (Gp), # of increments along circle of constant operating gain (#inc)
Calculate incremental source inductance ΔLs=(Lsf-Lsi)/(#L-1)
Ls=Lsi-ΔLs
Do 1, #L
Ls=Ls+ΔLs
Do 1, #f
Calculate new Γopt (Eqns 2.4.3.1, 2.4.2)
Print new Γopt
Modify device S-parameters with Ls (convert to Z-parameters, add Z(Ls), convert back to S-parameters)
Is Gp<max. stable gain ? (eqn. 2.4.2.2)
NO
STOP
YES
Calculate radius and center of constant gain circle (CGC) (eqns. 2.4.4.3, 2.4.4.4)
Does CGC lie entirely outside Smith Chart
YES
STOP
NO
Do 1, #inc
calculate Γ_L along CGC and Γ_S = Γ*_IN (eqn. 2.4.1.4)
calculate noise temperature (Tn)
print Γ_L, Γ_S, Tn
END

Figure 2.4.4.1: Flowchart for LNA design program.

2.5 Initial RF Design

In this section a prelimary design for a three stage LNA will be carried out using the procedure outlined above. For thermal reasons to be explained in chapter 3, the first stage device will be a NEC32000 chip HEMT. The active devices in the following two stages will be NE32084 packaged HEMTs as they are easier to work with and are more rugged mechanically. Lumped circuit elements were chosen over transmission line elements for use in the design, although they are difficult to model at higher frequencies, because the size of transmission line components at L-band becomes prohibitively large. The specifications for this initial room temperature design are as follows:

Bandwidth = 150 MHz
Center frequency = 1.42 GHz
Noise temperature ≤ 35 K
Gain ≥ 40 dB ($G_P=G_T$ with input conjugately matched)
Input return loss (Γ_{IN}) ≤ -10 dB

The operating gain, G_P, was divided among the three stages with G_{P1} = 10 dB and $G_{P2} = G_{P3}$ = 15 dB. Figure 2.5.1 gives a block diagram of the three stages with their matching circuits. The design program was run at 1.4 GHz with the manufacturer's data for the HEMTs as input and the source inductance variable from 0 to 4 nH in .5 nH increments. Appendix 1.2 gives an example of the program's output tables which were used to determine the following reflection coefficients and source inductances used in the design:

$$\Gamma_{S1} = 0.80\angle 10^{\circ} \quad \Gamma_{L1} = 0.93\angle -25^{\circ} \quad L_{s1} = 3.5\text{nH}$$
$$\Gamma_{S2} = 0.83\angle 18^{\circ} \quad \Gamma_{L2} = 0.50\angle -27^{\circ} \quad L_{s2} = 1.5\text{nH}$$
$$\Gamma_{S3} = 0.83\angle 18^{\circ} \quad \Gamma_{L2} = 0.50\angle -27^{\circ} \quad L_{s3} = 1.5\text{nH}$$

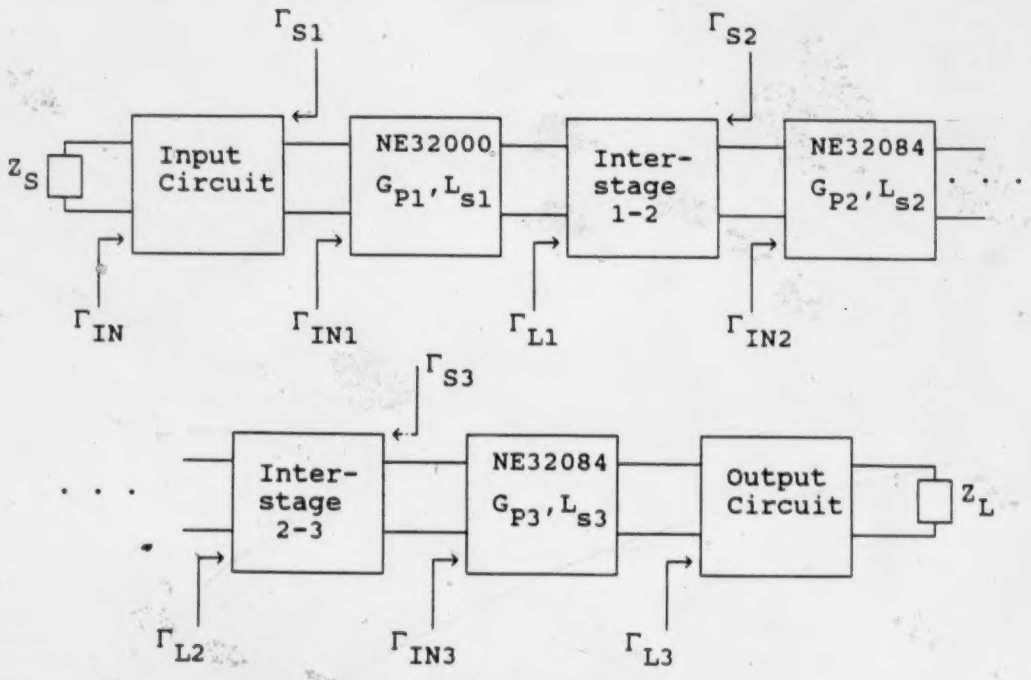
Γ_{S1}
Γ_{S2}
Z_S
Input Circuit
NE32000
G_{P1}, L_{s1}
Inter-stage 1-2
NE32084
G_{P2}, L_{s2}
. . .
Γ_{IN}
Γ_{IN1}
Γ_{L1}
Γ_{IN2}
Γ_{S3}
. . .
Inter-stage 2-3
NE32084
G_{P3}, L_{s3}
Output Circuit
Z_L
Γ_{L2}
Γ_{IN3}
Γ_{L3}

Figure 2.5.1: Three Stage LNA Block Diagram.

These reflection coefficients are all outside the unstable regions of the Smith Chart given in figure 2.4.2.1, thus indicating in-band stability.

The reflection coefficients and source inductances determined above were used as initial conditions for the design. A rough circuit was first designed on paper at 1.4 GHz. It was then entered into Touchstone® where it was optimized to meet the specifications given above. Several iterations of this process were carried out until a satisfactory design was produced. It was found that the values for L_{s2} and L_{s3} changed to 1.0nH after optimization. Stability was ensured on Touchstone® up to 10 GHz, beyond which the circuit models are certainly invalid.

Figure 2.5.2 gives the circuit schematic resulting from this design procedure. Figure 2.5.3 gives the circuit response obtained from Touchstone®. It can be seen that the circuit (as modelled on the computer) does in fact meet the design specifications.

In order to determine the sensitivity of the design to component variation, a Monte Carlo analysis was performed on the circuit using Touchstone®. For this analysis, a window of acceptable operation must be specified. Components are then randomly perturbed. The output is the percentage of trial perturbations which result in the circuit performance falling in the window of acceptable operation.

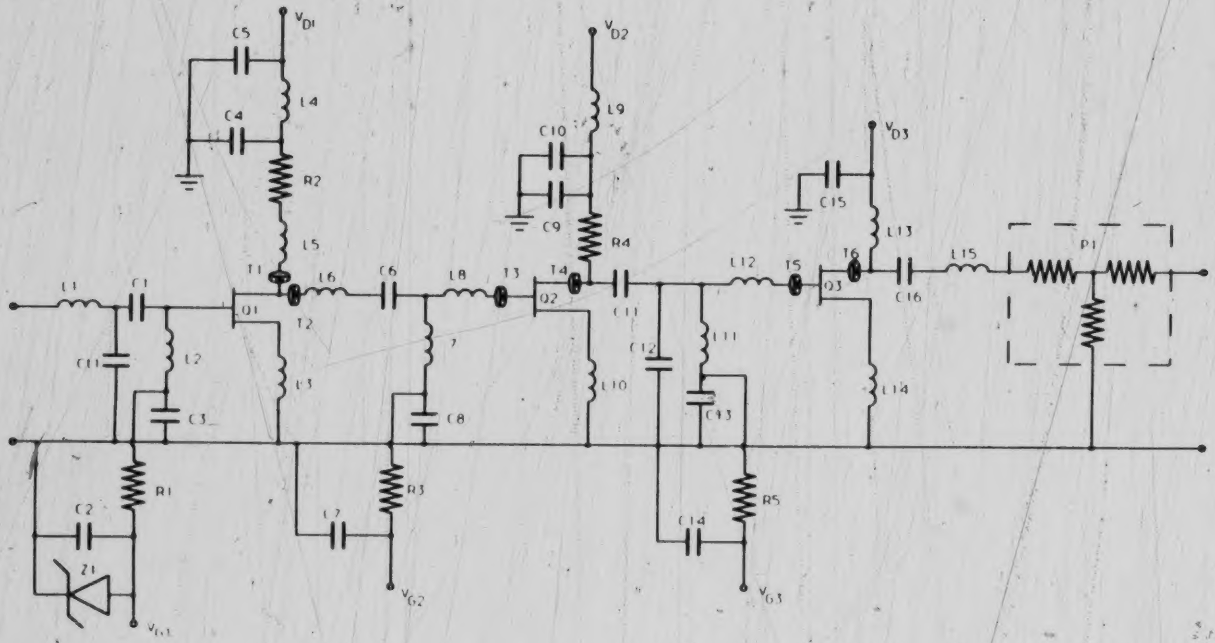

V_D1
C5
L4
C4
R2
L5
T1
T2
L1
C1
Q1
Ct1
L2
C3
L3
Z1
C2
R1
V_G1
L6
C6
7
C8
L8
T3
C7
R3
V_G2
V_D2
L9
C10
C9
R4
T4
Q2
L10
C11
C12
L11
C13
L12
C14
R5
V_G3
T5
Q3
T6
V_D3
C15
L13
L14
C16
L15
P1

Q1-NE32000
Q2, Q3-NE32084

Ct1-0.2-2.5pF
C1-3pF
C2, C7, C14, C15-680pF
C3, C5, C8, C10, C13-22pF
C4, C6, C9, C11-0.5pF
C12, C16-1.0pF

L1-13.3nH
L2, L4, L7, L9, L11-25nH
L3-3.5nH
L5-4.4nH
L6-5.5nH
L8-12nH
L10, L14-1.0nH
L12-23.5nH
L13-12.4nH
L15-1.7nH

R1, R3, R5-1000Ω
R2-50Ω
R4-100Ω

P1-6dB pad

T1 - T6-Ferromagnetic Toroid

Z1- 1N4627

Figure 2.5.2 L-Band LNA Schematic

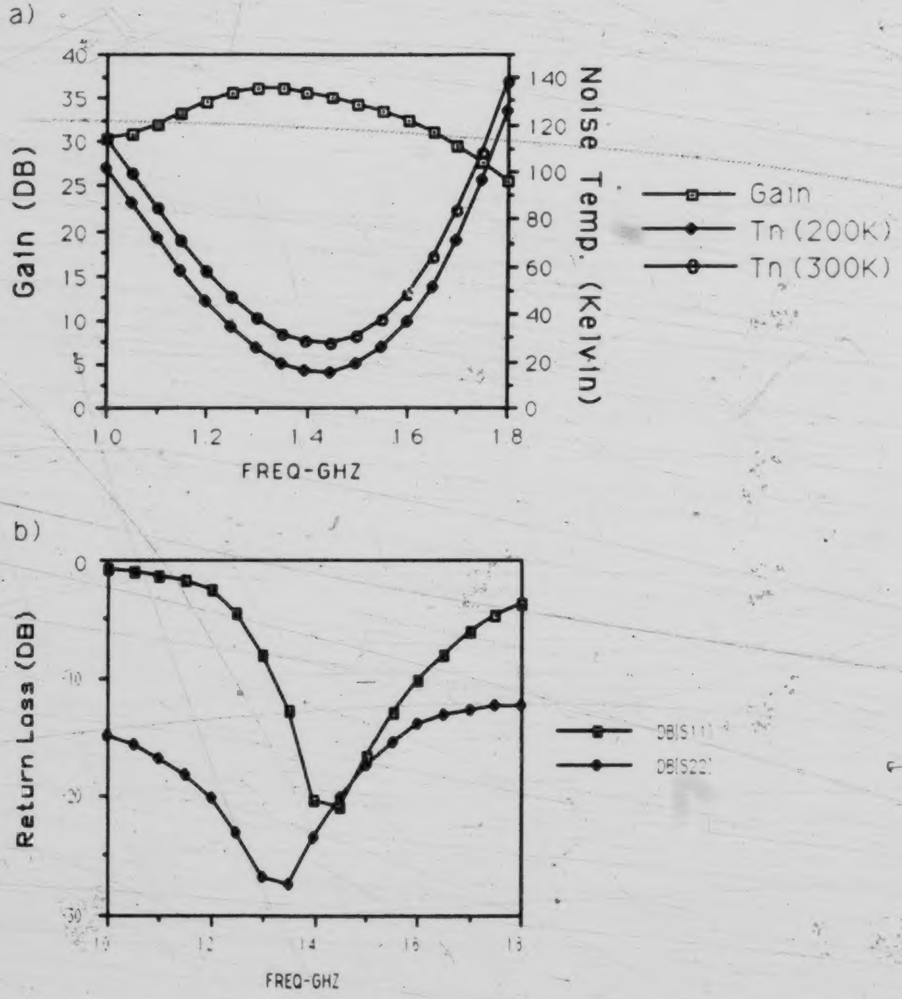

Figure 2.5.3: LNA performance obtained from Touchstone®. a) Gain and noise temperature, b) Input and output return loss.

The performance limits specified for the Monte Carlo analysis of this LNA design were:

$34.5 \le \text{Gain} \le 36.5$ dB (with 6 dB pad)

$T_N < 35$ K

$\Gamma_{IN} < -10$ dB.

Each component was perturbed randomly one hundred times by up to 10%. The analysis showed that the LNA is particularly sensitive to variations of four components: L1, L2, L12, and Ct1, which respectively had 55, 60, 46, and 26 successful trials each. The sensitivity to the inductor variations was not considered a problem because RF coils are easily tunable. The capacitor, Ct1, was made tunable for this very reason.

2.6 Conclusions

This chapter gives a description of the RF theory required to perform an LNA design. A design methodology to implement the theory is outlined and a program to serve as a design tool was described. Finally, a prelimary LNA design at 1.4 GHz was produced which, when modelled on Touchstone®, achieved the given design requirements. Later in the thesis it will be shown that modifications to the design are necessary for thermal and mechanical purposes as well as to compensate for model inaccuracies. Ultimately, the validity and limitations of the Touchstone® circuit model will be determined.

Chapter 3: Thermal Integration and LNA Fabrication

3.0 Introduction

An initial RF design for an LNA was provided in chapter 2. However, in that design, the thermal problems associated with cooling only a particular component were not fully dealt with. This chapter will first discuss the theory of thermoelectricity and the limitations of thermoelectric refrigerators, particularly the refrigerator employed in this project. Most importantly, the integration of the RF design with the thermal design will be carried out. This involves keeping the heat load on the refrigerator down to acceptable levels while maintaining RF signal paths. All three heat transfer mechanisms (conduction, radiation and convection) must be considered. Also, the thermal resistance from the HEMT to the cold surface of the refrigerator must be minimal in order to operate the HEMT at the lowest possible temperature. This necessitates the design of a unique HEMT carrier which must meet both thermal and RF criteria. Ultimately, an LNA enclosure will be produced which addresses all the above concerns.

3.1 Thermoelectricity

The Peltier effect was discovered in 1834 by Jean Peltier. He found that passing an electrical current in a particular direction through the junction of two dissimilar conductors produced a cooling effect. Also, when passed in the opposite direction, the current resulted in a heating effect quite distinct from resistive Joule heating.

Peltier's discoveries came shortly after Thomas Seebeck had discovered that an electric potential could be created by heating the junction between two metals. In 1885, William Thompson (later Lord Kelvin) was able to derive the relationship between the two effects using thermodynamic principles as well as predicting a third one, the Thompson effect, which is the absorption or evolution of heat when a current flows in the presence of a temperature gradient.

Figure 3.1.1 represents a simple thermoelectric circuit with conductors a and b and junctions at A and B. If a temperature difference, ΔT, is established between points A and B an electric potential, V, is evident between points C and D. This leads to the definition of the differential Seebeck coefficient or thermoelectric power as follows [36]:

$$\alpha_{ab} = \frac{V}{\Delta T} \qquad (3.1.1)$$

where α_{ab} is a function of materials a and b.

Now assume the two junctions are kept at the same temperature and a battery is placed between C and D, forcing a current I to flow through the circuit. In this case, if junction A is heated at a rate q, junction B must be cooled at the same rate q. The differential Peltier coefficient is then defined as [36]:

$$\pi_{ab} = \frac{q}{I} \qquad (3.1.2)$$

The Thompson coefficient can be defined for each conductor if in addition to the current I, there also exists a temperature gradient dT/dx. This leads to a cooling or heating at the rate dq/dx per unit length. The Thompson coefficient τ is then defined as [36]:

$$\tau = \frac{dq/dx}{I\ dT/dx} \qquad (3.1.3)$$

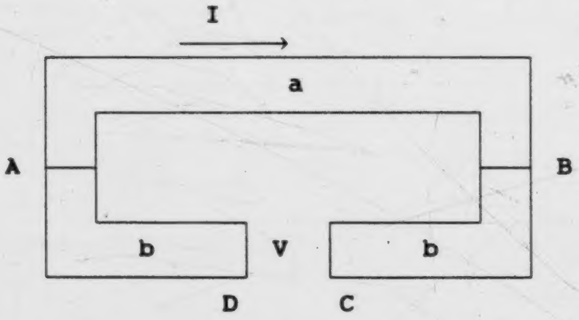

Figure 3.1.1: Simple Thermoelectric Circuit

Thompson derived [38] the following two equations known as the Kelvin relations which interrelate all three thermoelectric coefficients:

$$\pi_{ab} = \alpha_{ab}T \qquad (3.1.4)$$

and

$$\tau_a - \tau_b = T\frac{d\alpha_{ab}}{dT} \qquad (3.1.5)$$

where T is the absolute temperature of the junction.

A simple thermoelectric refrigerator is illustrated in figure 3.1.2.a. It comprises a cold junction at temperature T_c, a hot junction at temperature T_h, and thermoelectric materials A and B having physical properties α_a, ρ_a, k_a and α_b, ρ_b, k_b referring to the Seebeck coefficient, electrical resistivity, and thermal conductivity respectively. The materials have lengths L_a and L_b and cross-sectional areas A_a and A_b. The contact resistances between the materials and the junctions will be assumed to be negligible.

A simple explanation of the Peltier effect can be given in terms of semiconductor physics if one considers materials A and B in figure 3.1.2.a. to be N- and P-type semiconductors respectively, as shown in figure 3.1.2.b. In metal, the Fermi level is close to the top of the electron energy distribution. In semiconductors the Fermi level is in the forbidden gap. Current is carried by holes near the top of the valence band in P-type semiconductors and by electrons in the conduction band of N-type semiconductors.

As electrons flow from left to right through the circuit, electrons must gain energy at J_3 to rise from the Fermi level of the metal to the conduction band of the N-type semiconductor. This rise in energy occurs at the expense of thermal energy resulting in cooling. At J_4, electrons must jump downward in energy to the Fermi level of the metal resulting in the generation of thermal energy. Similarly heat is produced at J_1 and taken up at J_2. Thus,

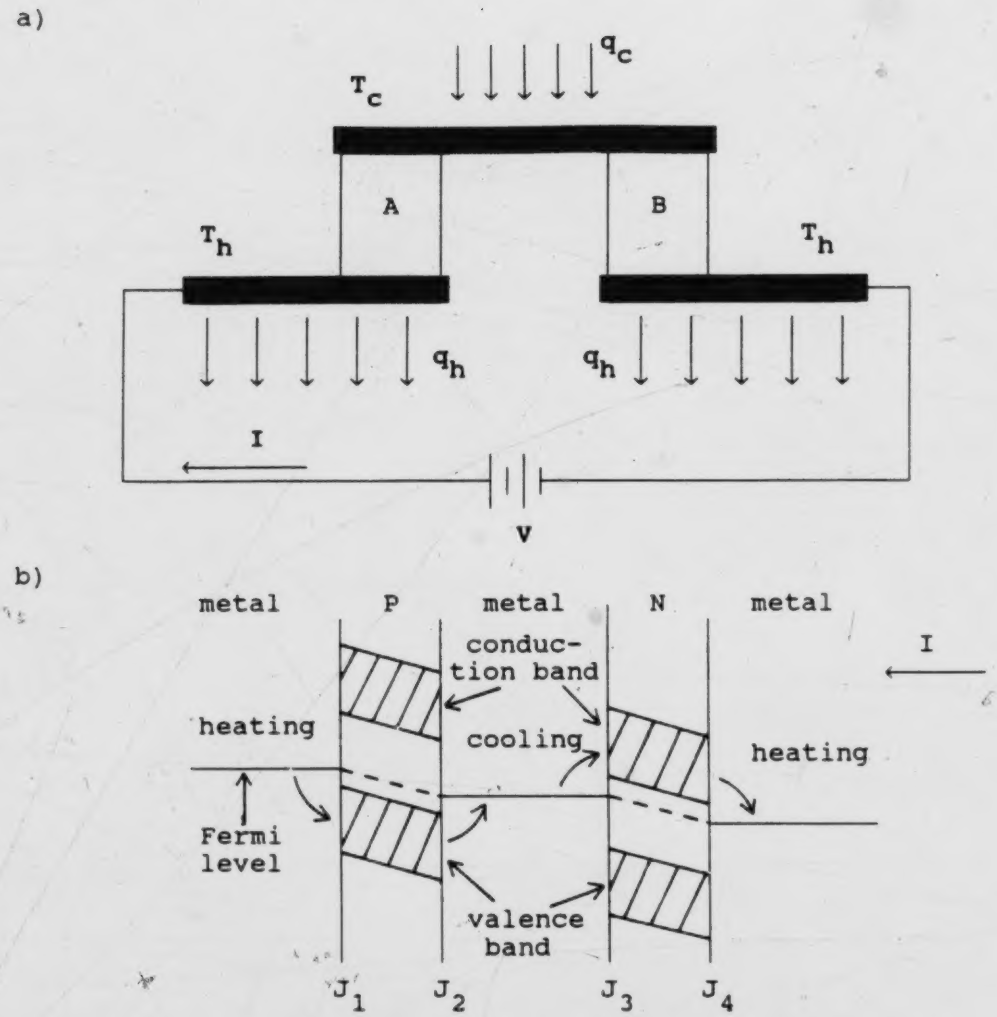
a)
q_c
T_c
A
B
T_h
T_h
q_h
q_h
I
V
b)
metal
P
metal
N
metal
I
conduc-
tion band
heating
cooling
heating
Fermi
level
valence
band
J_1
J_2
J_3
J_4

Figure 3.1.2: Simple Thermoelectric Refrigerator (metal represented by solid bar): a) physical configuration. b) energy level diagram.

the net effect of the current is to cool the inner junctions, J_2 and J_3, and to heat the outer junctions, J_1 and J_4. If the current were to be reversed, the opposite would hold true.

The following derivation [36] will lead to two parameters which determine the effectiveness of a particular thermoelectric refrigerator: the coefficient of performance (COP), which is the ratio of the cooling power to the input power, IV, and the maximum obtainable temperature difference between the hot and cold junctions (ΔT_{max}).

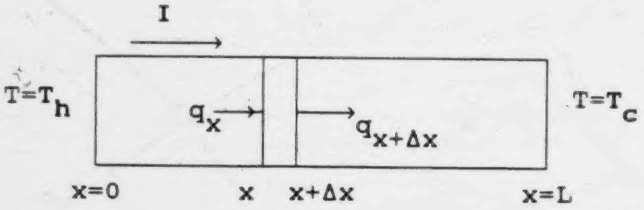

Figure 3.1.3: One Branch of Thermoelectric Refrigerator

Consider only one branch of the junction as shown in figure 3.1.3 with boundary conditions imposed such that at $x=0$, $T=T_h$ and at $x=L$, $T=T_c$. The heat quantities entering the section Δx at point x and leaving at $x+\Delta x$ through conduction, given by Fourier's law [37] are

$$q_x = \left.\frac{-kAdT}{dx}\right|_{x} \qquad (3.1.6)$$

and

$$q_{x+\Delta x} = \left.\frac{-kAdT}{dx}\right|_{x+\Delta x} \qquad (3.1.7)$$

respectively (here "k" is the thermal conductivity). The heat generated within the section through Joule heating is given by:

$$q_J = \frac{I^2 \rho \Delta x}{A}. \tag{3.1.8}$$

Heat balance requires that the net flow of heat into a volume plus the heat generated inside the volume be equal to the rate of increase of internal energy inside that volume. In this case we are dealing with a steady-state condition (ie. the temperatures are constant) which means that there is no rise in internal energy. Therefore:

$$q_x - q_{x+\Delta x} + q_J = 0, \tag{3.1.9}$$

which leads to the differential equation:

$$\frac{d^2T}{dx^2} + \frac{I^2\rho}{kA^2} = 0. \tag{3.1.10}$$

Application of the boundary conditions results in the solution being a parabolic temperature distribution through the material as given by:

$$T(x) = -\left(\frac{I^2\rho}{2kA^2}\right)x^2 - \left(\frac{\Delta T}{L} - \frac{I^2\rho L}{2kA^2}\right)x + T_h, \tag{3.1.11}$$

where $\Delta T = T_h - T_c$.

The heat flowing out of the material at $x = L$ can then be evaluated using Fourier's law:

$$q_L = -kA \left.\frac{dT(x)}{dx}\right|_L = \frac{I^2R}{2} + K\Delta T, \qquad (3.1.12)$$

where $R = \rho L/A$ and $K = kA/L$, the electrical resistance and the thermal conductance of the material respectively. This result is not surprising as it represents half the Joule heat dissipated in the branch plus the conductive heat due to the temperature difference.

If we now consider the simple refrigerator given in figure 3.1.2, the net heat absorbed by the cold junction, or the cooling power, is:

$$q_c = \alpha I T_c - \frac{I^2R}{2} - K\Delta T, \qquad (3.1.13)$$

where $\alpha I T_c$ is the Peltier heat (πI), $\alpha = |\alpha_a| + |\alpha_b|$ (in a thermoelectric refrigerator α_a and α_b are opposite polarities), $R = \rho_a L_a/A_a + \rho_b L_b/A_b$, and $K = k_a A_a/L_a + k_b A_b/L_b$. The voltage across the battery is

$$V = \alpha\Delta T + IR \, , \qquad (3.1.14)$$

and the input power to the junction is

$$P_{IN} = IV = I^2R \pm \alpha I \Delta T. \qquad (3.1.15)$$

The coefficient of performance (COP) then becomes:

$$\text{COP} = \Phi = \frac{\alpha I T_c - I^2 R/2 - K\Delta T}{I^2 R + \alpha I \Delta T}. \qquad (3.1.16)$$

Two values of current I are important. One is the value resulting in the maximum COP or operating efficiency for a given temperature difference, the other is the current allowing the maximum cooling power. The first current, I_Φ, is determined by differentiating equation 3.1.16 and setting it to zero. This yields, after some manipulation [36],

$$I_\Phi = \frac{\alpha\Delta T}{R(\sqrt{1 + ZT_M} - 1)}, \qquad (3.1.17)$$

where T_M is the mean temperature, $(T_h+T_c)/2$, and $Z = \alpha^2/KR$. The resulting maximum COP is then given by:

$$\Phi_{max} = \frac{T_c}{T_h - T_c} \times \frac{\sqrt{1 + ZT_M} - T_h/T_c}{\sqrt{1 + ZT_M} + 1}. \qquad (3.1.18)$$

As Z increases towards infinity, Φ becomes simply the Carnot efficiency for a refrigerator as given by $T_c/(T_h-T_c)$.

The current required for obtaining the maximum cooling power is determined by differentiating equation 3.1.13 and setting it to zero, which yields:

$$I_q = \frac{\alpha T_c}{R}, \qquad (3.1.19)$$

and

$$\Phi_q = \frac{ZT_c^2/2 - (T_h - T_c)}{ZT_hT_c} \,. \qquad (3.1.20)$$

Now consider the case when there is no heat source. The COP (given by equation 3.1.20) will drop to zero resulting in the following relationship:

$$(T_h - T_c)_{max} = \Delta T_{max} = \frac{ZT_c^2}{2} \,. \qquad (3.1.21)$$

It is now clear that the variable Z controls both the maximum attainable temperature difference as well as the COP at any lower ΔT. For this reason Z is called the thermocouple figure of merit and is a function of the material's dimensions and physical characteristics. It is the thermal, electrical, and thermoelectrical properties of the material, which vary with temperature, that ultimately determine the lowest temperature the refrigerator can achieve ($Z(T) \propto \alpha(T)^2/\rho(T)k(T)$).

Typically, thermoelectric refrigerators are constructed using p and n type semiconductors. Although metals normally have a small ρ, they also have a large k ($\rho k \approx$constant in metals) and Seebeck coefficients of the order of 10μV/deg compared with up to several millivolts per degree for semiconductors [36]. The best known thermoelectric materials for use in the temperature range between 200 and

300 Kelvin are bismuth-telluride alloys (Bi_2Te_3). Figure 3.1.4 gives a plot of the thermoelectric figure of merit versus temperature for several materials.

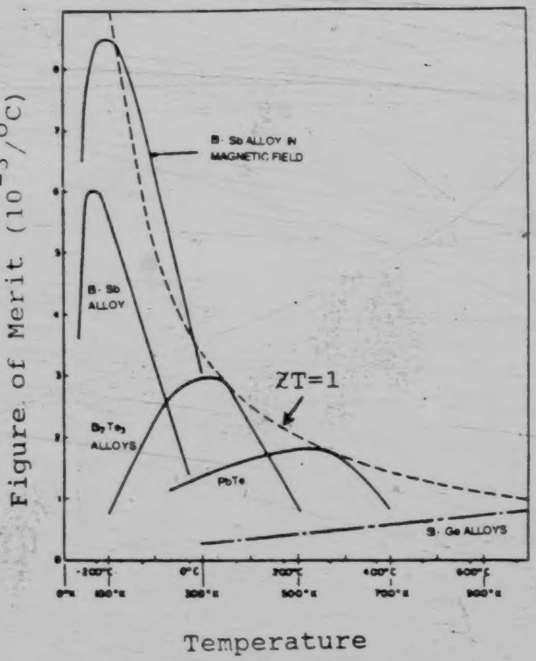

Figure 3.1.4: Variation of thermoelectric figure of merit with temperature for various materials. Modified from Wolfe [38].

It has been found [38] that at low temperatures (less than 200K), thermoelectric cooling can be enhanced in the presence of an appropriately aligned magnetic field. As shown in figure 3.1.4, very large figures of merit can be realized down to tens of Kelvin using this thermomagnetic effect. However, practical refrigerators using this technology are very inefficient and bulky and, therefore, lose their advantage over mechanical refrigerators.

McCormick and Brauer [39] showed that a combined thermoelectric-thermomagnetic refrigerator would require 10kW of power to pump only 1mW of heat from 70K to 297K. Also, liquid cooling would be necessary to keep the hot side at 297K.

It is possible to achieve greater temperature differentials by employing multistage thermoelectric refrigerators. Several thermoelements can be used in parallel in a single stage, the number of which determines the cooling capacity of that stage. Multistage, or cascaded, Peltier devices are normally arranged such that stages contain more elements the closer they are to the refrigerator hot plate. This configuration is employed because the warmer stages not only have to sink heat from the source and their own Joule heat, but also the heat generated by all the preceding stages. The individual thermoelements are normally connected in series electrically. Figure 3.1.5 gives an example of how a two stage refrigerator might be configured thermally and electrically.

In determining the COP of a cascaded refrigerator it is assumed that each stage has a temperature difference across it equal to $(T_h-T_c)/n$, where n is the number of stages. Also, the COP of each individual stage, when there is a current I_Φ, is assumed to be equal to $n(\Phi_1+1/2)-1/2$ [36], where Φ_1 is the COP for a single junction operating over the range from T_h to T_c. The COP for an n stage device is then:

$$\Phi_n = \frac{1}{(1 + 1/\Phi_1)^n - 1} . \qquad (3.1.22)$$

If there is an infinite number of stages, equation 3.1.22 becomes [36]:

$$\Phi_\infty = \frac{1}{\exp[1/(\Phi_1 + 1/2)] - 1} . \qquad (3.1.23)$$

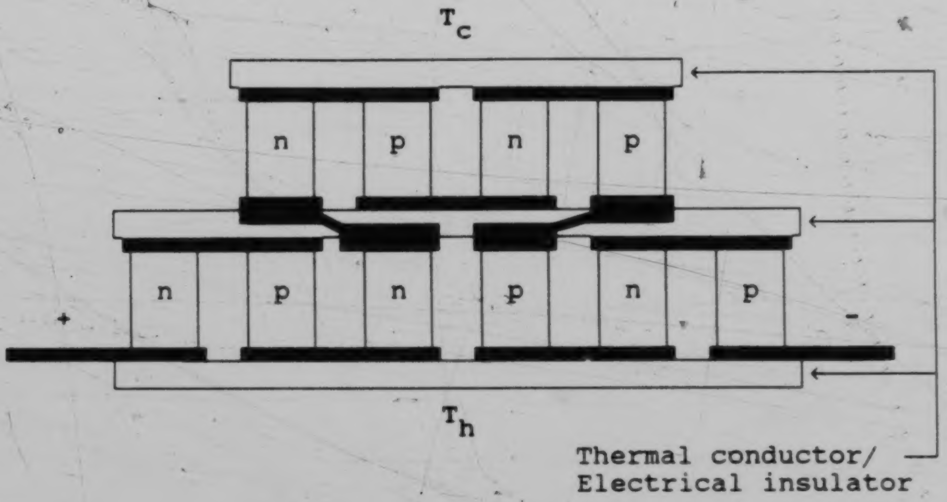

T_c
n
p
n
p
n
p
n
p
n
p
+
-
T_h
Thermal conductor/
Electrical insulator

Figure 3.1.5: Typical Cascaded Thermoelectric Refrigerator

In order to get useful results, the temperature dependence of the thermoelectric parameters must be taken into account. Goldsmid [36] shows that fairly accurate results can be obtained using the following equation for the thermoelectric figure of merit:

$$Z \cong \frac{\langle\alpha_2 - \alpha_1\rangle^2}{[\langle k_1\rho_1\rangle^{1/2} + \langle k_2\rho_2\rangle^{1/2}]^2} , \qquad (3.1.24)$$

where <> denotes averaging between the values at the hot and cold temperatures of the junction. Substituting equation 3.1.24 into equation 3.1.18 gives the COP of one stage in an infinite stage device as follows:

$$\Phi_{n1} = \frac{T}{\delta T}\,\frac{\sqrt{1 + ZT} - 1}{\sqrt{1 + ZT} + 1} = \frac{T}{\delta T}\,\varepsilon(T), \qquad (3.1.25)$$

where δT is the infinitesimal temperature difference of the stage. Equation 3.1.23 then becomes [36]:

$$\Phi_\infty = \frac{1}{\exp\left[\int_{T_c}^{T_h} \frac{dT}{T\varepsilon(T)}\right] - 1} . \qquad (3.1.26)$$

Now consider a cascaded refrigerator where the hot side is at some lower temperature, T_h', where Z is very small, such that $\sqrt{1+ZT} \cong 1+ZT/2$ and $\varepsilon(T) \cong ZT/(ZT+4)$. It can be shown that equation 3.1.26 becomes:

$$\Phi_\infty = \frac{T_c}{T_h'\exp[4(T_h' - T_c)/ZT_h'T_c] - T_c} . \qquad (3.1.27)$$

As T_c decreases, Φ_∞ quickly becomes very small ($\Phi_\infty \propto T_c/\exp(1/T_c)$), and the power required to run the device increases in inverse proportion to Φ_∞. Even in this ideal case of an infinite cascade operating at the optimum current, the required operating power soon becomes prohibitively large at low T_C values. This results in the need for complex heat sink mechanisms and creates severe problems with thermal expansion, electrical contacts, fabrication of large assemblies, and high power densities [40]. In practice, the advantages of thermoelectric devices over other refrigerators quickly disappear for very large temperature differences.

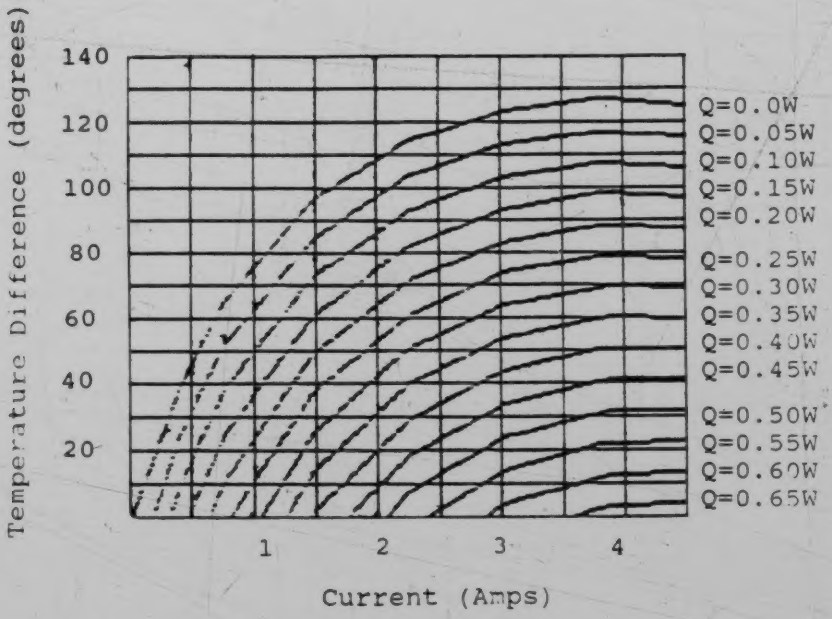

Figure 3.1.6: Temperature difference (ΔT) versus current of Marlow MI6030 6 stage refrigerator for various heat loads. Modified from Marlow [7].

Marlow Industries [7] produces several multistage Peltier devices including a six stage cooler (MI6030) which achieves a ΔT_{max} of 130° in a vacuum (10^{-6} Torr) with about

25 Watts of input power. The refrigerator is very suitable for this LNA application because of its small dimensions and a cooling capacity commensurate with the requirements. Its total volume is less than 16ml and the cold plate surface area is 27 square millimeters. The temperature differential decreases by about 10 degrees for every additional 50 milliwatts of heat load (ie. about 200K/W). Figure 3.1.6 gives the curves, supplied by Marlow Industries, of ΔT versus current for various heat loads.

3.2 Thermal Model

Optimizing LNA performance requires operating the HEMT at the lowest possible temperature. Therefore, the heat load on the Peltier device must be minimized while maintaining the RF performance of the HEMT. The thermal model must incorporate heat loading due to the three main mechanisms of heat transfer: conduction, convection, and radiation. Also, Joule heat produced by the HEMT and the thermal resistance of the medium between the HEMT and the refrigerator (R_{car}) must be taken into account.

Figure 3.2.1 gives a pictorial representation of the heat transfer mechanisms which exist, along with the analogous electrical model. Temperatures in the model are analogous to nodal voltages, thermal resistances to electrical resistances, and heat flow to electrical current. It must be noted that the radiation resistance, R_{rad}, is given for a fixed temperature difference since radiation heat transfer is actually proportional to temperature to the fourth power.

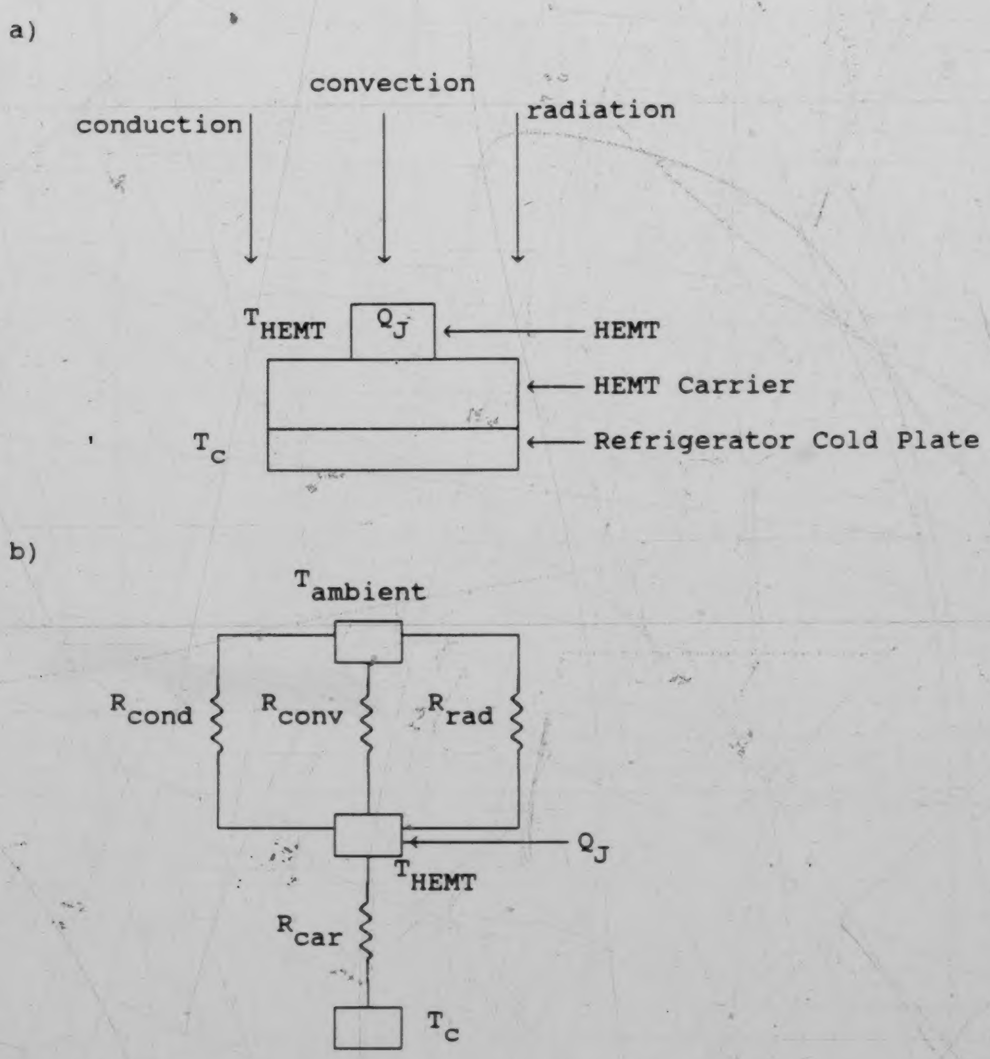
a)
convection
conduction
radiation
T_{HEMT}
Q_J
HEMT
HEMT Carrier
T_C
Refrigerator Cold Plate
b)
$T_{ambient}$
R_{cond}
R_{conv}
R_{rad}
Q_J
T_{HEMT}
R_{car}
T_C

Figure 3.2.1: Heat Loading on Peltier Device. a) Physical model b) Electrical Equivalent Circuit

An expression for the HEMT temperature which incorporates all of the above parameters can be derived as follows. The total heat load on the refrigerator cold plate is

$$\begin{aligned} Q_T &= Q_{rad} + Q_{conv} + Q_{cond} + Q_J \\ &= (T_{amb} - T_{HEMT})/R_T + Q_J \end{aligned} \qquad (3.2.1)$$

where $R_T = (R_{rad}^{-1} + R_{conv}^{-1} + R_{cond}^{-1})^{-1}$. The HEMT temperature is then given by:

$$T_{HEMT} = T_c + Q_T R_{car} \qquad (3.2.2)$$

However, the cold plate temperature, T_c, is also a function of the heat load Q_T.

$$T_c \cong T_{amb} - \Delta T_{max} + 200K/W \times Q_T \qquad (3.2.3)$$

Substituting equations 3.2.1 and 3.2.3 into equation 3.2.2 yields:

$$T_{HEMT} = \frac{R_T}{R_T + R_{car} + 200}\left[T_{amb} - \Delta T_{max} + (R_{car} + 200)(T_{amb}/R_T + Q_J)\right] \qquad (3.2.4)$$

In the actual design it is desired to make R_T as large as possible to minimize the heat load and R_{car} as small as possible to minimize the temperature drop across the carrier. When designed properly, $R_T \gg R_{car} + 200$ and $R_{car} \ll$

200; thus equation 3.2.4 reduces to

$$T_{HEMT} = T_{amb} - \Delta T_{max} + 200(T_{amb}/R_T + Q_J) \qquad (3.2.5)$$

For the purpose of thermal design a target HEMT temperature of 200K was established. Assuming the ambient temperature to be 300K, $\Delta T_{max}=130^{\circ}$, and $Q_J=20mW$ (manufacturer's data were specified at 2V and 10mA), the minimum combined thermal resistance allowed for conduction, convection, and radiation is (from equation 3.2.5) 2.3K/mW. This results in an allowed heat load of about 43mW ($Q=\Delta T/R$) due to those three mechanisms. The remaining sections of this chapter will deal with producing a thermal design which meets the heat load objective without compromising the RF performance.

3.2.1 HEMT Carrier Design

Thermal resistance in the path from the HEMT to the cold plate of the Peltier device will result in a temperature drop and hence a higher HEMT temperature. At the same time, the Peltier device has some finite RF impedance that must be taken into account or compensated for. Therefore, a mechanism is required which will efficiently transfer heat from the HEMT to the refrigerator without degrading the RF performance. This can be realized in the form of a HEMT carrier made from a thermally conductive material.

The first step in the design of the HEMT carrier was to try to measure the RF impedance of the Peltier device. Because of its complex mechanical structure it was not possible to measure its impedance using any kind of fixture with microwave connectors. However, it was possible to measure its impedance up to 100 MHz with a vector impedance meter (HP4815A). The impedance meter showed that the device was capacitive (≈1.7pf) up to 100 MHz, the upper limit of the instrument. This was not surprising due to the parallel plate structure of the cooler. It was consequently assumed to be capacitive at L-band, with the result that any circuitry on top of the refrigerator would effectively be at RF ground at L-band.

Touchstone® was used to determine how much capacitance to ground could be tolerated at each of the HEMT terminals. It was found that within reason, gate capacitance could be tolerated because it is effectively in parallel with the tuning capacitor, C_{T1}. Source capacitance proved to be the most detrimental to performance and stability. Intuitively this is expected since source inductance transforms to real input impedance and it is reasonable to assume that a source capacitance transforms to a negative real input impedance. A source capacitance of less than .1pF was found to be tolerable.

Several materials were investigated for use as the HEMT carrier. Table 3.2.1.1 gives a breakdown of the critical characteristics (thermal conductivity, k; relative dielectric constant, ε_r) and the resulting parameters (thermal resistance, R_{TH}; temperature differential across carrier, ΔT; source capacitance, C_S) assuming the carrier to have dimensions 5.2mm x 5.2mm x 1mm, the source surface area on the carrier to be 4mm^2, and a 30mW heat load.

Material	Alumina	Teflon	Fused Quartz	Crystalline Quartz	
				|| Z-axis	⊥ Z-axis
k (W/m/K)*	55	0.35	1.14	16.4	9.5
ε_r	9.75	2.33	3.8	4.58	4.70
R_{TH} (K/W)	0.85	106	41.2	2.26	3.89
ΔT (K)	0.03	3.2	1.2	0.07	0.12
C_S (pF)	0.27	0.08	0.11	0.13	0.17

*Thermal conductivities [41] given at 200K for all but teflon [42].

Table 3.2.1.1: Thermal and Electrical Properties of Various Dielectrics.

Crystalline quartz (parallel to Z-axis) was chosen for the design. It has good thermal conductivity at 200K (easily meeting the requirements for equation 3.2.5) and a reasonably low dielectric constant, allowing for a sufficiently small parasitic source capacitance. The technology for metal deposition on quartz also exists in the Electrical Engineering department at the University of Alberta, allowing for 'in house' fabrication of the carriers. Polished quartz discs (1 inch diameter, 1.5 mm thickness) with crystal orientation parallel to the Z axis were purchased [43]. Maintaining the previous assumptions for source surface area, the source capacitance is 0.1pF and the temperature drop across the carrier is 0.1K, both satisfactory results.

It is necessary to have a good microwave conductor deposited on the quartz in order to minimize conductive losses on the carrier. Gold was chosen because it does not deteriorate due to oxidation, although its conductivity is not quite as good as copper or silver. It is well known that at high frequencies nearly all the current flows in a thin layer on the surface of the conductor. The thickness of the layer is normally taken to be several skin depths [44]. Skin depth is given by the following relationship:

$$\delta = \frac{1}{\sqrt{\pi f \mu \sigma}} \qquad (3.2.1.1)$$

where μ is the magnetic permeability and σ is the conductivity. The skin depth for gold at 1.4 GHz is 1.8μm. Therefore a conductor thickness of 7.5μm (>4δ) should be sufficient.

Several steps are involved in obtaining a 7.5μm layer of gold on a disc of quartz. First, the disc must be cleaned extremely well. Oxygen plasma etching was used for this purpose. A thin layer of chromium (500-1000Å) is then required to act as an adhesive between the gold and the quartz. This layer is evaporated onto the quartz in a vacuum chamber. While in the chamber, a thin layer of gold

(≈.2μm) is then evaporated on top of the chromium. The entire 7.5μm is not deposited through evaporation because the process is very wasteful and hence expensive. Electroplating was employed to deposit the remaining 7.3μm of gold onto the quartz.

A problem was encountered in the initial attempts at electroplating the gold. When the gold layer reached a thickness of about 5μm, the chromium/gold film peeled away from the quartz. It appeared as if the gold solution was reacting with the chromium layer. After further investigation it was determined that during the evaporation processes chromium was deposited over the entire surface area, upon which a layer of gold was then deposited. This resulted in the chromium being directly exposed to the electroplating solution, with which it is believed to have reacted. Figure 3.2.1.1 shows schematically how the evaporation process was initially set up and the resulting film structure.

A method of overcoming this peeling problem was developed. It entailed using a holder for the crystal in the evaporation chamber which prevented deposition right to the edge of the disc. Figure 3.2.1.2 shows the new configuration and film structure achieved with it. The masking created by the overhang on the holder prevented the chromium from being deposited right to the edge of the quartz. The gold evaporates more diffusely than chromium

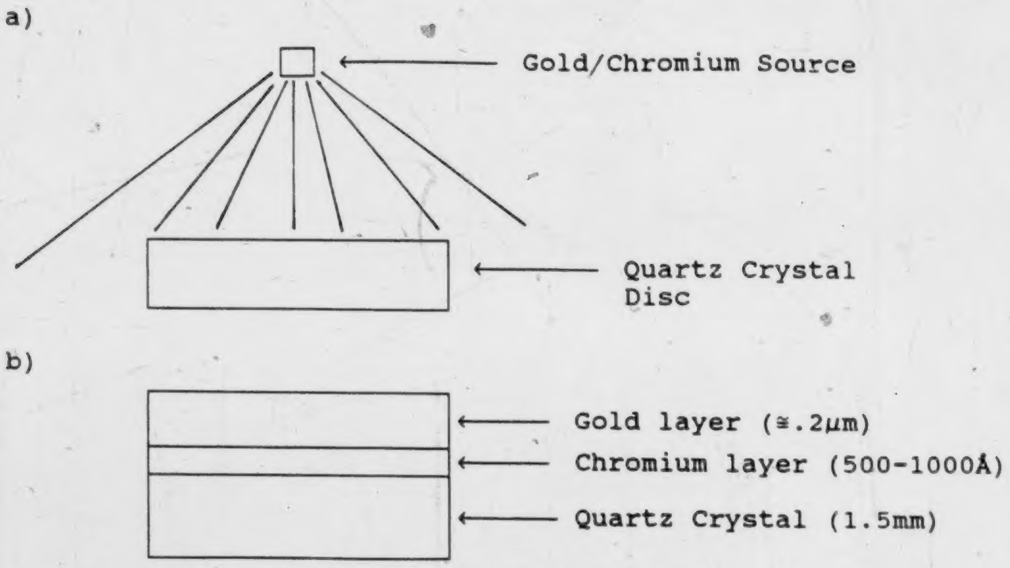
a)
Gold/Chromium Source
Quartz Crystal Disc
b)
Gold layer (≅.2μm)
Chromium layer (500-1000Å)
Quartz Crystal (1.5mm)

Figure 3.2.1.1: Initial Evaporation Technique:a) Schematic representation of initial configuration. b) Resulting cross-section of films on quartz.

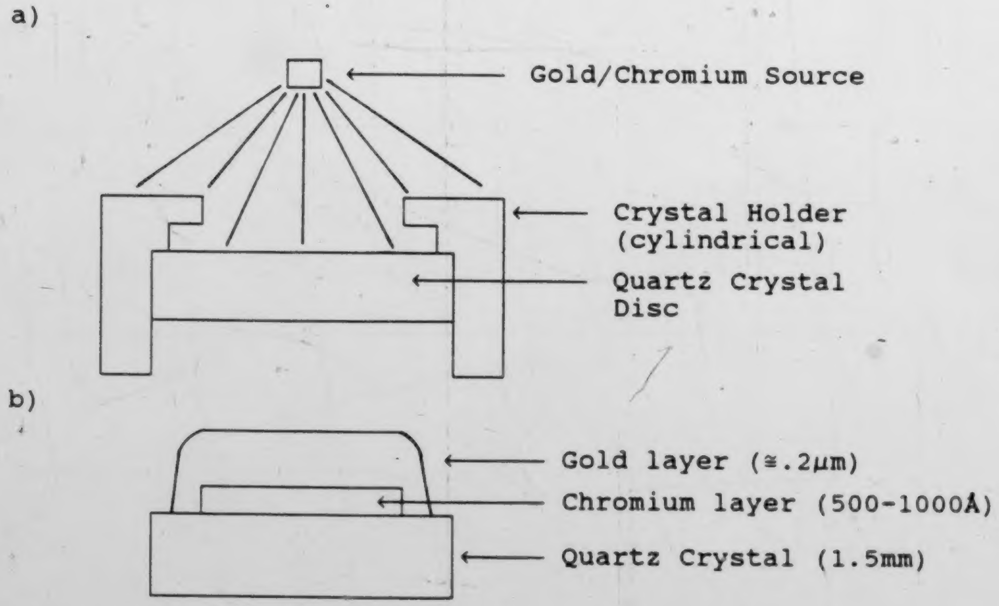
a)
Gold/Chromium Source
Crystal Holder (cylindrical)
Quartz Crystal Disc
b)
Gold layer (≅.2μm)
Chromium layer (500-1000Å)
Quartz Crystal (1.5mm)

Figure 3.2.1.2: Modified Evaporation Technique:a) Schematic representation of final configuration. b) Resulting cross-section of films on quartz.

and thus totally encases it. Hence the chromium is shielded from the plating solution. This deposition technique resulted in a 7.5μm layer of gold being successfully electroplated.

Apart from sustaining a thermal path from the HEMT to the Peltier device, the HEMT carrier must offer a means for transmitting the RF signal to the HEMT and on to subsequent stages, as well as provide for dc biasing. The gate serves as the input to the HEMT in its common source configuration. As shown by equation 2.2.9, any loss (1/G) in series with the input not only contributes its own noise temperature additively, but also increases the noise temperature of subsequent stages by a factor of 1/G (G<1).

The capacitor in series with the HEMT input (C1) is a convenient means for providing a thermal block in the input. One terminal of the capacitor must be mounted on the HEMT carrier. As a result, the structure chosen for the capacitor should allow for thermal expansion both vertically and horizontally. Modelling on Touchstone® determined that the exact value of capacitance is not critical as long as a minimum value of 3pF is maintained. Because the capacitor is to be a lumped element, its physical length should be constrained to less than one twentieth of a wavelength at L-band (λ at 1.4GHz is 21cm) in order to eliminate transmission line effects.

Figure 3.2.1.3 shows the capacitive structure developed which meets the above criterion. The value of capacitance is sufficiently small to allow for the use of a free space dielectric ($\epsilon_r=1$). Free space is lossless and invulnerable

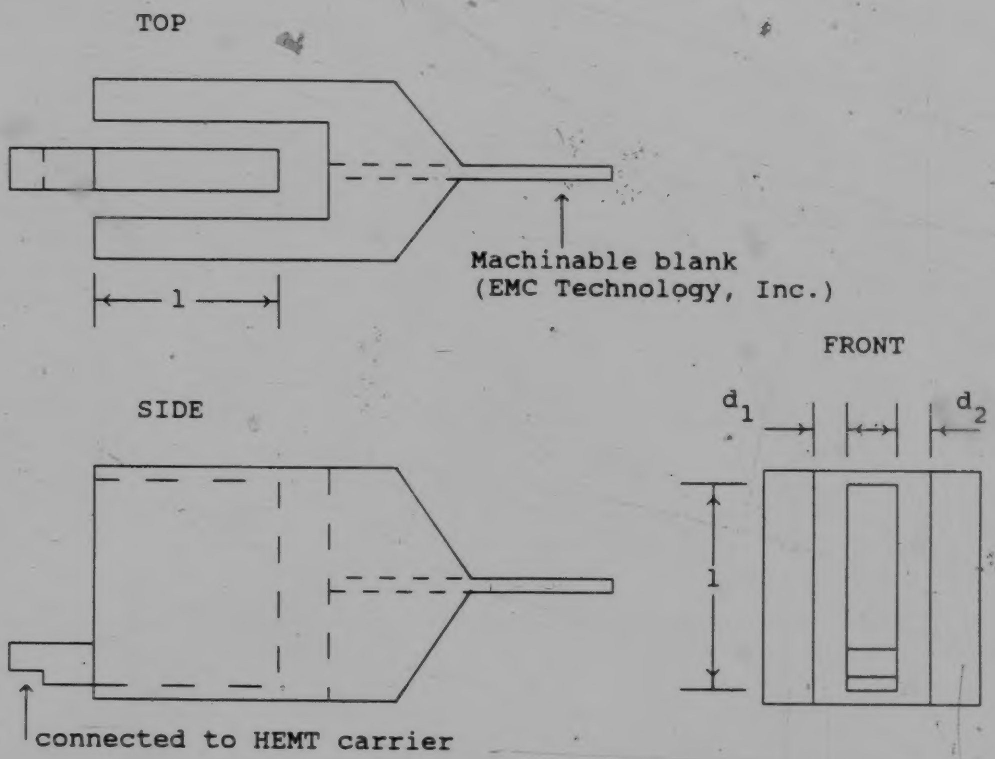
TOP
l
Machinable blank
(EMC Technology, Inc.)
FRONT
SIDE
d_1
d_2
l
connected to HEMT carrier

Figure 3.2.1.3: Thermal Blocking Input Capacitor

to thermal expansion. The nominal spacing, d, was chosen to be 0.25mm, a compromise between being too small for mechanical realizability and being too large to be considered a lumped element. The resulting dimension, l, required for a 3pF capacitor is 7.0mm ($<\lambda/20$). Ignoring fringing effects (which increase effective capacitance), the equation for the capacitance is

$$C_1 = \frac{\varepsilon_o l^2}{d_1} + \frac{\varepsilon_o l^2}{d_2} \qquad (3.2.1.2)$$

It can be shown that a minimum capacitance of 3pF results when $d_1=d_2$, allowing for inexact mechanical alignment. Also, the nature of the structure makes it insensitive to thermal expansion in the horizontal and vertical directions.

At room temperature chip GaAsFETs typically have half the thermal resistance to the channel of packaged GaAsFETs (100K/W versus 200K/W) [46]. Due to the similarity in structure between HEMTs and GaAsFETs, it is reasonable to assume that the same holds true for HEMTs. Consequently, the NE32000 chip HEMT was chosen to be used in the cooled first stage. Figure 3.2.1.4 gives the physical layout of the NE32000 chip HEMT.

Figure 3.2.1.5 shows the mask developed for the HEMT carriers. The gate capacitor terminal can either be soldered or attached with silver epoxy to the gate pad on the carrier. The notch on the capacitor terminal (figure 3.2.1.3) and the carrier pad itself allow for proper alignment of the terminal. Nine identical patterns are simultaneously produced on the one inch quartz disc as shown in figure 3.2.1.6. The disc is then diced into 5.2mmx5.2mm pieces using a saw suitable for precision glass or silicon wafer cutting (≈0.020" cutaway). Appendix 2.1 gives the

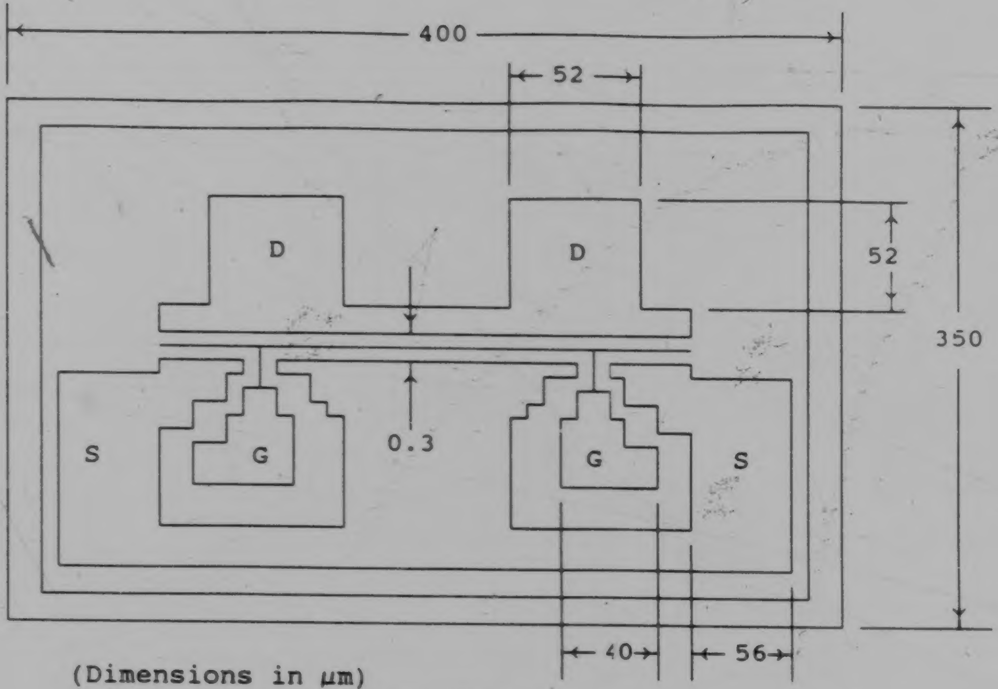
400
52
D
D
52
350
0.3
S
G
G
S
40
56

(Dimensions in μm)
Chip Thickness: 140 ∓ 10μm

Figure 3.2.1.4: Physical Layout of NE32000 Chip HEMT.

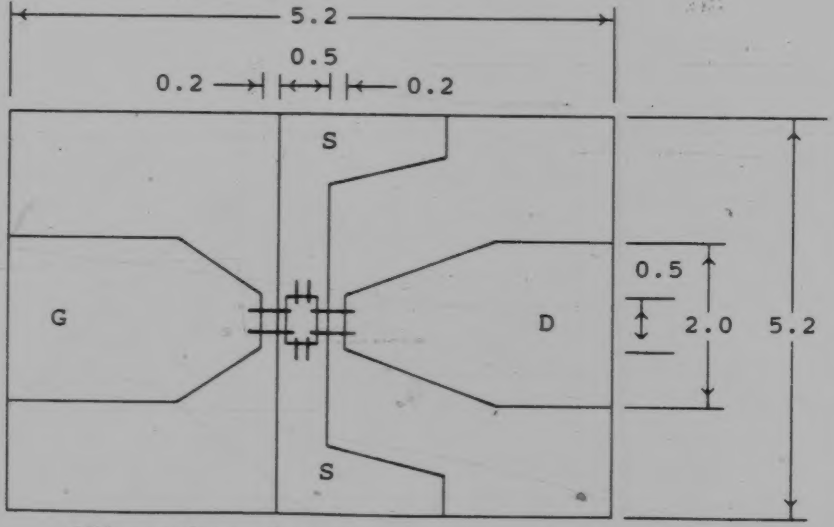
5.2
0.5
0.2
0.2
S
G
D
S
0.5
2.0
5.2

(Dimensions in mm)

Figure 3.2.1.5: Mask for Quartz HEMT Carrier With HEMT and Bonding Wire Positions.

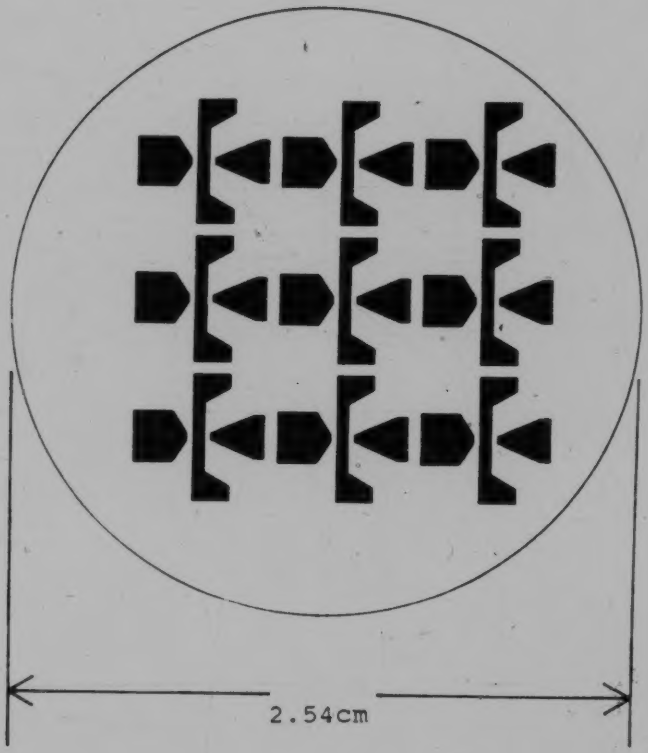

Figure 3.2.1.6: Mask for 9 quartz HEMT carriers.

procedure for etching the gold pattern on the quartz.

The manufacturer specifies 20μm diameter gold bonding wires using the thermocompression bonding technique. Data provided by NEC was given for two bonds each on the gate and drain and four on the source. The ultrasonic bonding machine at the Alberta Microelectronic Centre was fitted with the temperature control system necessary to perform thermocompression bonding.

Before bonding the HEMT, the gate capacitor terminal and inductors L2, L3, L10, and L14 (inductor specifications given in section 3.2.2) were attached. During the bonding procedure the carrier had to be heated to about 300°C, so any solder used had to have a higher melting temperature. The HEMT could then be mounted on the carrier using Epotek silver epoxy, a highly conductive (thermally and electrically) epoxy ideal for this purpose. Due to the extremely small size of the chip, great care had to be taken during this procedure. A good pair of tweezers and a microscope were essential.

3.2.2 Conduction Heat Load

It was not possible to use a capacitive thermal block in the d.c. bias path. Fortunately, the RF circuit design called for inductive output coupling, a gate coil, and source lead inductance. Through proper design of these components, an adequate thermal block could be achieved.

The thermal resistance of a wire is given by

$$R_{TH} = L/kA \qquad (3.2.2.1)$$

where L is the wire length, A is the wire cross-sectional area, and k is the material thermal conductivity. Equation 3.2.2.1 shows that like electrical resistance, thermal resistance increases with length and with smaller cross-sectional area. By plating a poor thermal conductor with a thin layer of a good RF conductor, a low loss component with a high thermal resistance can be obtained.

Manganin is a copper based compound originally developed for its property of constant resistance with temperature. Its electrical and thermal conductances are each about twenty times poorer than that of copper (ie. $k_{manganin} \cong 18.7 W/K/m$, $k_{Cu} \cong 420 W/K/m$) [46]. This makes it a suitable material, when plated with a good RF conductor, for use as a thermal blocking inductor.

The formula for the inductance of a straight wire is [47],

$$L(nH) = 2x10^{-4}\left[\ln(4L/d) + 0.5d/L - 0.75\right] \qquad (3.2.2.2)$$

where L is the wire length and d is the diameter. The required source inductance for the HEMT is 3.5nH. However, the source lead is normally twinned. Therefore an inductance of 7.0nH is required in each path. The HEMT drain has two inductive connections: L10 (4.4nH) provides the bias path and L14 (5.5nH) couples to the second stage. A gold plating thickness of 2.5μm was chosen as a compromise between maintaining a low loss RF path and keeping the thermal resistance reasonably high. The thinnest manganin wire available that is practical to work with is 0.06mm in diameter.

The gate bias inductance, L2, is too large to be realized practically with simply a straight wire. It was designed using the formula for the inductance of an air filled RF coil [48], which is

$$L = \frac{a^2n^2}{9a + 10b}, \qquad (3.2.2.3)$$

where a is the coil radius in inches, b is the coil length in inches, and n is the number of turns. Using Equation 3.2.2.3, the coil was determined to require 5 turns having a radius of 1.5mm spaced along a length of 5.3mm. The total length of the wire required is approximately 47mm ($2\pi an$).

Table 3.2.2.1 gives the required lengths of the gate, drain, and source inductors for 0.06mm diameter manganin. The corresponding thermal resistances including the effect of the gold plating (k_{Au}=320W/K/m) are also given. In the case of L2, L10, and L14, the thermal resistances to the 300K enclosure are actually larger than the values given as they are not connected directly to ground.

Component	Inductance (nH)	Length (mm)	Thermal Resistance (K/mW)
L3	7.0	6.6	51.6
L10	4.4	4.5	35.2
L14	5.5	5.3	41.4
L2	25	47	362

Table 3.2.2.1: Gate,Source, and Drain Inductor Lengths and Associated Thermal Resistances.

The total conductive thermal resistance is determined by combining the thermal resistances of the four inductors in parallel and is found to be 13.4K/mW. This results in a conductive heat load of about 7.5mW assuming a temperature difference of 100K.

3.2.3 Convection Heat Load

Conductive heat transfer in a fluid is caused by the transfer of mechanical energy through molecular collisions. As molecules increase in energy, their temperature rises. In an ideal gas this results in pressure gradients which produce fluid flow patterns. In this manner heat is transferred convectively from bodies at different temperatures, flowing from the warmer body to the colder one.

The average distance travelled by a molecule before it collides with another is called the *mean free path* and is given by [49],

$$\lambda = 2.33\times10^{-20}T/(\xi^2 P) \quad \text{(cm)}, \qquad (3.2.3.1)$$

where T is in Kelvin, P is pressure in Torr, and ξ is the molecular diameter in cm. For air at ambient temperature, equation 3.2.3.1 reduces to [49],

$$\lambda = 5\times10^{-3}/P\text{(cm)}. \qquad (3.2.3.2)$$

If the mean free path is much larger than the enclosure size, collisions occur only between molecules and the enclosure walls. In this instance convective heat transfer does not exist since energy is not exchanged between molecules and hence flow patterns are not produced. Therefore, convective heat transfer can be eliminated by operating at a pressure such that the enlosure dimensions are much less than the mean free path. Table 3.2.3.1 gives the mean free path (λ) for air at various pressures.

Pressure (Torr)	λ (cm)
760	6.6×10^{-6}
1.0	0.0050
0.10	0.050
10^{-2}	0.50
10^{-3}	5.0
10^{-4}	50
10^{-5}	500

Table 3.2.3.1: Mean Free Path of Air for Various Pressures

An experiment was carried out to verify both the performance of the Peltier device and the variation of the heat load with pressure, as reflected by the temperature difference. The Peltier device was mounted in a bell jar vacuum enclosure as shown in figure 3.2.3.1 with thermocouples on both its hot and cold surfaces. The thermocouples were of sufficient length to render their heat load contribution negligible. The mechanical roughing pump is capable of achieving pressures down to about 10^{-3}Torr, below which the diffusion pump must be used (down to ≈ 10^{-6}Torr). Measurements were carried out with a Peltier current (I_p) of 3.8A, the current specified for maximum cooling power for that particular device. The hot plate temperature varied from about 33°C to 36°C during the measurements.

Figure 3.2.3.2 gives the resulting plot of temperature difference versus pressure. Below a pressure of about 10^{-3} Torr, the temperature difference of about 130K is very close to that specified by the manufacturer for zero heat load (combined radiative and conductive heat load is less than 10mW). It is evident that the temperature difference begins to drop off at a pressure of about 10^{-3} Torr. This is due to the mean free path length approaching the dimensions of the enclosure, resulting in an increased convective heat load. The fact that the drop off occurs at a pressure higher than 10^{-3}Torr is very useful as it allows for the use of mechanical pumping and thus much simpler vacuum technology. The LNA enclosure will certainly be smaller than the bell jar, further reducing the heat load for a given pressure.

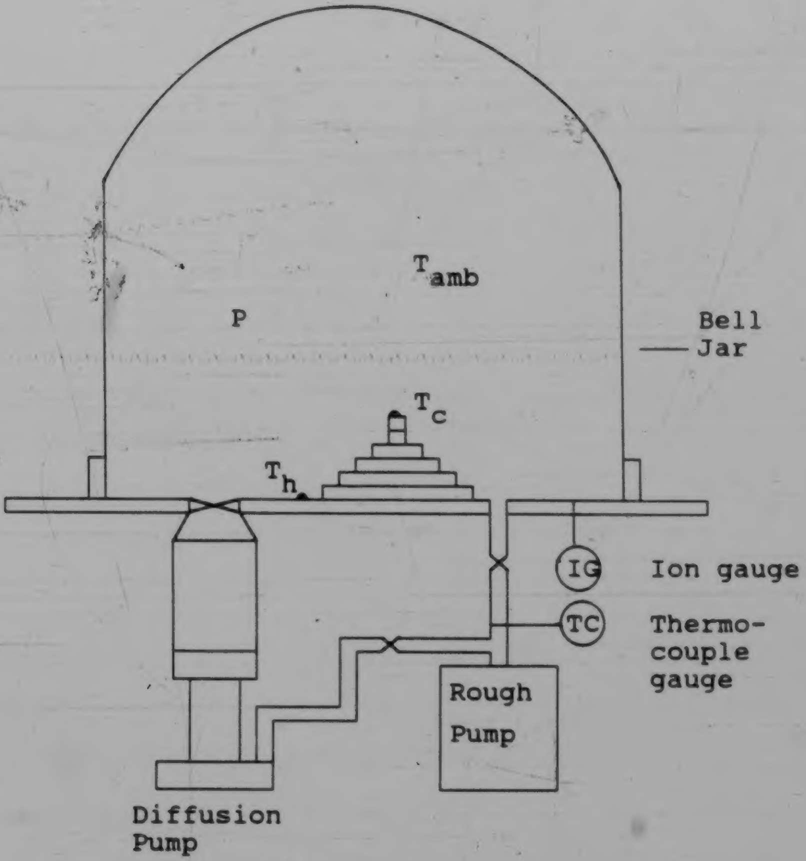
T_{amb}
P
Bell Jar
T_c
T_h
IG
Ion gauge
TC
Thermo-couple gauge
Rough Pump
Diffusion Pump

Figure 3.2.3.1: Peltier Device Test in Bell Jar.

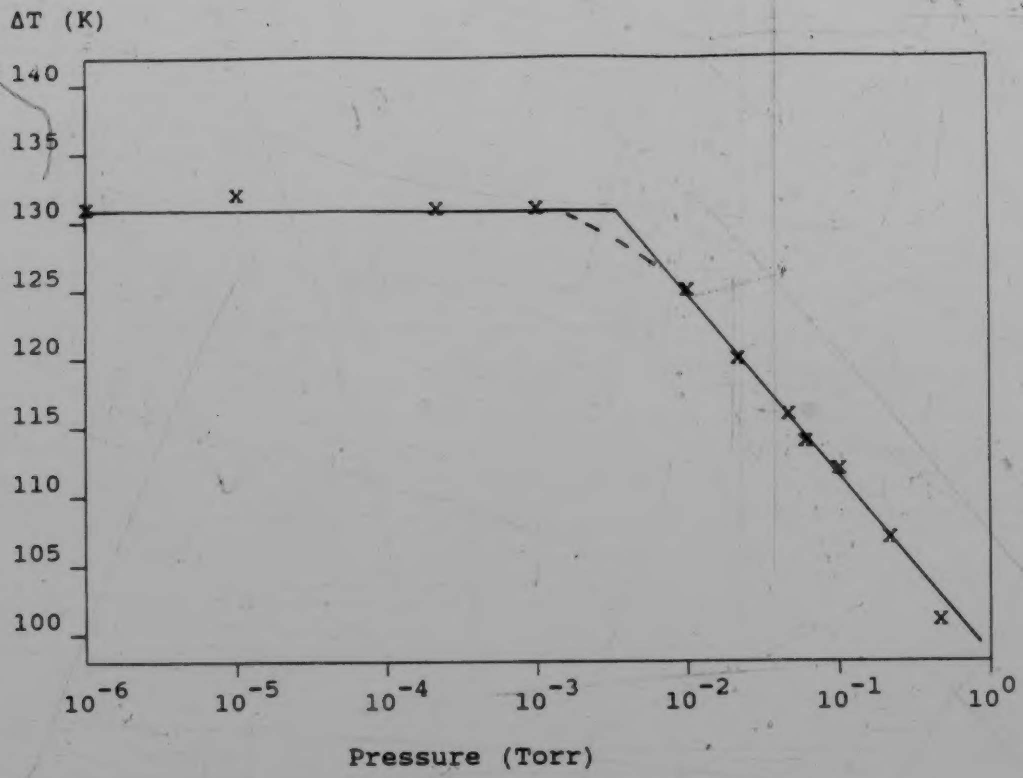

Figure 3.2.3.2: Peltier Device Temperature Differential versus Pressure.

In the thermal design of the LNA enclosure, the convective heat load on the refrigerator can be neglected if a maximum pressure of 10^{-3}Torr can be maintained. Actually, the maximum required pressure is probably an order of magnitude higher (10^{-2}Torr) because the LNA enclosure will have dimensions at least ten times smaller than the bell jar in which the experiment was carried out. In producing a practical LNA, the problem lies not in the ultimate pressure which can be achieved, but in being able to maintain that pressure for periods of several months or years despite leakage of seals and outgassing of materials. Operating the refrigerator under a vacuum is also essential for preventing water vapour from freezing on the Peltier device or HEMT carrier and severely degrading performance.

3.2.4 Radiation Heat Load

Any body having a non-zero physical temperature emits thermal radiation in all possible directions. The expression for radiative heat transfer between two arbitrary surfaces in a two zone enclosure is [37]

$$Q_{1-2} = \frac{\sigma T_1^4 - \sigma T_2^4}{\dfrac{(1-\varepsilon_1)}{A_1\varepsilon_1} + \dfrac{1}{A_1 F_{1-2}} + \dfrac{(1-\varepsilon_2)}{A_2\varepsilon_2}} \qquad (3.2.4.1)$$

where σ is the Stefan-Boltzmann constant ($5.667\text{x}10^{-8} W/m^2/K^4$), ε_1 and ε_2 and A_1 and A_2 are the emissivities and surface areas of the respective surfaces, and F_{1-2} is the geometric view factor between the two surfaces.

In the LNA enclosure the HEMT carrier, along with part of the input capacitor, can be thought of as a small body with emissivity ε_1, surface area A_1, and temperature T_1 completely surrounded by a surface with emissivity ε_2, surface area A_2, and temperature T_2 as shown in figure

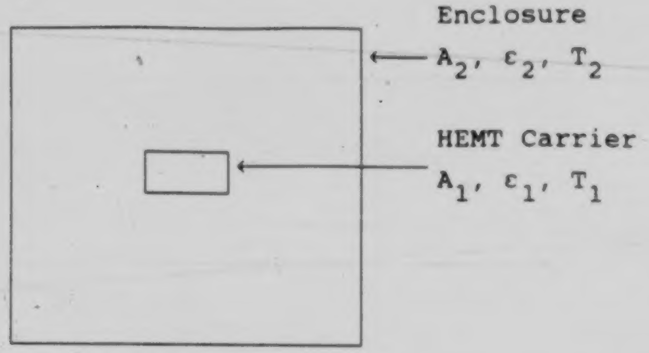

Figure 3.2.4.1: HEMT Carrier Surrounded by LNA Enclosure

3.2.4.1. Since any radiation emitted by surface A_1 would reach surface A_2, the geometric view factor, F_{1-2}, is simply unity. Area A_1 is actually the composite of the quartz HEMT carrier and the cold terminal of the capacitor. Therefore, using superposition, equation 3.5.1 can be rewritten as

$$Q_{2-1} = \frac{\sigma T_2^4 - \sigma T_1^4}{\dfrac{(1-\varepsilon_Q)}{A_Q \varepsilon_Q} + \dfrac{1}{A_Q} + \dfrac{(1-\varepsilon_2)}{A_2 \varepsilon_2}} + \frac{\sigma T_2^4 - \sigma T_1^4}{\dfrac{(1-\varepsilon_C)}{A_C \varepsilon_C} + \dfrac{1}{A_C} + \dfrac{(1-\varepsilon_2)}{A_2 \varepsilon_2}} \tag{3.2.4.2}$$

where A_Q, ε_Q, A_C, and ε_C are the surface areas and emissivities of the quartz and the cold terminal of the capacitor respectively. The capacitor terminals are made of gold plated copper. The emissivities of quartz (glass) and gold (polished) are about 0.9 and 0.02 respectively [37]. The surface areas of the HEMT carrier and the cold capacitor terminal are $58.2\times10^{-6}m^2$ (5.2mmx5.2mmx1.5mm) and $154\times10^{-6}m^2$ (≈7mmx7mmx2mm) respectively. The surface area of the enclosure (also polished gold) will be approximately $3.6\times10^{-3}m^2$ (≈3cmx3cmx1.5cm). Substituting these values with T_1=200K and T_2=300K into equation 3.2.4.2 yields a radiative heat load of 12.4mW (R_{RAD}=8.1K/mW). This is a conservative estimate since a significant portion of the quartz is covered with gold, thus reducing the radiative heat load.

3.2.5 Total Heat Load

The preceding sections resulted in the determination of the individual heat loads due to conduction, convection, and radiation. It is now possible to calculate the total heat load on the Peltier device and to make an estimate of the temperature achievable on the refrigerator cold plate.

The total heat load is simply the sum of the conductive and radiative heat loads since the convective heat load, in the evacuated enclosure, will be negligible. The total heat load for a 200K cold plate comes out to be 19.9mW. The total thermal resistance, R_T, assuming a ΔT of 100K, is 5025K/W. Substituting this value into equation 3.2.5 yields a HEMT temperature, T_{HEMT}, of 186K. The actual HEMT temperature should be somewhere between 186K and 200K since the three heat loads will increase with the larger temperature differential.

✓

3.3 LNA Enclosure Design

Several factors must be taken into account in the design of the LNA enclosure. It must contain a chamber, amenable to evacuation, to house the Peltier refrigerator and associated first stage circuitry. This entails the need for RF and DC feedthrus to provide RF coupling, biasing, and the refrigerator DC power. The enclosure should also provide a means for tuning the LNA, preferably with the first stage under vacuum This avoids an iterative tuning process involving temperature cycling of the refrigerator. The enclosure must also contain the second and third stage circuitry as well as the bias supplies for the HEMTs.

A compartmentalized enclosure, shown in figure 3.3.1, was developed to meet the above needs. The enclosure was machined out of a single block of oxygen free, high conductivity (OFHC) copper and gold plated to maintain the surface finish and a low emissivity in the refrigerator compartment. The input tuning circuit is located outside the vacuum chamber to allow for tuning while the first stage HEMT is cooled. There is also a separate chamber for the biasing circuitry and for the second and third stages.

Hermetic RF feedthrus are used to couple the RF signal in and out of the vacuum chamber. The DC biasing for the first stage and the refrigerator power supply are brought into the vacuum chamber with a vacuum feedthru having four molybdenum conductors, capable of carrying 10 amps each (the

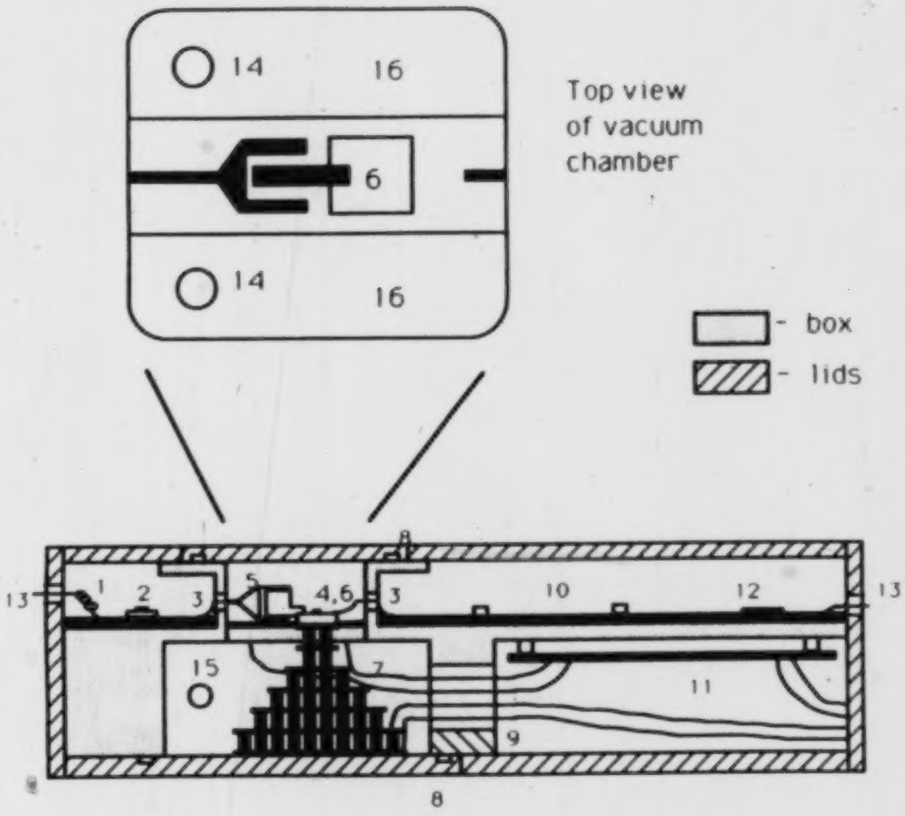
14
16
6
14
16
Top view
of vacuum
chamber
- box
- lids
13
1
2
3
5
4,6
3
8
10
12
13
15
7
11
9
8

1 Input circuit
2 Input Tuning Capacitor
3 Hermetic feedthru (50 ohms)
4 First stage HEMT (chip)
5 Air Capacitor
6 Quartz HEMT Carrier
7 6 Stage Peltier device
8 Indium Gasket
9 Hermetic feedthru
10 Stages 2 and 3
11 D C bias circuitry
12 6 dB attenuator
13 50 Ohm SMA Connectors
14 Fil-con
15 Pipe to vacuum
16 First stage circuitry on copper plates

Figure 3.3.1: Cross-Section of L-Band LNA Enclosure

Peltier device requires up to 4 amps). Both feedthrus were soft soldered in place, along with the pipe for the vacuum pump, before the gold plating was attempted.

The Peltier device is constructed with solder having a 138°C melting point. For this reason great care had to be taken in mounting it so as not to damage the device. Both the hot side of the Peltier device and the bottom lid of the vacuum chamber had to be pre-tinned with indium based solder (~117°C melting point) using an acid based flux. The Peltier device was then positioned on the lid with a template, and placed on a hot plate at 125°C to reflow the solder. A resin based flux was used in this step. When the solder reflowed, downward pressure was placed on the Peltier device before it was quickly removed from the hot plate and allowed to cool.

Caution also had to be taken in mounting the HEMT carrier assembly on the Peltier device cold plate. The chip HEMT and the bonding leads are both easily susceptible to damage. A thermally conductive epoxy was used for this procedure. It requires a 24 hour curing period. A jig was built that mounts on top of the enclosure. A nylon screw through the jig applied pressure to the HEMT carrier throughout the curing period.

The leads to the Peltier device are fragile and susceptible to breaking under repeated strain. Strain relief terminal posts were constructed and mounted on the lid containing the refrigerator. The leads were soldered to the posts, thus eliminating excessive stress on them.

The seals for the vacuum chamber were formed with indium wire placed in the grooves of the lids before fastening. These successfully held a vacuum and were able to be re-used several times.

3.4 Conclusions

This chapter provided an introduction to thermoelectricity and the limitations of practical thermoelectric devices. A thermal model for the first stage of the LNA was established which included the three main sources of heat conduction. With this model in mind, the RF design was integrated with the thermal requirements in a unique manner which involved the development of a compartmentalized vacuum enclosure and a technique for producing quartz HEMT carriers.

Chapter 4: Results

4.0 Introduction

In this chapter a brief introduction will be given on the topic of noise measurement. In particular, the methods used in testing the LNA design will be discussed, such as the noise and S-parameter measurement systems. Subsequently, the actual results of experiments with the modified 'Walker' LNA [15], and the LNA developed in the preceding chapters will be given. It will be shown that several modifications to the design were necessary due to model deficiencies which resulted in severe stability problems and higher than expected noise temperatures. Compromises to the thermal design were required to ensure stable operation of the LNA.

4.1 Noise Measurement Method

Typically, the noise temperature of a DUT (device under test) is measured using the so called hot/cold technique. This technique requires that two known noise sources, a 'hot' (T_h) and a 'cold' (T_c) source, are applied to the input of the DUT. The output power of the DUT is measured for each source (N_h and N_c). Plotting these two points on an x-y graph as shown in figure 4.1.1, with the y-axis being output power and the x-axis being source noise temperature, enables a straight line to be drawn through them. The y-intercept is the noise power contribution of the DUT alone

(N_a). The x-intercept is equal to $-T_e$, where T_e is the effective input noise temperature of the DUT [50]. The available gain (G_A) of the DUT is the ratio of the slope of the line to the slope of the line with the DUT replaced by a lossless connection (ie. calibration).

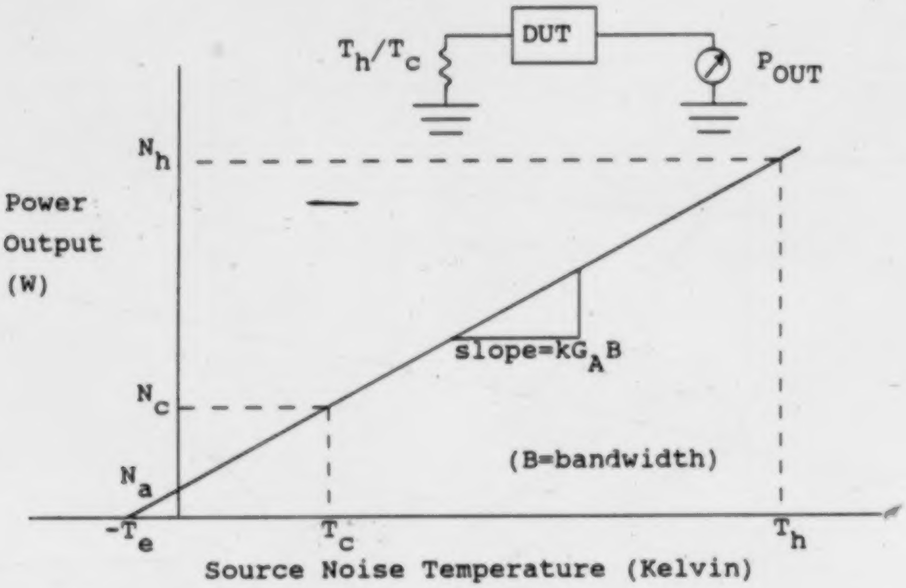
DUT
T_h/T_c
P_{OUT}
N_h
Power Output (W)
slope=kG_AB
N_c
(B=bandwidth)
N_a
$-T_e$
T_c
T_h
Source Noise Temperature (Kelvin)

Figure 4.1.1: Noise temperature measurement using the hot/cold source technique.

The HP8970A Noise Figure Meter, in conjunction with an HP346 calibrated noise source, automatically performs the above measurements for T_e and G_A. The HP8970A has the capability of measuring the noise figure of a DUT from 10MHz to 1500MHZ. Any measurements outside this frequency band require external mixing to bring the signal within the measurement range of the HP8970A. A typical configuration for noise measurements with the HP8970A in the frequency range of 10-1500MHz is given in figure 4.1.2..

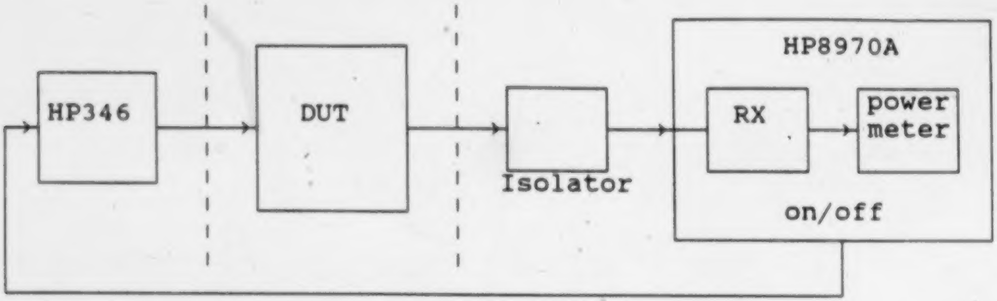

Figure 4.1.2: Typical noise measurement configuration.

The dotted lines in figure 4.1.2 represent locations where the signal path is broken to calibrate the system before the DUT is inserted. The HP346 noise source has a nominal output impedance of 50 ohms. In general, the output impedance of the DUT is not 50 ohms. The isolator ensures that the receiver inside the noise figure meter sees the same source impedance during calibration and measurement, hence keeping its noise contribution constant. In some situations it is also required to have a directional coupler between the DUT and the HP8970A to monitor for DUT oscillations.

4.2 S-Parameter Test-Set

The network analyzer, or S-parameter test-set, is the instrument used to characterize, or determine the S-parameters, of microwave networks. The radioastronomy laboratory at the University of Alberta has access to such an instrument which can be operated in either manual mode or automatic mode. The full description of the instrument's operation and calibration techniques are given by Chau [51] and Valk [52]. Figure 4.2.1 is a block diagram of the S-parameter test set. For the purpose of the measurements required in this project, the test-set described provides more than adequate accuracy and repeatability.

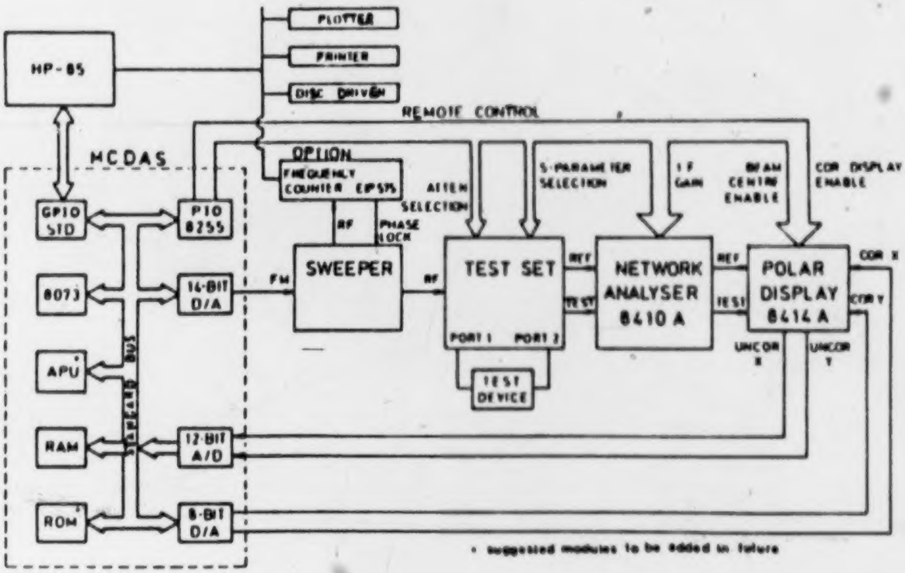
HP-85
PLOTTER
PRINTER
DISC DRIVER
REMOTE CONTROL
MCDAS
OPTION
FREQUENCY COUNTER EIP575
GPIO STD
PIO 8255
8073
14-BIT D/A
APU*
STANDARD BUS
RAM
12-BIT A/D
ROM*
8-BIT D/A
RF
PHASE LOCK
FM
SWEEPER
RF
ATTEN SELECTION
S-PARAMETER SELECTION
TEST SET
PORT 1
PORT 2
TEST DEVICE
REF
TEST
NETWORK ANALYSER 8410 A
I F GAIN
BEAM CENTRE ENABLE
REF
TEST
POLAR DISPLAY 8414 A
COR DISPLAY ENABLE
COR X
COR Y
UNCOR X
UNCOR Y

* suggested modules to be added in future

Figure 4.2.1: S-Parameter measurement system.
Modified from Chau [51].

4.3 Modified L-Band LNA

In order to verify the manufacturer's data on the performance of the NEC320 series HEMTs, a three stage L-band LNA, almost identical to the ones employed in the DRAO synthesis telescope [15], was constructed with an NE32084 HEMT in the first stage. The noise and gain measurements were carried out using the configuration given in figure 4.3.1. An isolator was not required at the LNA output since it has a 50 ohm output impedance, the same as that of the noise source.

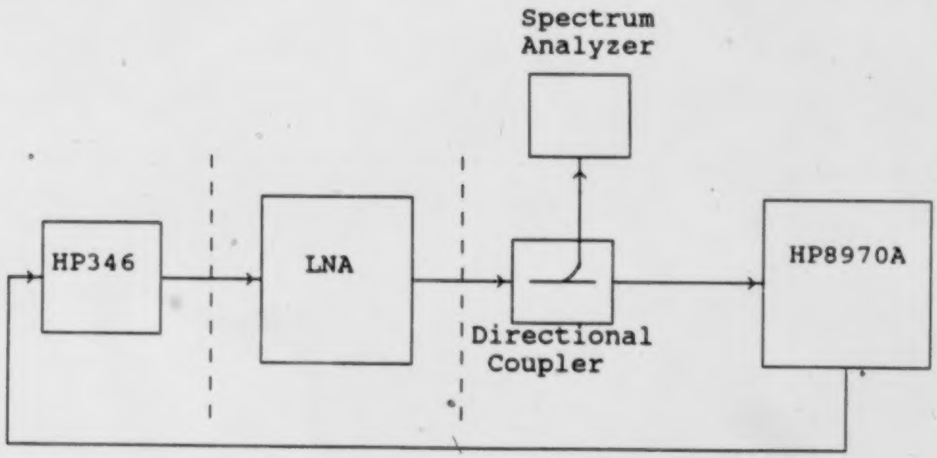

Figure 4.3.1: LNA noise and gain measurement configuration.

Oscillation problems were encountered with the LNA. In order to stabilize the amplifier it was necessary to place strips of lossy material (Eccosorb) along the sides of the enclosure. Grounding the first stage HEMT carrier to the lid also helped ensure stability.

After the LNA operated satisfactorily at room

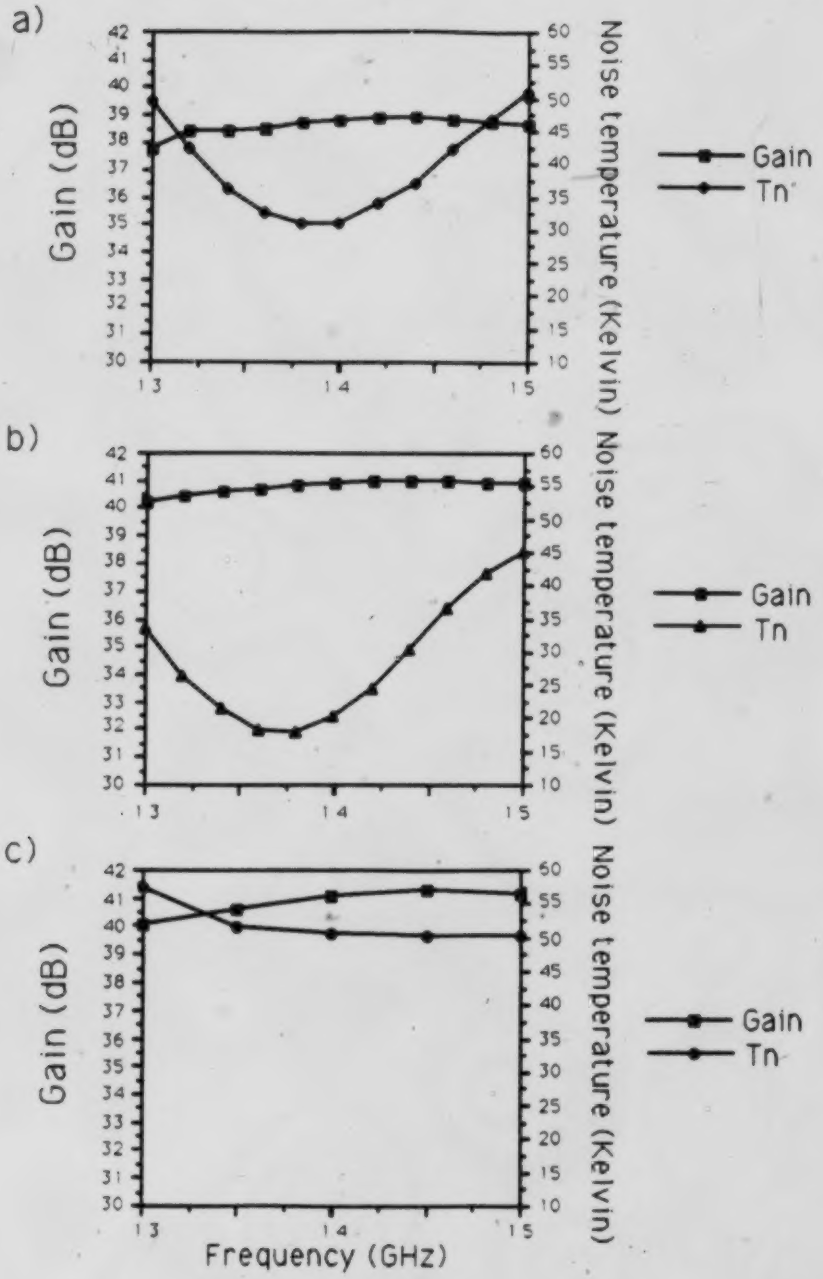

Figure 4.3.2: Measured gain and noise temperature of DRAO L-band LNA. a) 300K NE32084 HEMT in first stage. b) 217K NE32084 HEMT in first stage. c) 300K MFG1412 GaAsFETs in all three stages.

temperature, it was placed in a styrofoam box filled with dry ice (≅ -56°C). Figure 4.3.2 gives the noise temperature and gain for the LNA at both room temperature and at -56°C. The gain and noise temperature for a typical LNA employing MFG1412 GaAsFETs in all three stages is also given for comparison purposes.

Figure 4.3.2 shows that the LNA with the room temperature HEMT has a noise temperature at mid-band lower by about 20K than the typical GaAsFET LNA. The mid-band input reflection coefficient was also less than -10dB, indicating a reasonable input match. With moderate cooling, the noise temperature of the HEMT LNA was reduced by another 10 degrees. The large S_{11} of the HEMT is reflected by the narrow bandwidth of the noise temperature curve. The small source inductance (0.1-0.3nH) in these LNAs does not reduce the reactance of the HEMT input impedance enough to make a simultaneous broadband noise and power match possible.

4.4 LNA With Peltier Cooled First Stage HEMT

Due to the inherently unstable nature of HEMTs, stability problems were anticipated in the testing of the LNA. For this reason, and in order to simplify troubleshooting, the second and third stages of the LNA were tested independently from the first. Stability problems were even more extreme than anticipated. Also, some of the assumptions made in the initial design were found to be incorrect. These two factors required the need for modifications and compromises to the original LNA design.

4.4.1 Second and Third Stage Testing

The second and third stages of the LNA were constructed on Rogers Duroid® microwave circuit board (ε_r=2.33, 0.030" dielectric thickness) with the component values determined in section 2.5. The circuit board layout is given in figure 4.4.1.1 and the schematic in figure 4.4.1.2. A brass box was used for the circuit enclosure.

Chip capacitors and resistors were used in the circuit construction. Inductors were formed according to equation 3.2.2.3 except for the source inductances, L10 and L14, which were formed out of the HEMT source leads themselves, and L15, which was realized with a microstrip inductor. The HEMT source leads were considered to be lengths of microstrip in the design of L10 and L14. The inductance of a straight length of microstrip is given by [47]:

$$L = L_o K_g, \tag{4.4.1.1}$$

where K_g is the ground plane correction:

$$K_g = 0.57 - 0.145 \ln(w/h), \tag{4.4.1.2}$$

for $w/h > 0.05$ and L_o is:

$$L_o = 2\text{x}10^{-4}\left[\ln\left(\frac{l}{w+t}\right) + 1.193 + 0.2235\left(\frac{w+t}{l}\right)\right], \tag{4.4.1.3}$$

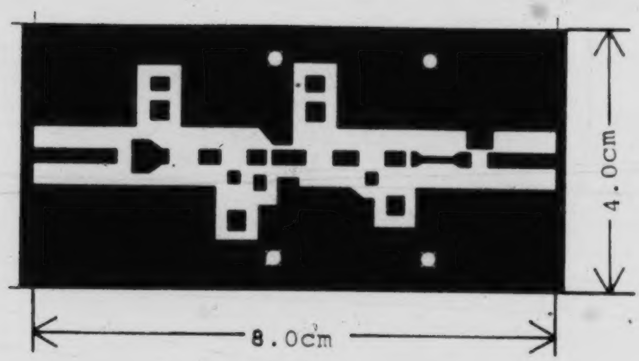

Figure 4.4.1.1: Printed circuit layout of second and third LNA stages.

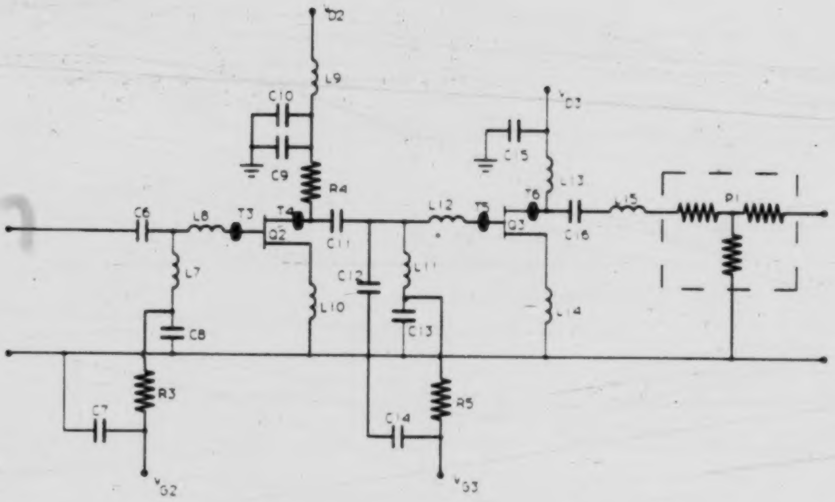
V_D2
L9
C10
C9
R4
V_D3
C15
L13
C6
L8
T3
T4
Q2
C11
L12
T5
T6
Q3
C16
L15
P1
L7
C12
L11
L10
C13
L14
C8
R3
C7
C14
R5
V_G2
V_G3

Q2, Q3-NE32084

C7, C14, C15-680pF
C8, C10, C13-22pF
C6, C9, C11-0.5pF
C12, C16-1.0pF

L7, L9, L11-25nH
L8-12nH
L10, L14-1.0nH
L12-23.5nH
L13-12.4nH
L15-1.7nH

R3, R5-1000Ω
R4-100Ω

P1-6dB pad

T3 - T6-Ferromagnetic Toroid

Figure 4.4.1.2: Schematic of second and third LNA stages.

where L_o is in nH, 'w' is the conductor width (mm), 't' is the conductor thickness (mm), 'l' is the conductor length (mm) and 'h' is the dielectric thickness (mm).

Initial tests of these two stages indicated that they both were unstable. When operating independently, stage 2 oscillated at about 6.3 GHz, and stage 3 at 4.25, 6.6, and 6.8 GHz. It must be noted that these oscillations were of a dynamic nature and very sensitive to variations in circuit parameters and bias conditions.

The first step taken to overcome this problem was to ensure adequate grounding of the circuit board. Numerous via holes were drilled in the board through which copper wires were soldered connecting ground on the upper surface to the lower ground plane. Copper tape was wrapped around the edges of the board and soldered to ground on both sides. Also, the circuit board was fastened tightly to the brass enclosure. After these steps were taken, the HEMTs continued to oscillate at multiple frequencies. This indicated with reasonable certainty, that poor grounding was not the sole cause of the instability.

It was found that loading the bias coils with lossy material quelled the oscillations at all but ~6.3 GHz in the second stage. That was an indication that the coils couple and extrinsically increase the feedback, or S_{12}, of the HEMTs. Reducing the source lead inductance of the second stage to a few tenths of a nanohenry killed the remaining oscillation mode.

Although loading the bias coils effectively increased the stability of the circuit, it also drastically changed the characteristics of the inductors. An alternative measure in reducing the effects of the coupling coils was then attempted. Shielding made from brass shim stock was placed between the amplifier stages. In addition, walls were constructed around the individual bias networks. In this manner the two stages were stabilized, allowing for further testing of the important circuit parameters, noise temperature and gain.

In order to determine the performance of the two stages over a relatively large bandwidth, the test configuration was set for 1.0 to 2.0GHz operation as shown in figure 4.4.1.3. The external local oscillator at 2.4 GHz, in conjunction with a mixer, was used to bring the signal into the range of 400-1400 MHz, making it compatible with the noise figure meter. An L-band LNA was used to reduce the noise contribution of the mixer and thus maintain the system noise temperature at a reasonable level. The low-pass filter prevents higher frequency components from mixing down into the range of the noise figure meter.

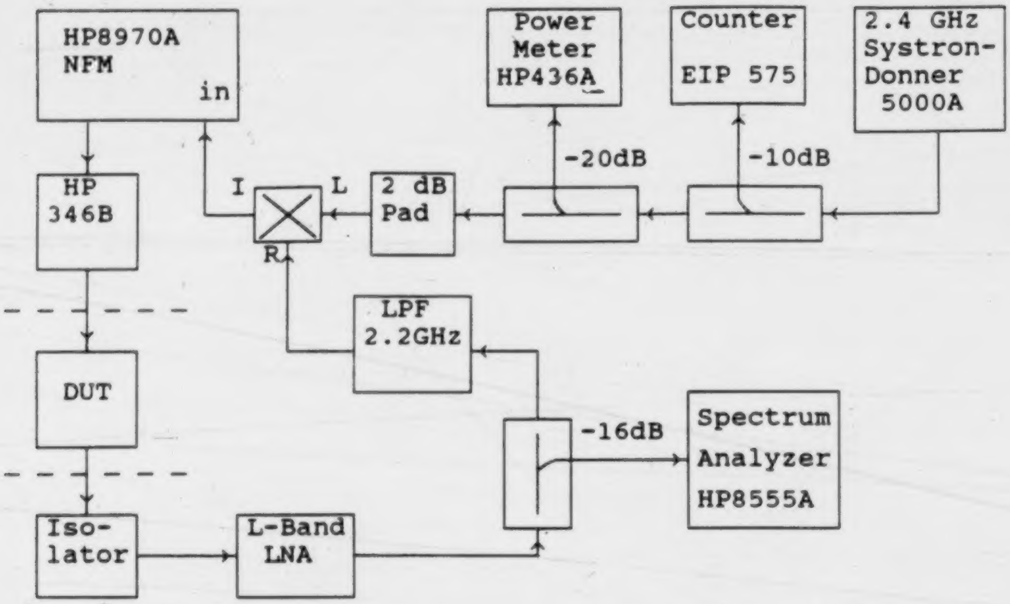
HP8970A
NFM
in
Power
Meter
HP436A
Counter
EIP 575
2.4 GHz
Systron-
Donner
5000A
-20dB
-10dB
HP
346B
I
L
2 dB
Pad
R
LPF
2.2GHz
DUT
-16dB
Spectrum
Analyzer
HP8555A
Iso-
lator
L-Band
LNA

Figure 4.4.1.3: Stages 2 and 3 test configuration.

The results of the gain and noise temperature measurements are given in figure 4.4.1.4 along with the results predicted by Touchstone® for the two stages. It can be seen that the actual noise temperature is not as low as predicted. Rather than continuing with the refinement of these two stages it was decided to proceed with the development of the first stage for the following reasons: (1) the first stage is where new concepts will be tested; (2) the overall LNA performance is dominated by the first stage performance; (3) any useful bandshaping or input matching modifications can only be accomplished with knowledge of the first stage characteristics.

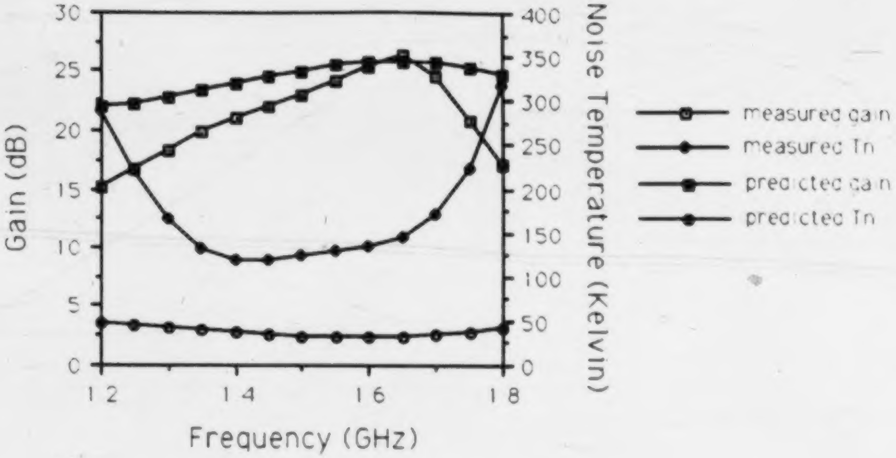

Figure 4.4.1.4: Measured and predicted gain and noise temperature of second and third LNA stages (without 6dB attenuator).

4.4.2 First Stage Testing

The first stage performance is what ultimately determines the sensitivity of the amplifier. In this stage new concepts have been developed which form the motivation for this thesis. Hence, the main focus of experimental work has been in attempting to achieve successful operation of this cooled first stage.

The refrigerator and HEMT carrier were assembled as outlined in chapter 3. The drain and gate bias networks were constructed on separate copper plates as shown in figure 3.3.1. and were each fastened down with a screw and a Fil-con feedthru. The input tuning network, which consists of L1 and C_{T1}, was built on the same type of circuit board as the second and third stages. Its layout is given in figure 4.4.2.1. A 50 ohm thru-line was inserted in place of the second and third stages. Initial tests were carried out at room temperature to ensure proper RF operation before cooling was attempted.

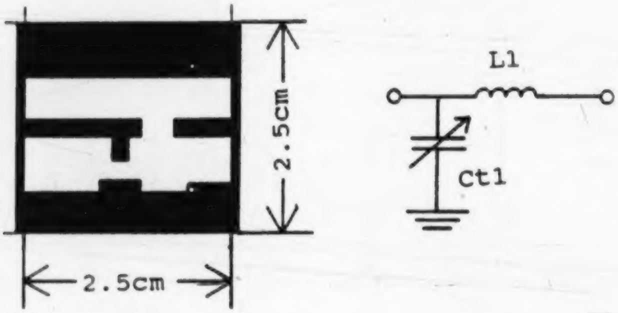

Figure 4.4.2.1: Printed circuit layout of input tuning circuit and associated components.

During the construction of the first stage, a slight transverse force was exerted on the HEMT carrier. Due to the rigidity of the epoxy joining it to the refrigerator, the top stage of the Peltier device fractured. Fortunately a spare refrigerator was available which could be used to rebuild the stage. A thermal grease was chosen for attaching the HEMT carrier to the cold plate for the remainder of the room temperature tests. The grease facilitated easy removal of the HEMT carrier, a procedure accurately predicted to be required quite frequently during the development stages of the project.

When the HEMT was turned on oscillations were found to be present at 4.8 GHz. This oscillation mode was eliminated by clamping down the source inductances more tightly using washers and the screws for fastening the bias plates. The HEMT then began to oscillate at several frequencies between 8 and 14 GHz (and possibly higher). At this point, strange bias behavior of the HEMT led the author to believe it was damaged. HEMT damage was confirmed with the discovery of a very small gate to drain resistance.

The exact cause of the HEMT damage was unknown. However, in order to remove the substantial possibility of HEMT damage during the bonding procedure, it was decided to continue the testing using an NE32084 packaged HEMT in the first stage. The dimensions of the packaged HEMT were such that it was possible to solder it directly to the carrier developed for the chip HEMT. For ease of removal during room temperature testing, the carrier was again mounted on the Peltier device using thermal grease.

At this point the HEMT appeared to be marginally stable. With the drain current below about 10mA, gain increases in bands approximately 60MHz wide were detected at 9.7 and 12.7 GHz. As the bias current was increased above 10mA, the ripples became sharp peaks, definitely indicating oscillations. Below 10mA it could not be ascertained whether the spectral features were simply circuit resonances or in fact frequency modulated oscillations. The author decided to proceed with noise temperature measurements while operating the marginally stable HEMT at a drain current of 10mA in the hopes of gaining insight into the circuit performance.

The initial results using the test configuration given in figure 4.4.1.3 showed that the bandshape was severely skewed. Reducing the input inductance, L1, to the point where it was simply a thruline and replacing the tuning capacitor, CT1, with one having a range of 0.5-10pF shifted the passband such that it was centered on 1420MHz. Subsequent adjustment of L2 and L3 resulted in the stage having 9.5dB gain and 170K noise temperature at 1420MHz. This noise temperature was much higher than that predicted by Touchstone®.

In order to determine if the HEMT actually was presented with a source reflection coefficient equal to Γ_{opt}, an external three stub tuner was placed in series with its input as shown in figure 4.4.2.2 The 3dB attenuator serves to present the circuit with a reasonable out-of-band reflection coefficient to prevent oscillations. If the LNA is internally tuned to present the HEMT with Γ_{opt}, then adjusting the tuner for minimum noise should result in a value of Γ_s' equal to zero. After tuning for minimum noise at 1420MHz, Γ_s' was measured on the S-parameter test set in manual mode. The measured magnitude of Γ_s' was approximately 0.05, indicating that the internal tuning provided the HEMT with a source reflection coefficient very close to Γ_{opt}. This result indicated that the poor noise performance was due to something other than inadequate input matching of the HEMT.

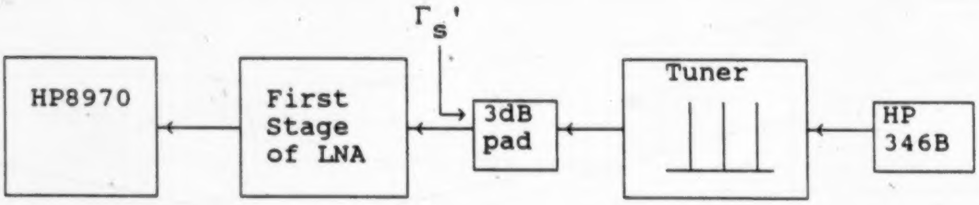

Figure 4.4.2.2: Test to determine if first stage HEMT is tuned to Γ_{opt}.

Out-of-band oscillations are known to degrade in-band noise performance due to the mixing action of the transistor operating in a non-linear mode. For this reason and because of the obvious marginal stability of the HEMT, the author presumed that the apparent high frequency gain peaks were in fact frequency modulated oscillations which caused the poor noise performance. This was confirmed when slight variations of the source inductance resulted in oscillations at lower bias currents than before (≅5mA).

Weinreb et al [14] found it necessary to bypass the source inductance at high frequencies with series RC networks to increase out-of-band stability. However, as stated in section 3.2.1, source capacitance in the NEC HEMT is detrimental to stability. Nevertheless, experiments employing RC source bypass networks were performed to test Touchstone® predictions which relied on the manufacturer's transistor data.

Figure 4.4.2.3 gives the magnitude and phase plots for the impedance of various RC combinations in parallel with

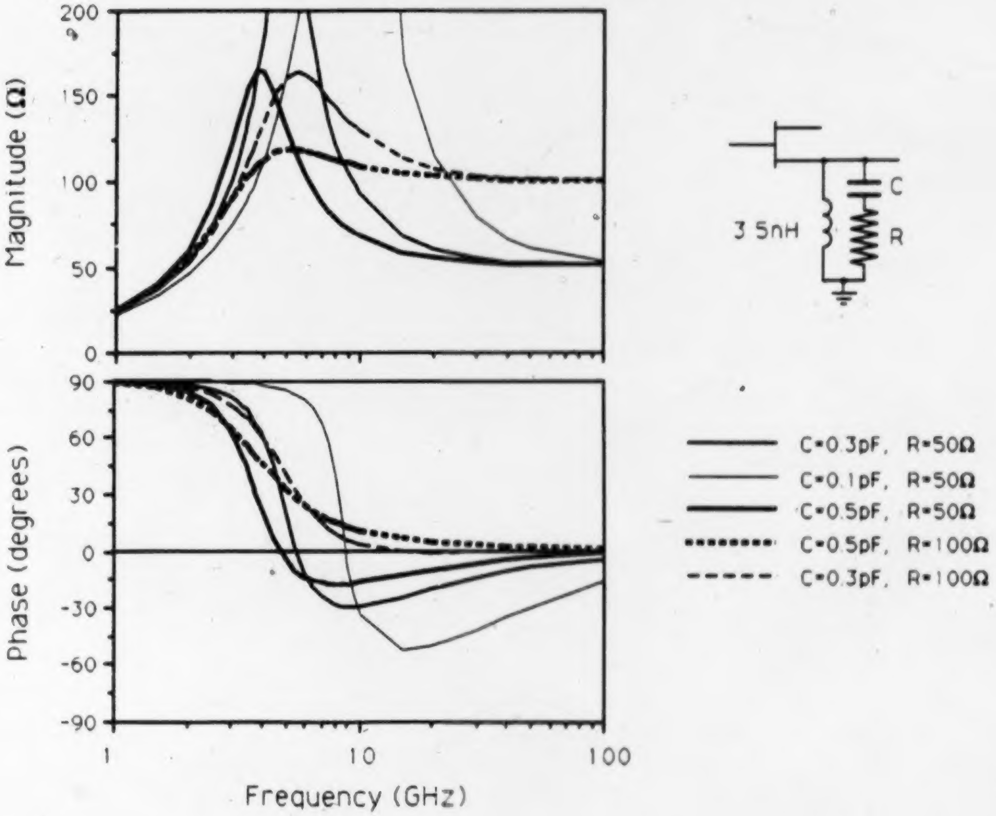

Figure 4.4.2.3: Impedance of source inductance in parallel with various RC bypass networks.

the source inductance, L3. Microwave stripline resistor packages formed the resistances. The capacitances were formed by sandwiching a thin piece of teflon between ground and one lead of the resistor package.

The first RC combination tested consisted of a 0.5pF capacitor and a 50Ω resistor. With these in place the HEMT oscillated at 4.5GHz as well as at higher frequencies. The 4.5GHz oscillation frequency corresponds very closely to the resonant frequency of the RC/L3 combination. Figure 4.4.2.3 shows that the phase of this combination goes negative at the resonant frequency, indicating a capacitive impedance. The negative phase in conjunction with the large resonant impedance creates large feedback voltages which cause the instability.

The impedance of a 0.5pF capacitor and a 100Ω resistor in parallel with L3 never has a negative phase angle as shown in figure 4.4.2.3 This indicates that the combination is never capacitive. When placed in the circuit oscillations persisted at 10.2 and 13.2GHz, roughly the original oscillation frequencies. This combination may not have worked in quelling the oscillations because it did not present a low enough impedance at higher frequencies. Consequently the RC bypass network was eliminated as a possible solution to the stability problem.

Another possible cause of the instability was the existence of resonant cavity modes at frequencies where the

HEMT still had gain. The formula for predicting resonant frequencies in a rectangular cavity is [53]:

$$f_{res} = \frac{1}{2\sqrt{\mu\varepsilon}} \sqrt{(m/a)^2+(n/b)^2+(p/d)^2} \qquad (4.4.2.1)$$

where m, n, and p correspond to the possible transverse electric and transverse magnetic resonant modes designated by TE_{mnp} and TM_{mnp} respectively. Here a, b, and d are the dimensions of the cavity and are 3cm, 3cm, and 1.3cm respectively (note: the cavity is taken to be the volume above the Peltier device which almost entirely encloses the RF circuitry). Table 4.4.2.1 gives some of the modes and associated resonant frequencies which could exist in the cavity and are close to the observed oscillation frequencies.

Mode	Frequency (GHz)
010	11.5
011	12.6
101	7.07
110	12.6
111	13.5
002	10.0
200	10.0

Table 4.4.2.1: Some possible resonant cavity modes in the LNA enclosure and their associated frequencies.

The resonant frequencies given in table 4.4.2.1 come very close to some of the observed oscillation frequencies. Also, an infinite number of modes could possibly exist at higher frequencies, beyond the 26GHz upper limit detectable by the spectrum analyzer. The manner in which these resonant modes contribute to the instability is by effectively increasing the extrinsic S_{12} of the HEMT.

Two methods were attempted for reducing the resonant mode effects. The first, which had little effect, was to insert lossy material at various positions in the cavity in order to damp the resonance. The other was to solder brass shields to the grounded lid of the cavity. These shields served to isolate the gate circuitry from the drain circuitry as well as to effectively decrease the size of the cavity and hence move the minimum frequencies for possible resonant modes to higher values where there is less gain and losses are higher. The shielding unfortunately had little effect on the stability other than to produce a slight shifting of the oscillation frequencies. Due to the failure of these methods in improving stability, it was presumed that another form of coupling between the input and output existed which caused the oscillations.

In the design of the HEMT carrier it was assumed that the Peltier device could electrically be considered a capacitance which would connect the refrigerator cold plate to RF ground. This may be true at lower microwave frequencies but at higher frequencies, where oscillations are present, the Peltier device most likely presents a high impedance to ground due to its physical size and inherent losses. In this case parasitic capacitances due to the HEMT carrier would not be to ground, but would couple the HEMT gate and drain to one another as illustrated in figure 4.4.2.4.

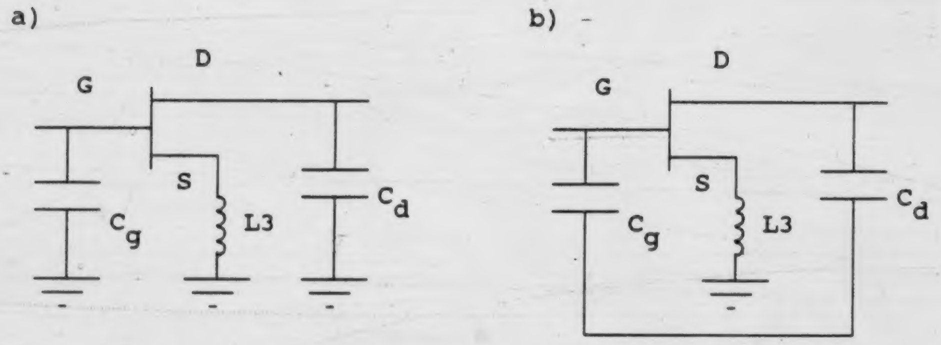

Figure 4.4.2.4: Parasitic capacitive coupling between HEMT drain and gate. a)Top of Peltier device at ground. b)Top of Peltier device floating.

The parasitic capacitances, C_g and C_d, between the pads on the HEMT carrier and the top of the Peltier device were calculated to be approximately 0.1 and 0.064pF respectively. At higher frequencies, where the top of the Peltier device is no longer at ground potential, C_g and C_d can be considered to be a series capacitive connection between the gate and drain of the HEMT with an equivalent capacitance of about 0.039pF. This capacitance is over two times the intrinsic gate to drain capacitance of the HEMT (0.039pF vs

0.016pF) shown in figure 2.4.3.1. and thus greatly increases its S_{12}.

In order to verify that this gate to drain coupling was in fact the cause of the instability, the Peltier device was removed and replaced by a strip of grounded copper tape, simulating the scenario of figure 4.4.2.4.a. The result was a stable HEMT for bias currents up to about 8mA. A small piece of Eccosorb inserted near the input of the cavity made it stable for all bias currents.

Two possible measures were available which could reduce this extrinsic gate-to-drain coupling. The first was to ground the top of the Peltier device for RF while maintaining its thermal isolation. The other possibility was to increase the impedance of the coupling path by either redesigning the HEMT carrier for lower parasitic capacitances, or by inserting some loss in the path as shown in figure 4.4.2.5. This last method of inserting loss in the feedback path required the least amount of rebuilding or redesign and thus was attempted first. The drawback of this method is that due to the added thermal resistance between the HEMT and refrigerator, the ultimate temperature achievable by the HEMT would be increased.

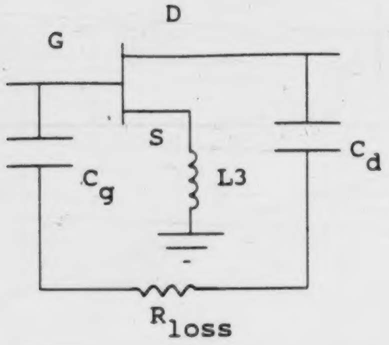

Figure 4.4.2.5: Reduction of extrinsic gate-to-drain coupling.

In order to insert loss in the feedback path, a layer of 3M® antistatic shielding was placed between the HEMT carrier and the refrigerator. This technique appeared to quell the oscillations, even without a piece of Eccosorb in the cavity. It was felt by the author that due to the high L-band impedance of this feedback path, the in-band noise performance of the LNA would not be affected. This was confirmed by a somewhat lengthy analysis of the noise performance of parallel two-port networks based on the work of Valk [52].

At this point it was decided to proceed with the development of the critical RF parameters of the LNA: noise temperature and gain. It was found that a more permanent thermally conductive connection than thermal grease could be made between the HEMT carrier, the lossy layer, and the refrigerator with the use of the alcohol based silver paint used in the previous step. The connection could be broker when desired by the application of an alcohol such as ethanol or methanol.

After further testing with this new configuration it became evident that oscillations were again present. This was probably due to there being less space between the HEMT carrier and refrigerator, thus increasing the gate-to-drain coupling. Consequently, it was necessary to develop a new method of suppressing the oscillations.

The new method of stabilization attempted was to try to force the top of the Peltier device to ground potential. This was accomplished through the use of commercially available "space blanket", a very thin mylar sheet coated with an even finer metal layer, probably aluminum. The space blanket was placed between the HEMT carrier and the top of the Peltier device and fastened to the LNA enclosure with copper tape as shown schematically in figure 4.4.2.6. This configuration detracts from the thermal design in two respects. Firstly, it creates an additional conductive heat path from the LNA enclosure to the refrigerator. Secondly, it adds thermal resistance in series with the HEMT carrier. Space blanket was chosen because its longitudinal thermal resistance should be relatively high due to its very small cross-sectional area, while the thermal resistance in series with the HEMT carrier should be very low since in its transverse direction it presents a large cross-sectional area compared to its thickness ($R_{TH} \propto L/A$).

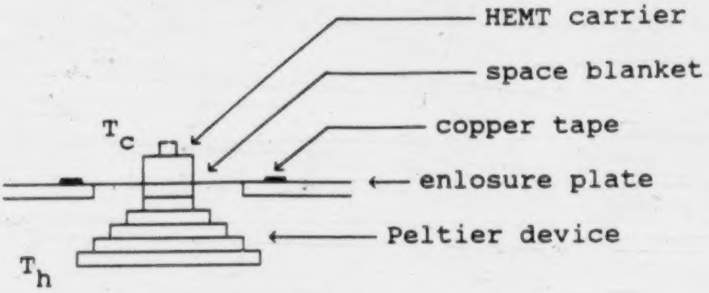

Figure 4.4.2.6: Space blanket between Peltier device and HEMT carrier.

This technique proved to be effective in eliminating room temperature oscillations. At this point it was again decided to proceed with the development of the important LNA parameters, ie. noise temperature and gain, as well as with testing of the thermal design.

The LNA was mounted on an aluminum plate with a forced convection heat sink attached as shown in figure 4.4.2.7. A roughing pump was connected to the vacuum chamber of the LNA via a hose. A thermocouple was run through the enclosure lid and fastened to the quartz HEMT carrier with silver paint. The vacuum seal was maintained with a vacuum epoxy filling the thermocouple hole. A second thermocouple was mounted on the bottom of the LNA enclosure to monitor the Peltier device hot side temperature. After pumping down the enclosure for several hours, a pressure of about 4×10^{-3} Torr was reached. This pressure should effectively eliminate the convective heat transfer in this enclosure which has dimensions at least ten times smaller than the bell jar shown in figure 3.2.3.1.

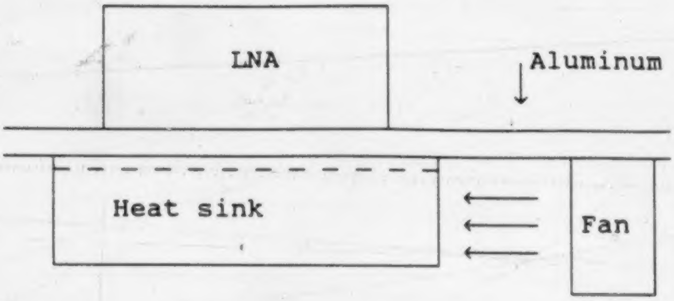

Figure 4.4.2.7: Thermal mounting of LNA

When the LNA was turned on it was determined that the thermocouple attached to the HEMT carrier had the effect of coupling in noise as well as detuning the amplifier. However, since the thermocouple was in place, it was decided to proceed with testing the thermal design.

With no power applied to the HEMT, the HEMT carrier reached a temperature of about 224K while the hot side remained at about 299K. When the HEMT was biased at 5mA and 2V (10mW), the cold temperature increased by one degree to 225K. The current to the Peltier device was varied between 3.0 and 4.0 Amps without significant change in the cold plate temperature. For this reason, subsequent operation of the Peltier device was at 3 Amps to minimize the required heat dissipation at the hot plate.

The one degree difference in HEMT carrier temperature with and without the HEMT biased can be used to roughly determine the transverse and longitudinal thermal resistances of the space blanket layer. The transverse thermal resistance (R_{st}) can be calculated using

$$R_{st} \cong \Delta(\Delta T)/\Delta Q \qquad (4.4.2.2)$$

where $\Delta(\Delta T)$ is the change in the temperature difference (1K) and ΔQ is the change in the heat flow transversely through the space blanket. The resulting R_{st} is approximately 100K/W. In order to determine the longitudinal thermal resistance of the space blanket (R_{sl}), equation 3.2.4 can be used, with $R_{car} \cong R_{st}$, to evaluate for the new R_T formed by the parallel combination of 5025K/W (original R_T) and R_{sl}. The new R_T is ~420K/W and the resulting R_{sl} is ~460K/W.

These values for R_{sl} and R_{st} show how the space blanket severely degrades the thermal design as reflected by at least a 25K increase over the expected HEMT physical temperature. An additional heat load of over 150mW flows through R_{sl} and the assumptions made in forming equation 3.2.5 are no longer valid.

At this point the thermocouple was removed from the HEMT carrier and cooling was again attempted. It was found that the HEMT oscillated at 11GHz at all but very low bias currents (≤2mA). Replacing the copper lid with one made from plexiglass alleviated this problem. The drain resistance, R2, was also reduced from 50Ω to 15Ω in order to improve stability. This solution indicated that the combination of the increased gain of the cooled HEMT and the existence of a resonant cavity mode was sufficient to force the potentially unstable circuit into oscillations.

With stability reasonably assured, the LNA was connected in the test configuration shown in figure 4.4.2.8 with the internal tuning network replaced by a 50Ω thruline. The 3dB pad was used to present the LNA with a 50Ω termination at frequencies outside the 1-2GHz bandwidth of the isolator.

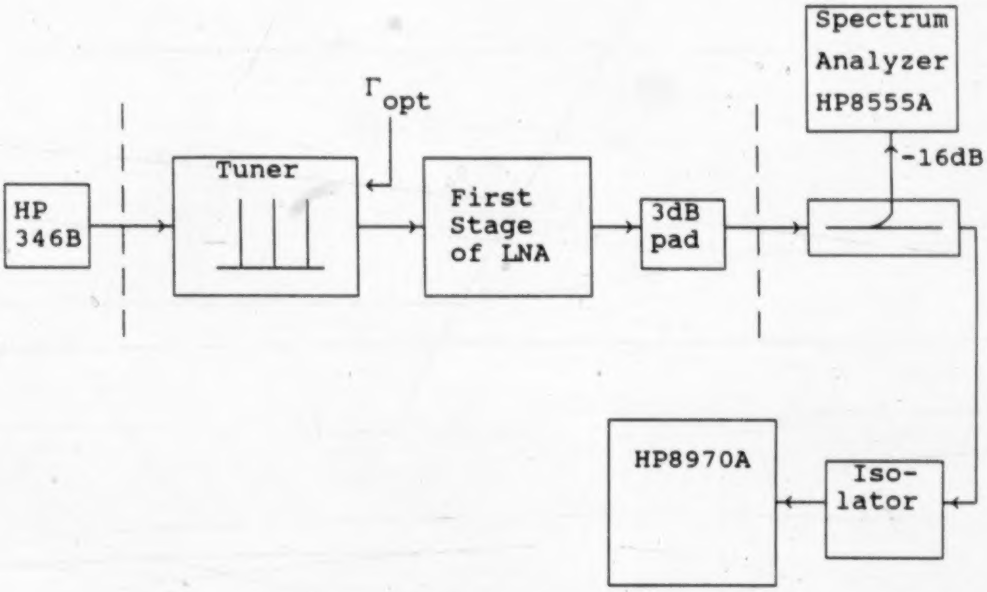
Spectrum
Analyzer
HP8555A
Γ_{opt}
-16dB
Tuner
HP
346B
First
Stage
of LNA
3dB
pad
HP8970A
Iso-
lator

Figure 4.4.2.8: Test configuration for optimizing input tuning network.

The procedure used to optimize the input tuning network entailed first locating the tuning position resulting in the minimum noise temperature and then designing a matching circuit having the same source reflection coefficient as the tuner (ie. Γ_{opt}). Γ_{opt} was determined for the HEMT both at room temperature and at about 225K, although only the cooled measurements were used for design purposes. For simplicity, the above procedure was performed only at 1420MHz.

In order to obtain accurate figures for the noise temperature, the noise contribution of the 3dB pad was taken into account using equation 2.2.8. The noise parameters of the 3dB pad were determined by a computer program based on the work of Valk [52] in the form of Γ_{opt}, T_{min}, and T_N and are $0.0\angle 0.0$, 300K, and 447K respectively. The noise temperature can be calculated from these noise parameters using the following equation [52]:

$$T_e = T_{min} + T_N \frac{|\Gamma_s - \Gamma_{opt.}|^2}{|1 + \Gamma_{opt}|^2 (1 - |\Gamma_s|^2)} \quad (4.4.2.3)$$

To properly compensate for the 3dB pad it is also necessary to know its source reflection coefficient (S_{22} of the LNA). The noise contribution of the tuner can also be calculated with knowledge of its S-parameters and source reflection coefficient. The source reflection coefficient is the output reflection coefficient of the HP346B noise source and is nominally zero (~0.01 change in magnitude between 'on' and 'off' states). Table 4.4.2.2 gives the measured S-parameters of the LNA (with HEMT cooled and at room temperature) and the tuner in various combinations including those required for accurate noise temperature determination of the LNA. Table 4.4.2.3 gives the measured and corrected gains and noise temperatures of the LNA.

DUT	Temp.	S11	S21	S12	S22
LNA+ Tuner +Pad	300K	0.543∠-14.4	2.37∠142	0.044∠124	0.283∠-2.30
	*225K	0.507∠-19.5	1.24∠141	0.017∠125	0.078∠-2.40
LNA+ Tuner	†300K	0.588∠-17.2	2.52∠-173	0.057∠166	0.489∠74.8
	225K	---	---	---	0.460∠79.5
LNA	300K	0.727∠-117	2.83∠-49.1	0.052∠-68.3	0.475∠86.4
	*225K	0.699∠-117	1.06∠-91.7	0.015∠-109	0.081∠1.50
Tuner	300K	0.294∠-132	0.918∠75.7	0.921∠75.3	0.307∠98.9
	225K	0.260∠-134	0.929∠73.6	0.933∠73.2	0.265∠96.9

HEMT biased at 2V and 7mA unless otherwise noted.

* 10dB instead of 3dB to keep ANA input power within range.

† HEMT biased at 3mA to keep ANA input power within range.

Table 4.4.2.2: 1420MHz S-parameter measurements with externally tuned LNA.

DUT	Temp.	T_e (K)	G_A (dB)
LNA+tuner +3dB pad (measured)	300K	146	7.92
	225K	107	9.37
3dB pad	300K	440	-3.83
	225K	420	-3.81
Tuner	300K	21.8	-0.315
	225K	22.5	-0.323
LNA+tuner	300K	117	11.8
	225K	86.9	13.2
LNA+tuner (-tuner noise)	300K	88.5	11.8
	225K	59.8	13.2

Table 4.4.2.3: 1420MHz noise temperatures and gains of externally tuned LNA and associated components. HEMT biased at 2V and 7mA.

The noise temperatures given in table 4.4.2.3 are not as low as expected. They do, however, reflect a substantial improvement in noise performance even with the moderate applied cooling. Also, the external tuner has a finite loss which degrades the noise performance as shown by the difference in noise temperature of the LNA+tuner before and after the noise contribution of the tuner was removed. In the hopes of reducing this degradation, an internal tuning network was designed based on the Γ_{opt} determined from the S-parameter measurement of the tuner, optimized for the cooled HEMT ($\Gamma_{opt}=S_{22}$ of the tuner).

Γ_{opt} obtained from table 4.4.2.2 ($0.265\angle 96.9$) was measured at the reference plane formed by the connector of the tuner. This reflection coefficient had to be transformed through the electrical length to the point where the internal tuning network was to be located. The resulting required reflection coefficient looking into the tuning network was approximately $0.58\angle 0^\circ$. It was possible to employ a simple LC network to realize the required source reflection coefficient. Two possible LC combinations are shown in figure 4.4.2.9. The network of figure 4.4.2.10.b) was chosen because its lower required component values made realization easier. It was then constructed in the same manner as the original one shown in figure 4.4.2.2.

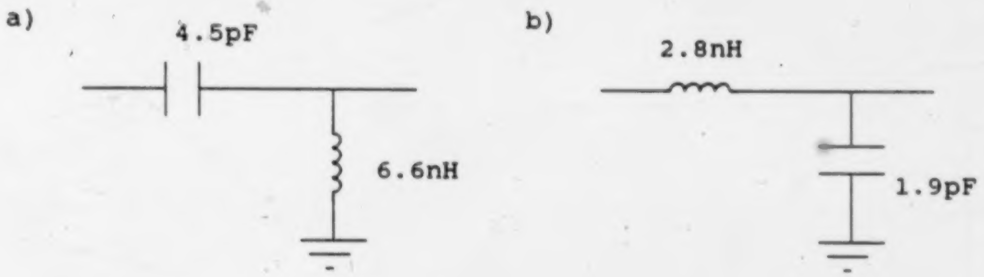

Figure 4.4.2.9: Dual realizations of input tuning network for source reflection coefficient equal to Γ_{opt}.

The LNA was then placed in the test configuration shown in figure 4.4.2.10. The L-band LNA was added to eliminate the effects of gain variation in the lengthy cable connected from the isolator to the noise figure meter. Adjustments were made to the tuning network to optimize the noise performance at 1.42GHz. S-parameter and noise temperature measurements were then performed for two bias conditions with the HEMT both at room temperature and at 225K.

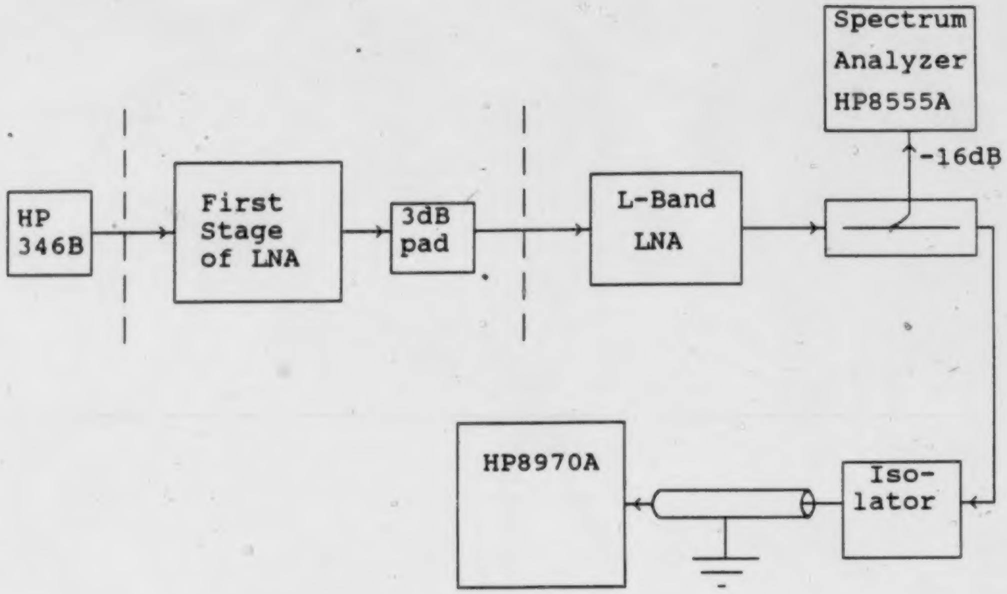
Spectrum
Analyzer
HP8555A
-16dB
HP
346B
First
Stage
of LNA
3dB
pad
L-Band
LNA
HP8970A
Iso-
lator

Figure 4.4.2.10: Test configuration for first stage of LNA with internal tuning network.

Figure 4.4.2.11 gives the resulting S-parameters of the LNA stage. Figure 4.4.2.12 gives the available gain and noise temperature of the stage with corrections made for the 3dB pad. The resulting noise temperatures are not as low as predicted. However, a marked improvement in noise temperature was achieved by cooling the HEMT. The decrease in noise temperature with cooling is nearly linear with temperature as predicted by Pospieszalski [5] and as discussed in section 1.2 earlier. Figure 4.4.2.13 gives the actual cooled noise temperatures as well as those predicted

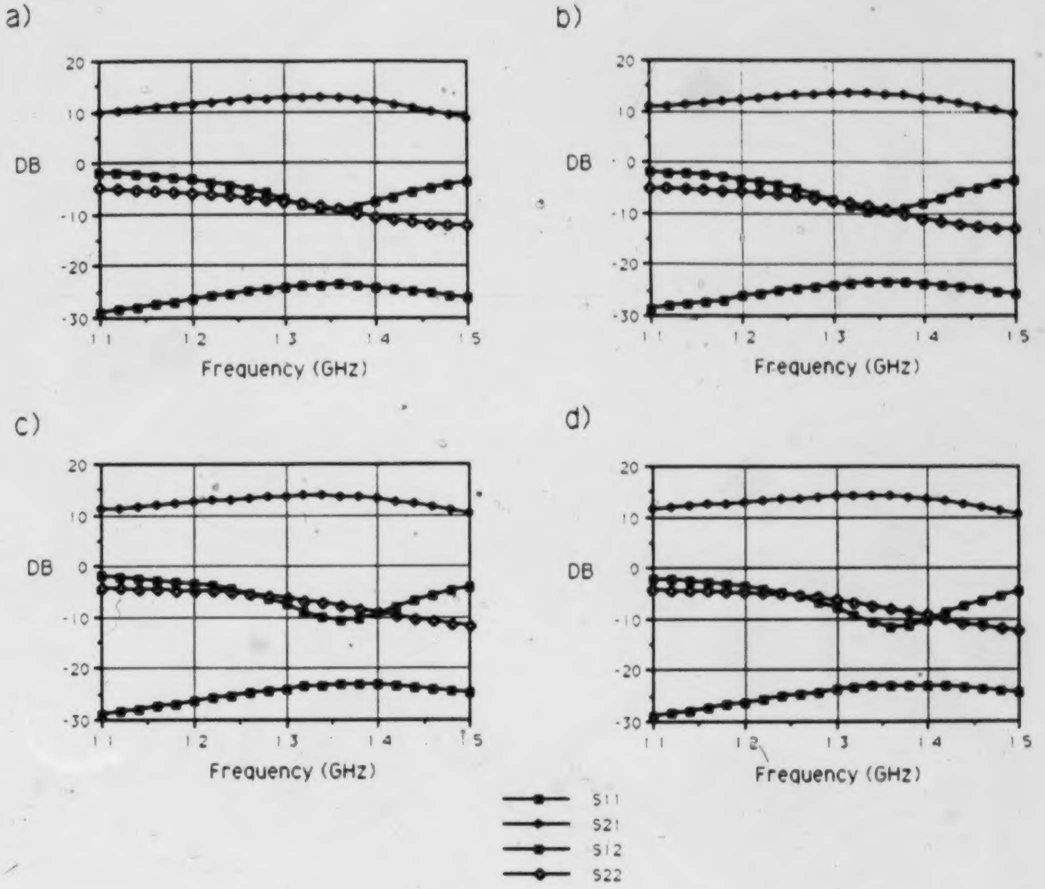

Figure 4.4.2.11: LNA S-parameters at 300K and at 225K.
a) I_d=5mA, T=300K, b) I_d=7mA, T=300K,
c) I_d=5mA, T=225K, d) I_d=7mA, T=225K.

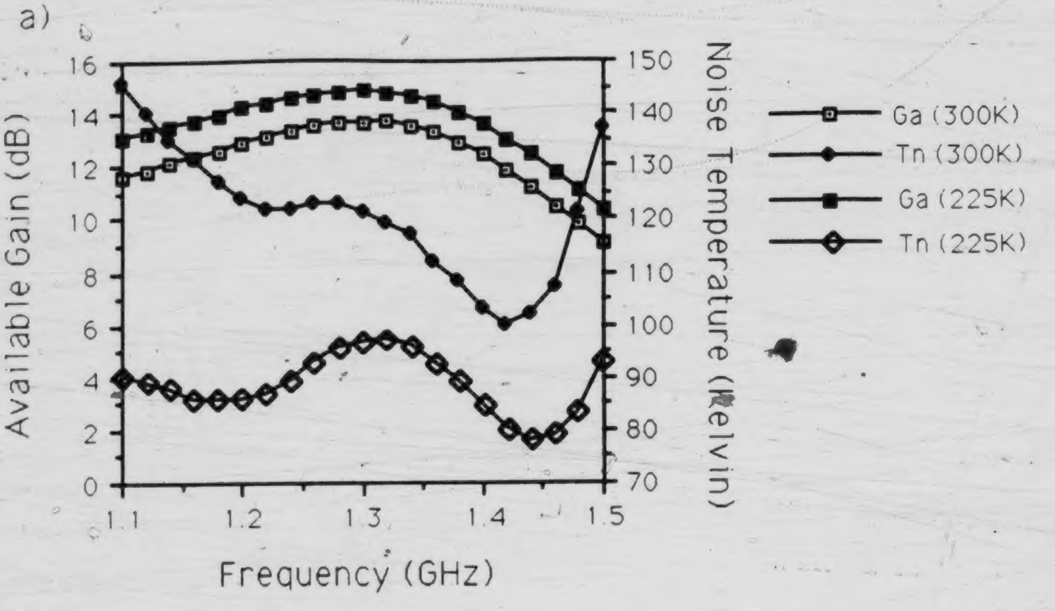

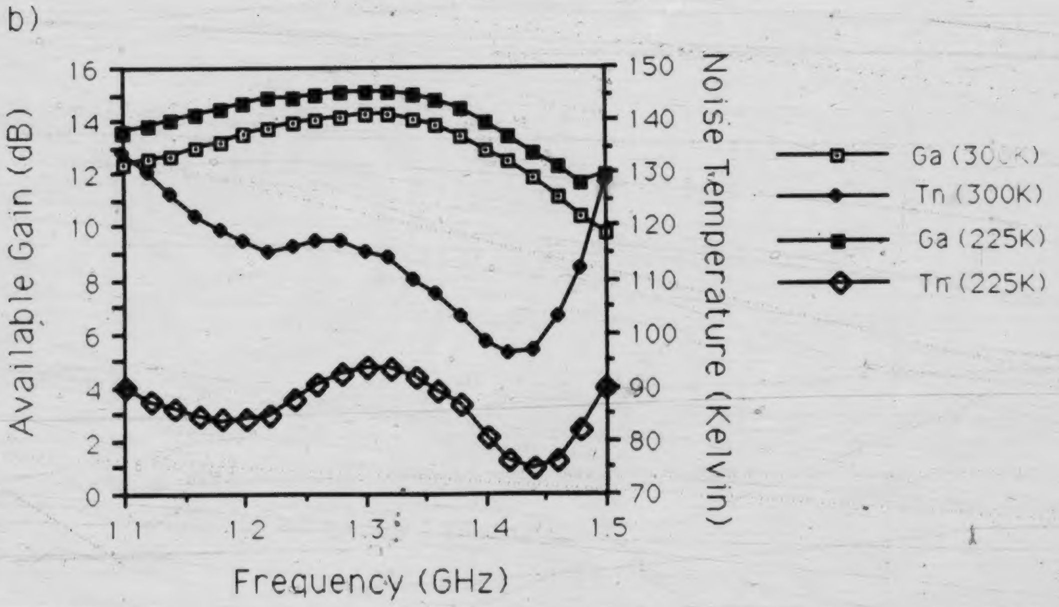

Figure 4.4.2.12: Available gain and noise temperature for LNA first stage with HEMT at 300K and 225K. a) I_d=5mA, b) I_d=7mA.

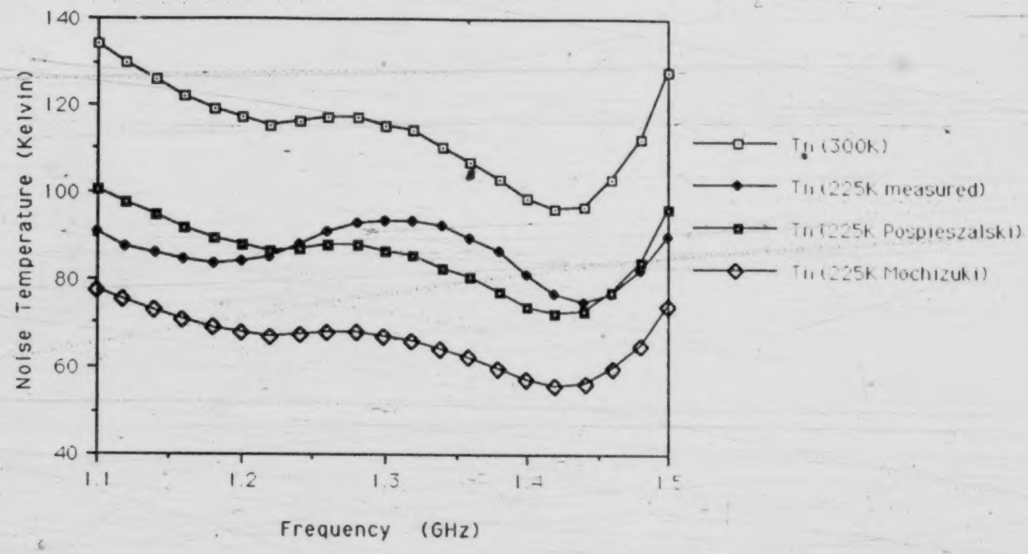

Figure 4.4.2.13: Noise temperature improvement due to cooling as measured and predicted by Pospieszalski [5] and Mochizuki [6].

by Pospieszalski and Mochizuki [6] calculated from the values of T_e measured at 300K. It appears that Mochizuki's exponential relationship between noise temperature and physical temperature is rather optimistic.

4.4.3 Discussion

Several possible factors may have resulted in the higher than predicted noise temperatures. These factors include: loss unaccounted for in circuit components, undetected oscillations, and damaged or sub-standard HEMTs (ie. HEMTs which do not meet manufacturer's specifications).

The most obvious possible cause of the higher than expected noise temperatures is loss unaccounted for in particular circuit components. It is known that the conductivity of electroplated gold is very unpredictable [54] and can vary between 10 and 74 percent of that of wrought copper. The implications of this discovery are that the gold plated manganin inductors may have a non-neglible loss component. In order to verify if indeed this was the cause of the inflated noise temperatures, individual manganin wires were replaced with pure copper wires of the same diameter. Even with all the manganin inductors replaced with copper ones, however, there was no discernible difference in the room temperature noise temperatures.

It is possible that the HEMT was oscillating at higher frequencies than are detectable by the spectrum analyzer. This is unlikely for two reasons. Firstly, the HEMT bias behaved normally as evidenced by a smooth increase in gate voltage with drain current. Secondly, the measurements were repeatable with no fluctuations beyond what is normal in noise measurements. One or both of these conditions were violated in all previous cases of detected oscillations.

The possibility that the HEMT was partially damaged was diminished by the fact that three different HEMTs were placed in the circuit without any significant difference in the results. Also, proper static precautions were taken during both construction and measurement.

None of the above factors can be ruled out completely in the higher than predicted LNA noise temperatures. Other factors unknown to the author may also have contributed.

4.5 Conclusions

This chapter provided a brief introduction to the subject of microwave noise measurement as well as the test configurations employed in this project. These measurement configurations were applied to the testing of the modified 'Walker' LNA [15] as well as to the LNA developed in this thesis.

A great deal of work was required to overcome severe LNA instability problems created by model deficiencies. Several possible causes of instability were discussed and investigated. It was found that the RF characteristics of the Peltier device had a detrimental effect on the circuit which had to be compensated for. This required modifications to the design which increased the ultimate cold temperature of the HEMT by at least 25K.

The noise temperatures obtained by the LNA were not as low as expected. Modifications to the tuning network were made which improved the LNA performance which still fell short of the predicted results. Several possible causes of the inflated noise temperatures were discussed.

The thermal design of the LNA worked satisfactorily with the HEMT reaching 224K after modifications compared to the expected ~200K before modifications. The improvement in noise performance due to cooling closely followed the relationship predicted by Pospieszalski [5]. It was demonstrated that the thermal analysis performed in chapter 3 was valid and should be of use in future projects of this nature.

Chapter 5: Future LNA Development

5.0 Introduction

It is certain that in the future, effort will continue to be expended on the improvement of LNA performance. For the benefit of those carrying on in attempts at cooling only the critical components of LNAs, this chapter will discuss the two main problems involved in the process: stability and thermal isolation. Possible methods of overcoming these problems will be explored. The use of Joule-Thompson cooling as well as the possibility of cooling multiple LNAs, or components thereof, will also be considered.

5.1 Future LNA Development With Peltier Cooling

Future LNA designs employing Peltier cooling of particular components will require that special attention be paid to stability. This will involve the development of enclosures which do not support resonant modes susceptible to amplifier oscillation, and broad-band RF characterization of the refrigerator and other circuit components.

A possible alternative to traditional L-band LNA design techniques is the use of planar passive elements in hybrid configurations. In order to simplify matching to the highly reflective inputs of L-band HEMTs, other source impedances than 50 ohms could be considered, making direct coupling to waveguide components a possibility.

5.1.1 Problems With This Project

The main difficulty with this project was the struggle to obtain a stable circuit. Instead of initially attempting a complete three stage design, more preliminary work should have been performed in the way of simplified experiments. Computer modelling proved to be of limited use because of the lack of refrigerator RF characterization, uncertainty in the manufacturer's HEMT specifications, and the many unknown parasitic elements created by the LNA enclosure itself.

Future projects of this nature should begin with the development of a single stage amplifier, in a simple enclosure. The first step should be the design of an enclosure which houses only the refrigerator and a thermally isolated HEMT with only the minimum required bias circuitry. An external tuner should be used to determine the optimum source matching condition for noise performance. With accurate knowledge of the matching requirements, more complex circuits can then be designed which meet the desired gain, bandwidth, and noise requirements. Once a single cooled stage is working satisfactorily, attention can be focused on subsequent stages. If the noise and gain performance of the first stage is adequate, it may be possible to use commercially available LNAs in place of the subsequent stages. Another possibility is simply to incorporate the single stage as a preamplifier for LNAs currently in use.

In the design of an LNA enclosure, particular attention should be paid to input/output coupling in order to improve stability. A possible solution to this problem is to build shielding directly into the cavity to isolate the drain circuitry from the gate circuitry. By essentially compartmentalizing the cavity, not only would direct coupling between components be reduced, but the effective size of the cavity would also be made smaller. This reduces the possibility of resonant cavity modes contributing to instability in the LNA.

5.1.2 Hybrid LNA Design

A possible alternative approach to traditional L-band LNA design is the incorporation of one or more complete stages in a single hybrid circuit. This technique is widely used at higher microwave frequencies where transmission line components are much smaller. However, at L-band, the size of transmission line components can be prohibitively large. If feasible, hybrid L-band LNA stages would yield several advantages when combined with Peltier or other cooling techniques, such as ease of production, the ability to cool an entire stage including the input circuit, and the availability of accurate planar component models. This section will discuss the prospect of realizing a single miniature hybrid L-band LNA stage.

Even with a high dielectric microwave circuit board such as alumina ($\varepsilon_r \cong 10$), the wavelength at 1.4GHz in a microstrip transmission line is nominally 6.6cm. The prospect of incorporating multiple transmission line components with lengths of up to $\lambda/4$ on a single miniature hybrid circuit is daunting. In addition, transmission line components are both narrow-band and frequency-periodic in nature. This makes higher frequency resonances inevitable and thus complicates the process of realizing a stable circuit. Consequently, this discussion will be limited to the realization of hybrid LNA stages employing planar lumped elements.

Models of planar passive elements used in microwave integrated circuit designs have been well documented [47]. Several types of both planar capacitors and inductors exist. For small inductances (1-3nH), the straight strips described in section 4.4.1 are normally used. Larger inductances (up to ≅ 20nH) can be formed with planar loops or spirals. Interdigitated capacitors are normally used for capacitances less than 1pF. Larger capacitors usually require metal-insulator-metal (MIM) techniques to meet size constraints. These MIM capacitors can be realized using lithographic techniques or chips.

The technology is currently available for producing these passive components in sub-millimeter dimensions on various dielectric materials. Consequently, hybrid L-band LNA stages could be produced having dimensions of the same order as the Peltier device cold plate used in this project. A possible drawback of employing hybrid circuits is the inability to tune or alter circuit components after fabrication.

5.1.3 Alternative Source Impedance

Since the advent of radar technology during the second world war, the standard impedance for microwave devices and test equipment has been 50 Ohms. However, L-band HEMTs and GaAsFETs, due to their high input reflection coefficients, require relatively high source impedances. This necessitates the use of networks to transform the 50 Ohm source to the higher required impedance. A possible alternative to this approach may be to match the cooled transistor directly to a high impedance source and thus do away with the impedance transformation network. The optimimum source reflection coefficient (Γ_{opt}) for the NE32084 HEMT is nominally $0.823\angle 10.8^{\circ}$ at 1.4GHz. In a 50 Ω system this transforms to an optimum source impedance (Z_{opt}) equal to $360\angle 38.2^{\circ}$ and requires an impedance transformation of greater than 7 to 1. However, the antenna feeds in the synthesis telescope at DRAO consist of a section of circular waveguide approximately 15cm in diameter. The impedance of these waveguide sections at 1.42GHz can be calculated using [53]

$$Z_g = \eta\sqrt{1 - (f_c/f)^2}, \qquad (5.1.3.1)$$

where Z_g is the waveguide impedance, η is the intrinsic impedance of free space (377Ω), and f_c is the waveguide cut-off frequency (1.17GHz). The impedance, Z_g, at 1.42GHz is about 214Ω, much closer to the required HEMT source impedance than 50Ω.

It may be possible to couple the LNA directly to the antenna feed by way of a high impedance transmission line. The matching circuitry would be greatly simplified as the required impedance transformation would be reduced to about 1.7 to 1 from the previous 7 to 1. This would also ease the design of broadband matching circuits.

5.2 Joule-Thompson Cooling in LNA Design

Joule-Thompson cooling is achieved through the expansion of a pressurized gas, or throttling. This effect can be magnified by precooling the incoming high pressure gas stream with the outgoing cold working fluid in a heat exchanger, a process sometimes referred to as Linde-Hampson cooling [55]. Figure 5.2.1 is the temperature-entropy diagram of this process using nitrogen as the working fluid. Room temperature nitrogen gas at 100 atmospheres enters the countercurrent heat exchanger at point A. It is cooled at almost constant pressure in the exchanger until it reaches

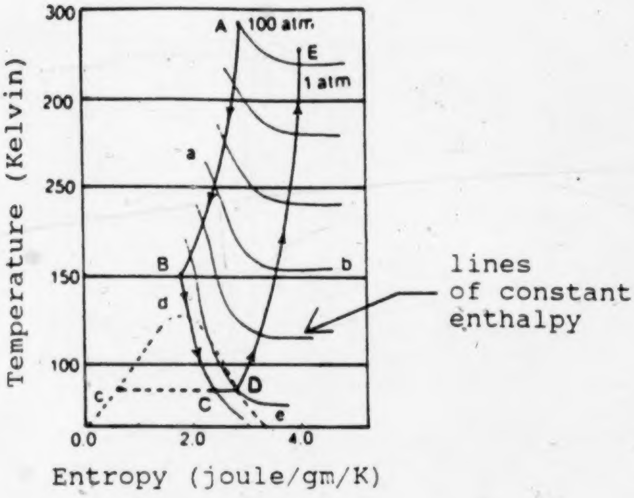

Figure 5.2.1: Temperature-entropy diagram for Joule-Thompson effect with precooling. Modified from MMR Tech. [8].

150 K at point B. The gas is then expanded adiabatically in a fine capillary resulting in Joule-Thompson cooling and forms a liquid at point C. The vapour travels back through the heat exchanger from point D to E, precooling the incoming gas until it vents at atmospheric pressure, just below ambient temperature. The refrigeration capacity of the process is determined by the change in enthalpy between points E and A.

Currently there are commercially available Joule-Thompson refrigerators specifically suited to the cooling of small electronic components [8]. These refrigerators are mass produced using semiconductor production techniques resulting in miniature packages less than 2ml in volume. These miniature cryocoolers can achieve temperatures as low as 77K with heat loads of up to 250mW. MMR Technologies specifies a nitrogen gas consumption of only about 7.5cc/sec (STP) per 100mW of heat load at 77K. This corresponds to a consumption of 6.5 litres per day of nitrogen at 100 atmospheres and ambient temperature.

The two main problems in producing practical LNAs using miniature Joule-Thompson refrigerators are packaging and sustaining a supply of clean, pressurized gas for extended periods. In order to optimize the noise performance of the LNA, there must be a low-loss electrical input connection to the outside of the vacuum package containing the refrigerator. As with the Peltier cooled HEMT LNA, the electrical connections must be designed so as not to contribute an excessive heat load. In a system containing several LNAs, supplying clean high pressure gas becomes both an engineering and an economical problem.

Little [56] describes a miniature Joule-Thompson refrigerator (1.0cm x 4.0cm x 0.1cm) cooling a CMOS clock to below 100K, all contained in a ceramic vacuum package. The clock is mounted on the alumina cold stage from which there are eight gold traces for electrical contact. Such a system could possibly be adapted to house a hybrid LNA or LNA stage constructed on alumina as discussed in section 5.1.2. The problem still remains to produce a low loss RF input with a high thermal resistance and to ensure adequate grounding while maintaining thermal isolation.

5.3 Cooling Multiple LNAs With A Single Refrigerator

The proposed new DRAO radio-telescope [17] is to consist of about 100 antennas, each observing at several frequencies. The ability to cool several LNAs, or components thereof, with a single refrigerator would result in extreme cost and maintenance benefits. Cooling only the critical components of the LNAs would enable the use of lower capacity and cheaper refrigerators such as the miniature Joule-Thompson devices or even Peltier devices if only moderate cooling is desired.

Figure 5.3.1 gives a schematic representation of how a single refrigerator could be employed to cool the critical components of several LNAs. The success of this configuration is dependent on the following factors: minimal radiative and convective heat loads, good thermal contact between refrigerator and cooled components, and thermal isolation of cooled components from LNA enclosures.

The number of LNAs possible in the configuration given in figure 5.3.1 is dependent on the heat capacity of the refrigerator and the desired cold temperature. For example, assuming no radiative or convective heat load and good thermal isolation of the cooled components, a miniature Joule-Thompson refrigerator would be able to cool at least 3 or 4 first stage transistors to 77K.

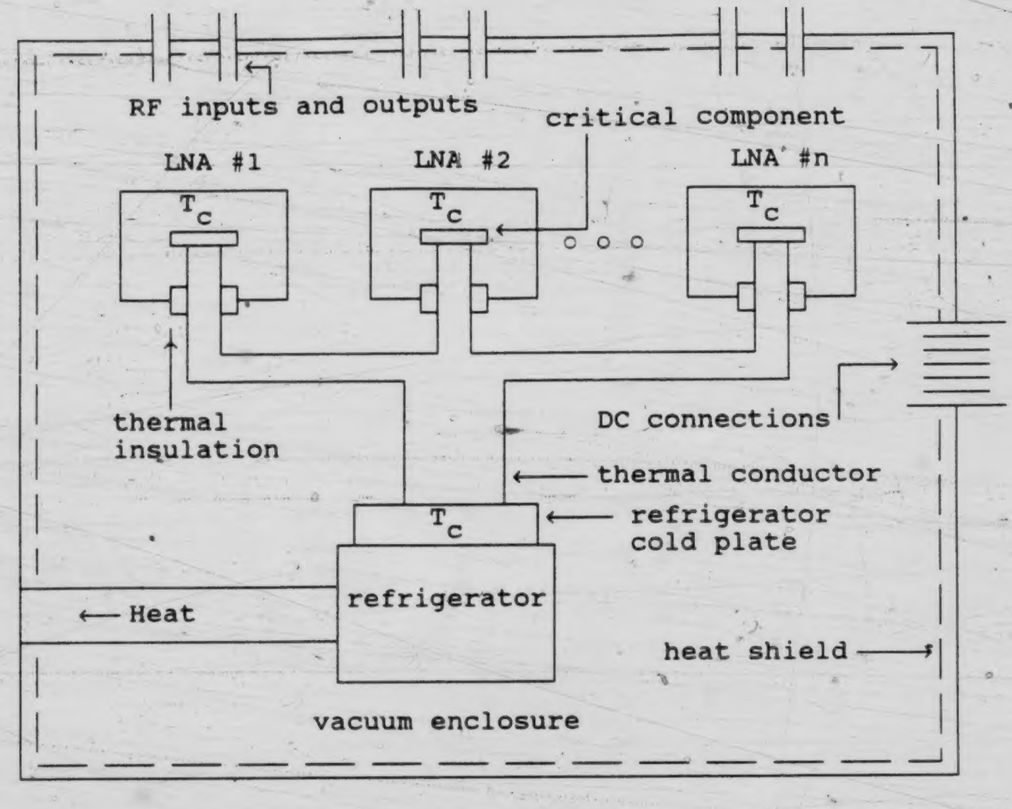
RF inputs and outputs
critical component
LNA #1
LNA #2
LNA #n
T_c
T_c
T_c
thermal insulation
DC connections
thermal conductor
T_c
refrigerator cold plate
refrigerator
Heat
heat shield
vacuum enclosure

Figure 5.3.1: Cooling of multiple LNAs with single refrigerator.

5.4 Thermal Insulation with RF Conduction

Regardless of the technique chosen for cooling only the critical components of an amplifier, the problem of providing a highly conductive RF path while maintaining thermal isolation will exist. This thesis has explored several of the options pertaining to this problem, yet many possibilities have been left for future studies. This section will briefly introduce some of these previously unexplored options for possible future investigation.

In chapter 4 it was found that having a good RF ground between the refrigerator and the active device was essential both for stability and for eliminating the parasitic effects of the refrigerator. This project utilized a small sheet of space blanket for this purpose because of its thermal properties. A very good electrically conducting metal, in the form of an extremely thin foil or mesh, would have as good or better electrical properties depending on the relative thickness and conductivity. The advantages of using a pure metal as opposed to the space blanket are an improved thermal contact with the refrigerator and the possibility of easily characterizing its thermal and electrical properties. In producing or working with a thin metal foil, optimally only a few skin depths thick, mechanical strength and workability may be the limiting factor.

Another possibility in providing a good RF ground which is thermally isolated is to capacitively couple the cooled ground plane to the ambient ground. This technique would involve the design of a structure with enough surface area to provide a very low capacitive reactance between the refrigerator and the RF grounds. Ideally the dielectric would be vacuum in order to minimize the thermal load; however, some form of spacers may be required for mechanical stability.

A third possibility for providing a thermally isolated ground is simply an extension of the space blanket concept. Evaporating a thin metallic film onto a thermal insulator is essentially the same as the space blanket except that the materials can be chosen specifically to suit the task. The quality of the evaporated metal film is the major factor in successfully implementing this method.

Producing a thermal break in the signal path can be accomplished by an endless list of capacitive structures such as the one developed in chapter 3 or by interdigitated or cylindrical structures. It may also be possible to use the same concepts mentioned for producing a thermally isolated ground to produce a thermal break in the signal path.

Although these concepts are not the only possibilities, they are the ones most obvious to the author. All future projects of this nature will have to take into account the desired cold temperature, the refrigerator heat capacity, and the particular RF design.

5.5 Conclusion

The purpose of this chapter was to serve as a guide for those involved in similar future projects. The key problem areas in cooling only the critical LNA components were discussed. Alternate RF design concepts such as hybrid circuits and non-standard source impedances were introduced as a means for possible improvement of future designs. The use of miniature Joule-Thompson refrigerators was considered as an option in achieving cryogenic temperatures without expensive closed cycle systems. The possibility of cooling the critical components of several LNAs with a single refrigerator was also discussed. Finally, the problem which forms the common thread among projects of this nature, achieving an RF conducting thermal break, was discussed.

Chapter 6: Conclusions

This thesis was primarily involved in the development of a new LNA design technique; an LNA with only the critical components thermoelectrically cooled. In the past, LNAs have either been operated at room temperature or have been bulk cooled. This project investigated the possibility of cooling only the critical components of an LNA for the purpose of producing inexpensive, self-contained, and low maintenance units. A secondary aspect of this thesis was to provide a reference and to discuss different alternatives for future projects of this nature.

Chapter 2 introduced the RF theory required to perform an LNA design. A design procedure involving a new computer program was developed to implement the design theory. The program served to assist in determining matching and feedback conditions for optimum noise performance of transistors. The chapter concluded with a preliminary 1.4GHz LNA design and its performance as predicted by Touchstone®.

The third chapter explained the three thermoelectric effects. An extensive description was given of the operation of practical thermoelectric devices, including their limitations. The remainder of the chapter dealt with integrating the RF design of chapter 2 with the thermoelectric refrigerator. This involved the use of a thermal model to determine the heat loads due to conduction, convection, and radiation. A compartmentalized LNA enclosure was designed to meet both thermal and electrical requirements. Techniques for fabricating a unique quartz HEMT carrier were also developed.

Chapter 4 presented the bulk of the laboratory work performed in this project. It began with a brief introduction to the topic of noise measurement. The measurement instruments and techniques required in the project were described. These techniques were applied to testing the modified 'Walker' LNA [15] as well as the LNA developed in this thesis.

Severe stability problems were encountered during the testing of the LNA. Several possible causes of instability were discussed and investigated. The stability problems were overcome by RF grounding the top of the Peltier device. This solution compromised the ultimate cold temperature achieved by the HEMT by at least 25K.

Although the noise temperatures obtained were not as low as predicted, substantial improvement was noted with cooling the HEMT. It was found that the improvements in noise temperature due to cooling closely followed the linear relationship predicted by Pospieszalski [5] (see section 1.2). The thermal design worked well despite compromises made for stability purposes.

The fifth chapter serves as a reference for future projects of this nature. Key problem areas in cooling only the critical LNA components were discussed. Concepts such as utilization of hybrid circuits and non-standard source impedances were introduced as means of possible improvement or simplification of future designs. Miniature Joule-Thompson refrigerators were considered as an option in achieving cryogenic temperatures without expensive closed cycle systems. A basic configuration for cooling the critical components of multiple LNAs with a single refrigerator was given. The problem of achieving a thermally isolated RF ground, a common requirement in projects of this nature, was also discussed.

In conclusion, this thesis served as a starting point in developing the concept of cooling only critical LNA components. This concept, with some refinement, is a promising alternative to traditional LNA design. The greatest benefits of using the concepts developed herein may be expected with multiple antenna telescopes, where the cost and maintenance requirements of closed-cycle refrigerators become overwhelming.

References

[1] S. Weinreb, M.W. Pospieszalski, R. Norrod, "Cryogenic, HEMT, Low-noise Receivers for 1.3 to 4.3 GHz Range", 1988 IEEE MTT-S Digest, pp.945-948.

[2] C.R. Moore, R.C. Clauss, "A Reflected-Wave Ruby Maser with K-Band Tuning Range and Large Instantaneous Bandwidth", IEEE Trans. Microwave Theory Tech., vol. MTT-27, no. 3, pp. 249-256, March 1979.

[3] S. Weinreb, M. Balister, S. Maas, P.J. Napier, "Multiband Low-Noise Receivers for a Very Large Array", IEEE Trans. Microwave Theory Tech., vol. MTT-25, no. 4, pp. 243-248, April 1977.

[4] D.R. Williams, "State-of-the-Art Cryogenically Cooled Amplifiers for Radio Astronomy", Proceedings of a Workshop held at Penticton 1989 October 11-12, Dominion Radio Astrophysical Observatory, Herzberg Institute of Astrophysics, National Research Council of Canada, June 1991.

[5] M.W. Pospieszalski, S. Weinreb, R.D. Norrod, R. Harris, "FET's and HEMT's at Cryogenic Temperatures - Their Properties and Use in Low-Noise Amplifiers", IEEE Trans. Microwave Theory Tech. vol. MTT-36, no. 3, pp. 552-560, March 1988.

[6] T. Mochizuki, K. Honma, K. Handu, W. Akinaga, K. Ohata, "Low Noise Amplifiers Using Two Dimensional Electron Gas FETs", 1985 IEEE MTT-S Digest, pp. 543-546.

[7] Marlow Industries, Inc., 10451 Vista Park Road, Dallas, TX 75238, (214) 340-4900.

[8] MMR Technologies, Inc., 897 Independence Ave., 4-B, Mountain View, CA 94043, (415) 965-9653.

[9] G.R. Busacca, P.A. Goldgeier, H.B. Goldberg, M. Noyes, A. Chuchra, "A 14-GHz Cooled Low-Noise GaAs FET Amplifier for Communication Satellite Application", RCA Review, vol. 45, pp. 651-669, December 1984.

[10] M. Uenohara, R. Wolfe, "Parametric Amplifier with Thermoelectric Refrigeration",IRE Trans. on Electron Devices, ED-8, pp. 521-524, 1961.

[11] M. Iwakuni, M. Niori, T. Saito, T. Hamabe, H. Kurihara, K. Jyoshin, M. Mikuni, "A 20 GHz Peltier-cooled Low Noise HEMT Amplifier", 1985 IEEE MTT-S Digest, pp. 551-553.

[12] R. Askew, "A Cooled Low-Noise GaAs FET Amplifier", RCA Review, vol. 44, pp. 537-550, December 1983.

[13] Berkshire Technologies, 5427 Telegraph Road, Suite B, Oakland, CA 94609, (415) 655-1986.

[14] S. Weinreb, D.L. Fenstermacher, R.W. Harris, "Ultra-Low-Noise 1.2- to 1.7-GHz Cooled GaAsFET Amplifiers", IEEE Trans. Microwave Theory Tech., vol. MTT-30, no. 6, pp. 849-853, June 1982.

[15] G. Walker, J.F. Vaneldik, D. Routledge, T.L. Landecker, J.A. Galt, "A dual-channel cooled GaAsFET receiver for the Dominion Radio Astrophysical Observatory 26-metre radio telescope covering 1.35 to 1.75 GHz", Canadian Elec. Eng. Journal, vol.13, no. 1, pp. 3-7, 1988.

[16] "The DRAO Synthesis Telescope", Dominion Radio Astrophysical Observatory, National Research Council of Canada, Box 248, Penticton, B.C., V2A 6K3, (604) 497-5321.

[17] "The Radio Schmidt Telescope", Proceedings of a Workshop held at Penticton 1989 October 11-12, Dominion Radio Astrophysical Observatory, Herzberg Institute of Astrophysics, National Research Council of Canada, June 1991, P. Dewdney, T.L. Landecker.

[18] J.D. Kraus, "Radio Astronomy", Second Edition, 1986, Cygnus-Quasar Books, Powell Ohio.

[19] H. Nyquist, "Thermal Agitation of Electric Charge in Conductors", Physics Review, vol. 32, pp. 110-113, 1928.

[20] W.N. Christiansen, J.A. Högbom, "Radiotelescopes", Second Edition, 1985, Cambridge University Press, Cambridge, U.K..

[21] M. Anderson, "Reducing Antenna Noise in a Synthesis Telescope and an Observation of an HII Region", M.Sc. Thesis, University of Alberta, 1989.

[22] H.T. Friis, "Noise Figures of Radio Receivers", Proceedings of the IRE, vol. 32, pp. 419-422, July 1944.

[23] G. Gonzalez, "Microwave Transistor Amplifiers, Analysis and Design", 1984, Prentice-Hall, Inc., Englewood Cliffs, NJ.

[24] H. Fukui, "Design of Microwave GaAs MESFET's for Broad-Band Low-Noise Amplifiers", IEEE Trans. Microwave

Theory Tech.,vol. MTT-27, pp. 643-650, July 1979.

[25] T.J. Drummond, W.T. Masselink, H. Morkoc, "Modulation-Doped GaAs/(Al,Ga)As Heterojunction Field-Effect Transistors: MODFETs", Proceedings of the IEEE, vol. 74, no. 6, pp. 773-822, June 1986.

[26] A.J. Hill, P.H. Ladbrooke, "High Electron Mobility Transistors (HEMTs) - A Review", General Electric Company Journal of Research, vol. 4, no. 1, pp. 1-14, 1986.

[27] I. Hanju, S. Asai, M. Nunokawa, K. Joshin, Y. Hirachi, S. Ohmura, Y. Aoki, T. Aigo, "Super Low-Noise HEMTs With a T-Shaped WS$_{ix}$ Gate", Electronics Letters, vol. 24, no. 21, pp. 1327-1328, October 1988.

[28] H. Morkoc, P.M. Solomon, "The HEMT: A Superfast Transistor", IEEE Spectrum, pp. 28-35, February 1984.

[29] Nippon Electric Company, Distributed by California Eastern Laboratories, 3260 Jay Street, Santa Clara, CA 95054, (408) 988-3500.

[30] C.C. Lo, B. Leskovar, "Cryogenically Cooled Broad-Band GaAs Field-Effect Transistor Amplifier", IEEE Trans. Nuclear Science, NS-31, pp. 474-479, 1984.

[31] H.G. Jackson, T.T. Shimizu, "A Low-Noise 2-4 GHz Preamplifier", Nuclear Instruments and Methods in Physics Research, no. 226, pp. 560-563, 1984.

[32] S. DePanfilis, J. Rogers, "L- and S-Band Low-Noise Cryogenic GaAs FET Amplifiers", IEEE Trans. Microwave Theory Tech., vol. MTT-36, no. 3, pp. 607-610, March 1988.

[33] A. Anastassiou, M.J.O. Strutt, "Effect of Source Lead Inductance on the Noise Figure of a GaAs FET", Proceedings of the IEEE, pp. 406-408, March 1974.

[34] G.D. Vendelin, "Feedback Effects on the Noise Performance of GaAs MESFETs", 1975 IEEE MTT-S Digest, pp. 324-326.

[35] B.M. Albinsson, "A Graphic Design Method for Matched Low-Noise Amplifiers", IEEE Trans Microwave Theory Tech., vol. MTT-38, no. 2, pp. 118-122, February 1990.

[36] H.J. Goldsmid, "Thermoelectric Refrigeration", Plenum Press, New York, 1964.

[37] M.N. Özisik, "Heat Transfer: A Basic Approach",

McGraw-Hill, U.S.A., 1985.

[38] R. Wolfe, "The Physics of Thermoelectricity", Semiconductor Products, vol. 6, pp. 23-28, April 1963.

[39] J.E. McCormick, J.B. Brauer, "The Feasibility of Solid-State Cryogenic Refrigeration to 70°K", Advances in Cryogenic Refrigeration, vol. 10A, pp. 493-504, Plenum Press, 1965.

[40] R. Marlow, P.B. Click, "Estimating Heat Loads on Multistage Thermoelectric Heat Pumps", SPIE, vol. 116, Solid State Imaging Devices, 1977, pp. 94-103.

[41] Y.S. Touloukian, C.Y. Ho, "Thermal Conductivity (Nonmetallic Solids)", Thermophysical Properties of Matter, The TPRC Data Series, vol. 2, IFI/Plenum, New York, 1970.

[42] R.K. Hoffman, "Handbook of Microwave Integrated Circuits", Artech House, Inc., Norwood, MA, 1987.

[43] Valpey Fisher, A subsidiary of Matec, 75 South Street, Hopkington, MA 01748.

[44] C.R. Paul, S.A. Nasar, "Introduction to Electromagnetic Fields", McGraw-Hill, U.S.A., 1982.

[45] S. Weinreb, "Low-Noise Cooled GASFET Amplifiers", IEEE Trans. Microwave Theory Tech., vol. MTT-28, no. 10, pp. 1041-1054, October 1980.

[46] A. Tslaf, "Physical Sciences Data 9: Combined Properties of Conductors", Elsevier Scientific Publishing Company, Holland, 1981.

[47] I. Bahl, P. Bhartia, "Microwave Solid State Circuit Design", John Wiley and Sons, Inc., U.S.A., 1988.

[48] H.A. Wheeler, "Simple Inductance Formulas for Radio Coils", Proceedings of the IRE, vol. 16, no. 10, pp. 1398-1400, October 1928.

[49] A. Roth, "Vacuum Technology", North Holland Publishing Company, Holland, 1976.

[50] "Fundamentals of RF and Microwave Noise Figure Measurements", Hewlett Packard, Application Note 57-1.

[51] M.C. Chau, "Microprocessor-Controlled ANA System for De-Embedding FET Parameters", M.Sc. Thesis, University of Alberta, 1984.

[52] E.C. Valk, "Techniques of Microwave Noise Measurements on Cooled Transistors". Ph.D Thesis, University of Alberta, 1990.

[53] S.Y. Liao, "Microwave Devices and Circuits", Prentice-Hall, Inc., NJ, 1985.

[54] A.M. Fowler, "Radio Frequency Performance of Electroplated Finishes", Proceedings I.R.E.E. Australia, pp. 148-164, May 1970.

[55] G. Walker, "Miniature Refrigerators for Cryogenic Sensors and Cold Electronics", Monongraphs in Cryogenics 6, Oxford Science Publications, New York, 1989.

[56] W.A. Little, "Integrated Cryogenic Chip Carrier for High-Speed CMOS and Superconducting Devices", presented at Low Temperature Electronics Symposium, Stanford University, CA, Oct. 1987.

Appendix 1.1

LNA Design Program Listing

```
C *** UPDATED JUNE 8.1989---GAVIN MILLER
C  THIS PROGRAM PRODUCES VALUES OF GAMMA(L) ALONG A
C  CONSTANT OPERATING GAIN CIRCLE (CGC) AND THE CORRESPONDING
C  VALUES OF GAMMA(S) REQUIRED FOR A CONJUGATE MATCH.  IT
C  PERFORMS THESE COMPUTATIONS FOR AN INCREMENTAL SOURCE
C  FEEDBACK INDUCTANCE. LS.
C
      COMPLEX X(2.2).GAMOPT(4).GAMS(1100).GAML(100).Z(2.2)
      COMPLEX SS(2.2.4).S(2.2).ZOPT.GAMOPS
      REAL F(4).LS.ALS.LSTA.LSTP.GP.LSN.PI.FMIN.NF(100).TN
      INTEGER IL.INC.M.IF
      PI=3.14159265
C
C  READ IN THE NUMBER OF FREQUENCIES FOR WHICH THERE IS DATA
C
      READ(5.99)IF
C
C  READ IN S PARAMETERS
C
      DO 10 I=1.IF
        DO 11 J=1.2
          DO 12 K=1.2
          READ(5.100)X(J.K)
          CALL PTOR(X)
          SS(J.K.I)=X(J.K)
12        CONTINUE
11      CONTINUE
10    CONTINUE
C
C  READ IN GAMMA(OPT)s. Rn (NORMALIZED). AND FMIN(DB)
C
      READ(5.110)(GAMOPT(I).I=1.IF)
     READ(5.111)FMIN.RN
C
C  CONVERT GAMMA(OPT) TO RECTANGULAR COORDS.
C
      DO 15 I=1.IF
      GAMOPT(I)=CMPLX(REAL(GAMOPT(I))*COS(AIMAG(GAMOPT(I))
     +*PI/180.).REAL(GAMOPT(I))*SIN(AIMAG(GAMOPT(I))*PI/180.))
15    CONTINUE
C
C  READ IN START VALUE OF LS(nH). STOP VALUE AND # OF INCREMENTS
C
      READ(5.120)LSTA.LSTP.IL
C
C  READ IN 4 FREQUENCIES (GHz)
C
      READ(5.130)(F(I).I=1.IF)
C
C  READ IN DESIRED OPERATING GAIN (dB)
C
      READ(5.140)GAIN
C
C  READ IN THE # OF DESIRED GAMMAs FOR EACH LS
C
      READ(5.150)INC
C
C  FORMAT STATEMENTS FOR INPUT
C
99    FORMAT(I1)
```

```
100    FORMAT(F5.3,1X,F5.1)
110    FORMAT(F5.3,1X,F5.1)
111    FORMAT(F4.2,1X,F4.2)
120    FORMAT(F4.1,1X,F4.1,1X,I2)
130    FORMAT(F5.2,1X,F5.2,1X,F5.2,1X,F5.2)
140    FORMAT(F5.2)
150    FORMAT(I2)
C
C  BEGIN LOOPS FOR INCREMENTAL LS
C
       ALS=(LSTP-LSTA)/(IL-1)
       LS=(LSTA-ALS)*1E-9
       DO 20 I=1,IL
         LS=LS+ALS*1E-9
         LSN=LS*1E9
         WRITE(2.800)LSN
800      FORMAT(2X,'LS=',F10.5,'nH')
C
         DO 21 J=1,IF
C
C  PRINT FREQUENCY
C
         WRITE(2,810)F(J)
C
C  CALCULATE NEW GAMMA(OPT) AND PRINT IT.
C
       ZOPT=(1+GAMOPT(J))/(1-GAMOPT(J))
       ZOPT=ZOPT-CMPLX(0,1)*2*PI*LS*F(J)*1E9/50
       GAMOPS=(ZOPT-1)/(ZOPT+1)
C
C  CONVERT GAMOPS TO POLAR COORDINATES.
C
             GAMOPS=CMPLX(CABS(GAMOPS),
    +ATAN2(AIMAG(GAMOPS),REAL(GAMOPS))*180/PI)
C
C  PRINT RESULTING GAMMA(OPT)
C
       WRITE(2,812)GAMOPS
812    FORMAT(5X,'GAMMA(OPT)=',F9.7,1X,'@ ',F9.4,' DEGREES')
C
C  WRITE TABLE HEADINGS.
C
         WRITE(2,815)
815   FORMAT(3X,'N',4X,'|GAML|',5X,'ANG(L)',4X,'|GAMS|',4X
    +,'ANG(S)',4X,'TN')
810      FORMAT(5X,'FREQUENCY= ',F6.3,' GHz')
C
C  CONVERT S PARAMETERS TO Z PARAMETERS. ADD EFFECT OF LS
C  AND CONVERT BACK TO S PARAMETERS
C
           DO 22 K=1,2
             DO 23 L=1,2
               S(K,L)=SS(K,L,J)
23           CONTINUE
22         CONTINUE
         CALL STOZ(S,Z)
           DO 25 K=1,2
             DO 26 L=1,2
               Z(K,L)=Z(K,L)+CMPLX(0,2.*PI*LS*F(J)*1.E9/50)
26           CONTINUE
```

```
25          CONTINUE
          CALL ZTOS(Z.S)
C
C   COMPUTE VALUES OF GAMMA(L) ALONG CGC AND THE
C   CORRESPONDING GAMMA(S)s FOR A CONJUGATE MATCH
C
            CALL GAMSUB(S.GAIN.INC.GAML.GAMS)
C
C   CALCULATE THE NOISE FIGURES FOR EACH GAMS
C
.      CALL NOFIG(GAMS.GAMOPS.FMIN.RN.NF.INC)
C
            DO 24 M=1.INC
C
C   CALCULATE THE NOISE TEMPERATURE
C
       TN=(NF(M)-1)*290
C
C   PRINT RESULTS AT LS.F
C
            WRITE(2.820)M.GAML(M).GAMS(M).TN
24          CONTINUE
21        CONTINUE
20      CONTINUE
C
820     FORMAT(2X.I2.2X.F9.6.1X.F9.4.2X.F9.6.1X.F9.4.2X.F6.2)
        STOP
        END
C
C   THIS IS A SET OF FORTRAN SUBROUTINES TO CONVERT
C   BETWEEN VARIOUS SETS OF MICROWAVE PARAMETERS
C
       SUBROUTINE STOZ(S.Z)
       COMPLEX S(2.2).Z(2.2).DEN
       DEN=(1-S(1,1))*(1-S(2.2))-S(1.2)*S(2.1)
       Z(1.1)=((1+S(1,1))*(1-S(2.2))-S(1.2)*S(2.1))/DEN
       Z(1,2)=2*S(1.2)/DEN
       Z(2,1)=2*S(2.1)/DEN
       Z(2.2)=((1-S(1,1))*(1+S(2.2))+S(1,2)*S(2,1))/DEN
       RETURN
       END
C
C
C
C
       SUBROUTINE ZTOS(Z,S)
       COMPLEX Z(2.2).S(2.2).DEN
       DEN=(Z(1,1)+1)*(Z(2.2)+1)-Z(1,2)*Z(2,1)
       S(1,1)=((Z(1,1)-1)*(Z(2.2)+1)-Z(1,2)*Z(2,1))/DEN
       S(1,2)=2*Z(1,2)/DEN
       S(2,1)=2*Z(2,1)/DEN
     , S(2.2)=((Z(1,1)+1)*(Z(2.2)-1)-Z(1,2)*Z(2,1))/DEN
       RETURN
```

```
      END
C
C
C
C
C  MISCELLANEOUS ROUTINES WHICH MAY BE USEFULL ELSEWHERE
C
C
C  SUBROUTINE PTOR CONVERTS A 2X2 COMPLEX ARRAY OF THE FORM
C  X(I.J)=MAGNITUDE.ANGLE(DEG) TO RECTANGULAR COMPONENTS.  THIS
C  IS USEFUL FOR INPUTTING DATA IN POLAR FORM. AND CONVERTING THIS
C  TO THE FORM REQUIRED TO USE THE FORTRAN COMPLEX FUNCTIONS.
C  INCLUDING MOST OF THE ROUTINES IN THIS FILE.
C
      SUBROUTINE PTOR(X)
      COMPLEX X(2.2).CMPLX
      RADFCT=180/(4*ATAN(1.0))
      DO 10 I=1.2
        DO 20 J=1.2
          X(I.J)=CMPLX((REAL(X(I.J))*COS(AIMAG(X(I.J))/RADFCT)).
     +                 (REAL(X(I.J))*SIN(AIMAG(X(I.J))/RADFCT)))
20        CONTINUE
10      CONTINUE
      RETURN
      END
C  GAVIN MILLER   MAY 7.1989
C  (** UPDATED JUNE 21. 1989)
C  THIS SUBROUTINE COMPUTES A SPECIFIED # OF SOURCE REFLECTION
C  COEFFICIENTS ALONG A CONSTANT OPERATING POWER
C  GAIN CIRCLE.  THE INPUTS TO THE PROGRAM ARE THE
C  TRANSISTOR 'S' PARAMETERS.  THE DESIRED OPERATING
C  GAIN OF THE TRANSISTOR. AND THE NUMBER OF DESIRED
C  SOURCE REFLECTION COEFFICIENTS (GAMMAS) OBTAINED
C  FROM THE CORRESPONDING LOAD REFLECTION COEFFICIENTS
C  EVENLY SPACED ALONG THE GAIN CIRCLE.
C
C  VARIABLE DECLARATIONS
C
       SUBROUTINE GAMSUB(S.GAIN.INC.GAML.GAMS)
       COMPLEX S11.S12.S21.S22.CP.GAML(100).GAMS(100).DELTA.C2
       COMPLEX S(2.2)
       INTEGER INC
       REAL MS11.MS12.MS21.MS22.SS.D.XXX
       REAL RP.K.X.Y.GAIN.GP.MDELTA.ALPHA.XP.YP.MSG
       REAL MGAML(100).AGAML(100).MGAMS(100).AGAMS(100)
       PI=3.1415926
C
C  CONVERT S(2.2) TO S11.S12.S21.S22
C
       S11=S(1.1)
       S12=S(1.2)
       S21=S(2.1)
       S22=S(2.2)
       MS11=CABS(S11)
       MS12=CABS(S12)
       MS21=CABS(S21)
       MS22=CABS(S22)
C
C  CALCULATE 'K' AND 'DELTA' USED IN STABILITY CALCULATIONS.
C
```

```
      SS=CABS(S21*S12)
      DELTA=S11*S22-S21*S12
      MDELTA=CABS(DELTA)
      K=(1.-MS11**2-MS22**2+MDELTA**2)/SS/2
C   MSG=MAXIMUM STABLE GAIN
      MSG=MS21/MS12
      GP=10**(GAIN/10)/MS21**2
C
C  MAKE SURE THE DESIRED GAIN IS NOT GREATER THAN MSG
C
      IF((GP*MS21**2) GT MSG)GOTO 500
C
C  CALCULATE RADIUS OF CONSTANT OPERATING GAIN CIRCLE (CGC)
C   -ENSURE RADIUS IS POSITIVE (IE  CIRCLE EXISTS)
C
      D=1+GP*(MS22**2-MDELTA**2)
      XXX=1.-2*K*SS*GP+(SS*GP)**2
      IF(XXX.LT.0)GOTO 520
      RP=XXX**0.5/D
C
C  CALCULATE CENTRE OF CGC
C
      C2=S22-DELTA*CONJG(S11)
      CP=GP*CONJG(C2)/(1+GP*(MS22**2-MDELTA**2))
      XP=REAL(CP)
      YP=AIMAG(CP)
C
C  DETERMINE IF CGC LIES ENTIRELY OUTSIDE SMITH CHART
C
      IF((CABS(CP)-RP).GE.1)GOTO 510
C
C  MOVE ALONG THE CGC AND COMPUTE THE CORRESPONDING VALUES OF
C  GAMMAS REQUIRED FOR A CONJUGATE MATCH AT THE INPUT.
C
      ALPHA=-2*PI/INC
      DO 10 J=1,INC
      ALPHA=ALPHA+2*PI/INC
      X=XP+RP*COS(ALPHA)
      Y=YP+RP*SIN(ALPHA)
C
C  ENSURE NEW GAML IS INSIDE S.C  PERIMETER
C
      GAML(J)=CMPLX(X,Y)
      IF(CABS(GAML(J)).GT.1)THEN
         AGAMS(J)=0
         MGAMS(J)=0
         MGAML(J)=CABS(GAML(J))
         AGAML(J)=ATAN2(Y,X)*360/2/PI
         GOTO 9
      END IF
C
C  DETERMINE NEW GAMMAS
C
      GAMS(J)=CONJG(S11+S12*S21*GAML(J)/(1-S22*GAML(J)))
      MGAML(J)=CABS(GAML(J))
      MGAMS(J)=CABS(GAMS(J))
      AGAML(J)=ATAN2(Y,X)*360/2/PI
      X=REAL(GAMS(J))
      Y=AIMAG(GAMS(J))
      AGAMS(J)=ATAN2(Y,X)*360/2/PI
```

```
9      GAML(J)=CMPLX(MGAML(J),AGAML(J))
       GAMS(J)=CMPLX(MGAMS(J),AGAMS(J))
10     CONTINUE
       GOTO 810
500    WRITE(2,720)
       GOTO 800
510    WRITE(2,730)
       GOTO 800
520    WRITE(2,740)
       GOTO 800
C
C  OUTPUT FORMATTING
C
720    FORMAT(1X,'THE SPECIFIED GAIN IS GREATER THAN THE MSG')
730    FORMAT(1X,'THE CGC LIES ENTIRELY OUTSIDE THE SMITH CHART')
740    FORMAT(1X,'THE CGC HAS A NEGATIVE RADIUS, DOES NOT EXIST')
810    RETURN
800    STOP
       END
C
C  THIS SUBROUTINE CALCULATES THE NOISE FIGURE FOR FOR AN
C  AMPLIFIER STAGE GIVEN THE SOURCE REFLECTION
C  COEFFICIENT AND GAMMA(OPT) FOR A NOISE MATCH,
C  BOTH IN POLAR COORDINATES(MAG,ANGLE IN DEGREES),
C  AS WELL AS THE NORMALIZED NOISE RESISTANCE, Rn
C
      SUBROUTINE NOFIG(GAMS,GAMOPS,FMIN,RN,NF,INC)
C
C  VARIABLE DECLARATION
C
      COMPLEX GAMS(100),GAMOPS,GMS(100),GAMPS
      INTEGER INC
      REAL RN,NF(100),FMIN,FM
       PI=3.141592654
C
C  CONVERT GAMS AND GAMOPS FROM POLAR TO RECTANGULAR COORDINATES
C
      DO 10 J=1,INC
        GMS(J)=CMPLX(REAL(GAMS(J))*COS(AIMAG(GAMS(J))*PI/180)
     +,REAL(GAMS(J))*SIN(AIMAG(GAMS(J))*PI/180))
10    CONTINUE
C
C  CONVERT GAMOPS TO RECTANULAR COORDINATES
C
        GAMPS=CMPLX(REAL(GAMOPS)*COS(AIMAG(GAMOPS)
     +*PI/180),REAL(GAMOPS)*SIN(AIMAG(GAMOPS)*PI/180))
C
C CONVERT FMIN TO NORMAL FORM FROM LOGARITHMIC FORM
C
      FM=10**(FMIN/10 )
C
C  CALCULATE THE ACTUAL NOISE FIGURES FOR THE ARRAY OF GAMS's
C
      DO 20 J=1,INC
        NF(J)=FM+4*RN*CABS(GMS(J)-GAMPS)**2/(1-
     +CABS(GMS(J))**2)/CABS(1+GAMPS)**2
20      CONTINUE
      RETURN
      END
```

Appendix 1.2

LNA Design Program Output Data

```
DATA FOR NE32084 HEMT WITH A GAIN OF 15 DB.

 LS=    0.00000nH
    FREQUENCY=   1.400 GHz
    GAMMA(OPT)=0.8240004 @    20.4000 DEGREES
  N      |GAML|       ANG(L)      |GAMS|      ANG(S)      TN
  1     0.956127     12.3957    0.882398    30.9422     27.51
  2     0.990703     22.4448    0.972065    32.3485    106.20
  3     1.019050     32.2435    0.000000     0.0000    164.01
  4     1.040482     41.8603    0.000000     0.0000    164.01
  5     1.054503     51.3552    0.000000     0.0000    164.01
  6     1.060806     60.7831    0.000000     0.0000    164.01
  7     1.059251     70.1957    0.000000     0.0000    164.01
  8     1.049871     79.6438    0.000000     0.0000    164.01
  9     1.032874     89.1801    0.000000     0.0000    164.01
 10     1.008641     98.8612    0.000000     0.0000    164.01
 11     0.977740    108.7501    0.995166    20.2468    649.29
 12     0.940938    118.9194    0.988837    20.0916    276.09
 13     0.899228    129.4532    0.983035    19.9713    178.99
 14     0.853857    140.4508    0.977612    19.8770    133.97
 15     0.806363    152.0256    0.972444    19.8029    107.74
 16     0.758622    164.3028    0.967424    19.7453     90.36
 17     0.712876    177.4073    0.962456    19.7022     77.86
 18     0.671730   -168.5634    0.957446    19.6727     68.32
 19     0.638030   -153.5850    0.952298    19.6568     60.70
 20     0.614577   -137.7637    0.946905    19.6561     54.40
 21     0.603634   -121.3767    0.941144    19.6737     49.05
 22     0.606359   -104.8474    0.934861    19.7151     44.40
 23     0.622456    -88.6398    0.927864    19.7895     40.30
 24     0.650271    -73.1283    0.919897    19.9129     36.64
 25     0.687259    -58.5208    0.910629    20.1128     33.38
 26     0.730554    -44.8652    0.899638    20.4397     30.51
 27     0.777380    -32.1016    0.886479    20.9897     28.09
 28     0.825271    -20.1172    0.871058    21.9535     26.23
 29     0.872130     -8.7850    0.855296    23.7062     25.09
 30     0.916221      2.0165    0.849189    26.8122     24.81
 LS=    0.50000nH
    FREQUENCY=   1.400 GHz
    GAMMA(OPT)=0.8189888 @    20.6281 DEGREES
  N      |GAML|       ANG(L)      |GAMS|      ANG(S)      TN
  1     0.952540     12.2536    0.890079    28.9630     29.37
  2     0.977504     20.3818    0.948256    28.7218     58.62
  3     0.993046     28.4230    0.987178    26.6091    253.98
  4     0.998936     36.4205    0.998580    24.3656    ******
  5     0.995086     44.4139    0.995316    22.6995    712.49
  6     0.981554     52.4426    0.987132    21.5739    253.03
  7     0.958539     60.5486    0.978095    20.8178    145.18
  8     0.926387     68.7802    0.969536    20.2988    102.47
  9     0.885600     77.1956    0.961771    19.9324     80.57
 10     0.836844     85.8697    0.954776    19.6671     67.48
 11     0.780978     94.9024    0.948435    19.4708     58.84
```

```
12   0.719091   104.4322   0.942614   19.3236   52.70
13   0.652581   114.6577   0.937189   19.2127   48.09
14   0.583288   125.8694   0.932053   19.1298   44.48
15   0.513733   138.4953   0.927108   19.0695   41.55
16   0.447535   153.1447   0.922268   19.0287   39.10
17   0.390006   170.5705   0.917451   19.0058   37.01
18   0.348537  -168.6934   0.912576   19.0007   35.17
19   0.331280  -145.2685   0.907558   19.0146   33.54
20   0.342670  -121.5354   0.902307   19.0506   32.07
21   0.379698  -100.1242   0.896715   19.1140   30.72
22   0.434536   -82.0274   0.890663   19.2133   29.48
23   0.499424   -66.8598   0.884008   19.3627   28.34
24   0.568622   -53.8664   0.876590   19.5848   27.30
25   0.638208   -42.3991   0.868256   19.9174   26.38
26   0.705472   -31.9947   0.858946   20.4243   25.60
27   0.768457   -22.3380   0.848965   21.2142   25.00
28   0.825685   -13.2142   0.839763   22.4618   24.64
29   0.876010    -4.4742   0.835950   24.3815   24.54
30   0.918530     3.9886   0.848465   26.9236   24.98
LS=    1.00000nH
   FREQUENCY=   1.400 GHz
   GAMMA(OPT)=0.8137944 @    20.8574 DEGREES
 N     |GAML|      ANG(L)     |GAMS|     ANG(S)      TN
 1   0.948714    12.1960   0.896315   27.2622   31.54
 2   0.967183    18.7934   0.938452   26.2372   51.43
 3   0.975156    25.3746   0.962244   24.3275   86.22
 4   0.972545    31.9526   0.968253   22.5041  103.77
 5   0.959379    38.5401   0.964626   21.1094   92.44
 6   0.935805    45.1507   0.957270   20.1181   75.54
 7   0.902092    51.7999   0.949000   19.4232   62.60
 8   0.858620    58.5076   0.940919   18.9318   53.66
 9   0.805887    65.2998   0.933374   18.5792   47.43
10   0.744501    72.2134   0.926416   18.3228   42.95
11   0.675183    79.3040   0.919988   18.1348   39.61
12   0.598770    86.6599   0.913996   17.9973   37.03
13   0.516234    94.4336   0.908344   17.8985   34.97
14   0.428729   102.9111   0.902941   17.8306   33.29
15   0.337747   112.6992   0.897700   17.7890   31.88
16   0.245640   125.3209   0.892543   17.7711   30.68
17   0.157972   145.5939   0.887393   17.7763   29.64
18   0.097299  -169.9128   0.882173   17.8054   28.72
19   0.120634  -109.3188   0.876806   17.8613   27.91
20   0.199972   -79.9539   0.871210   17.9494   27.18
21   0.290971   -64.4904   0.865297   18.0779   26.53
22   0.382918   -53.5647   0.858980   18.2601   25.96
23   0.472406   -44.5331   0.852180   18.5164   25.46
24   0.557621   -36.4518   0.844858   18.8783   25.04
25   0.637270   -28.9091   0.837101   19.3951   24.72
26   0.710297   -21.6980   0.829314   20.1420   24.50
27   0.775802   -14.7033   0.822695   21.2253   24.39
28   0.833005    -7.8550   0.820189   22.7564   24.36
29   0.881242    -1.1083   0.827791   24.7102   24.47
30   0.919958     5.5678   0.853333   26.5761   25.54
LS=    1.50000nH
   FREQUENCY=   1.400 GHz
   GAMMA(OPT)=0.8084090 @    21.0878 DEGREES
 N     |GAML|      ANG(L)     |GAMS|     ANG(S)      TN
 1   0.944338    12.2033   0.901268   25.7443   33.95
 2   0.958182    17.5410   0.933505   24.4243   49.81
 3   0.961652    22.8907   0.950016   22.6637   67.39
```

```
  4   0.954710    28.2380   0.953531   21.0567   72.89
  5   0.937435    33.5685   0.949798   19.7969   67.08
  6   0.910022    38.8661   0.942921   18.8648   58.48
  7   0.872785    44.1116   0.935049   18.1860   51.04
  8   0.826152    49.2805   0.927139   17.6909   45.35
  9   0.770663    54.3394   0.919560   17.3274   41.08
 10   0.706972    59.2395   0.912412   17.0592   37.85
 11   0.635849    63.9064   0.905682   16.8616   35.36
 12   0.558194    68.2179   0.899311   16.7177   33.38
 13   0.475068    71.9576   0.893222   16.6167   31.79
 14   0.387798    74.7034   0.887339   16.5512   30.47
 15   0.298266    75.5159   0.881584   16.5170   29.37
 16   0.210003    71.9045   0.875884   16.5123   28.43
 17   0.133279    55.9634   0.870165   16.5370   27.63
 18   0.105357    13.8230   0.864355   16.5936   26.93
 19   0.156214   -19.6291   0.858381   16.6867   26.32
 20   0.238936   -29.9006   0.852174   16.8241   25.80
 21   0.328228   -31.5639   0.845669   17.0180   25.36
 22   0.417276   -29.9432   0.838820   17.2867   24.99
 23   0.503335   -26.7973   0.831633   17.6575   24.70
 24   0.584767   -22.8336   0.824231   18.1708   24.50
 25   0.660352   -18.3855   0.817002   18.8845   24.39
 26   0.729088   -13.6302   0.810903   19.8750   24.34
 27   0.790122    -8.6704   0.808018   21.2183   24.34
 28   0.842724    -3.5704   0.812271   22.9122   24.35
 29   0.886277     1.6273   0.829149   24.6898   24.63
 30   0.920278     6.8926   0.861374   25.8666   26.61
LS=   2.00000nH
   FREQUENCY=  1.400 GHz
   GAMMA(OPT)=0.8028258 @   21.3188 DEGREES
  N    |GAML|     ANG(L)    |GAMS|     ANG(S)     TN
  1   0.939002    12.2664   0.904972   24.3474   36.48
  2   0.949396    16.5352   0.930123   23.0128   49.64
  3   0.950240    20.8244   0.942707   21.4433   61.36
  4   0.941523    25.0994   0.945386   20.0179   64.62
  5   0.923364    29.3241   0.942199   18.8646   60.77
  6   0.896016    33.4586   0.936131   17.9767   54.60
  7   0.859865    37.4553   0.928900   17.3049   48.74
  8   0.815443    41.2540   0.921371   16.7987   43.93
  9   0.763437    44.7744   0.913937   16.4167   40.12
 10   0.704713    47.9049   0.906749   16.1288   37.13
 11   0.640366    50.4834   0.899839   15.9131   34.75
 12   0.571809    52.2653   0.893183   15.7546   32.84
 13   0.500941    52.8701   0.886731   15.6431   31.28
 14   0.430488    51.6956   0.880423   15.5720   29.98
 15   0.364648    47.8164   0.874195   15.5378   28.89
 16   0.310119    40.0382   0.867980   15.5391   27.96
 17   0.276670    27.7439   0.861713   15.5771   27.18
 18   0.273757    12.9141   0.855331   15.6556   26.50
 19   0.302379    -0.0733   0.848774   15.7811   25.93
 20   0.353973    -8.6471   0.841992   15.9643   25.45
 21   0.418394   -13.1249   0.834957   16.2208   25.06
 22   0.488395   -14.6957   0.827691   16.5739   24.75
 23   0.559419   -14.3559   0.820318   17.0562   24.54
 24   0.628530   -12.7489   0.813169   17.7131   24.41
 25   0.693741   -10.2901   0.806987   18.6016   24.35
 26   0.753544    -7.2432   0.803261   19.7784   24.34
 27   0.806803    -3.7823   0.804655   21.2556   24.34
 28   0.852617    -0.0261   0.815027   22.8980   24.43
 29   0.890268     3.9405   0.837638   24.3011   25.19
```

```
30    0.919201    8.0544    0.870702    24.8813    28.35
LS=    2.50000nH
   FREQUENCY=   1.400 GHz
   GAMMA(OPT)=0.7970382 @    21.5500 DEGREES
 N      |GAML|      ANG(L)     |GAMS|      ANG(S)      TN
 1    0.932019    12.3860    0.907303    23.0206    38.91
 2    0.939715    15.7163    0.926770    21.8394    49.62
 3    0.939132    19.0669    0.936873    20.5140    58.23
 4    0.930278    22.3906    0.939484    19.2884    60.98
 5    0.913310    25.6386    0.937266    18.2580    58.63
 6    0.888531    28.7572    0.932343    17.4311    54.02
 7    0.856404    31.6841    0.926074    16.7812    49.12
 8    0.817561    34.3440    0.919236    16.2750    44.75
 9    0.772827    36.6421    0.912236    15.8828    41.10
10    0.723261    38.4568    0.905271    15.5805    38.09
11    0.670209    39.6293    0.898418    15.3505    35.63
12    0.615397    39.9531    0.891693    15.1798    33.61
13    0.561059    39.1678    0.885074    15.0597    31.92
14    0.510093    36.9729    0.878527    14.9846    30.51
15    0.466178    33.0949    0.872003    14.9517    29.31
16    0.433638    27.4529    0.865455    14.9607    28.29
17    0.416696    20.4053    0.858832    15.0140    27.42
18    0.418009    12.8608    0.852092    15.1166    26.68
19    0.437358     5.9674    0.845200    15.2770    26.06
20    0.471768     0.5644    0.838147    15.5082    25.54
21    0.516925    -3.0652    0.830969    15.8284    25.13
22    0.568569    -5.0435    0.823790    16.2630    24.81
23    0.623132    -5.6553    0.816894    16.8454    24.59
24    0.677818    -5.1977    0.810851    17.6156    24.46
25    0.730474    -3.9237    0.806722    18.6125    24.40
26    0.779435    -2.0324    0.806279    19.8479    24.39
27    0.823398     0.3233    0.812062    21.2535    24.48
28    0.861343     3.0259    0.826652    22.6083    24.93
29    0.892471     5.9839    0.850569    23.5347    26.53
30    0.916176     9.1242    0.879908    23.6847    30.79
LS=    3.00000nH
   FREQUENCY=   1.400 GHz
   GAMMA(OPT)=0.7910389 @    21.7810 DEGREES
 N      |GAML|      ANG(L)     |GAMS|      ANG(S)      TN
 1    0.921983    12.5767    0.907882    21.7042    40.91
 2    0.927447    15.0447    0.922302    20.7845    48.95
 3    0.926245    17.5290    0.930438    19.7578    55.21
 4    0.918103    19.9787    0.933245    18.7743    57.77
 5    0.904098    22.3412    0.932227    17.9076    56.82
 6    0.883660    24.5605    0.928743    17.1787    53.78
 7    0.857583    26.5745    0.923790    16.5819    49.98
 8    0.826533    28.3124    0.918018    16.1008    46.22
 9    0.791370    29.6931    0.911825    15.7178    42.80
10    0.753168    30.6226    0.905438    15.4169    39.84
11    0.713249    30.9950    0.898979    15.1852    37.30
12    0.673209    30.6965    0.892502    15.0133    35.14
13    0.634939    29.6174    0.886025    14.8943    33.29
14    0.600602    27.6774    0.879544    14.8243    31.72
15    0.572530    24.8652    0.873041    14.8016    30.37
16    0.552983    21.2874    0.866497    14.8271    29.21
17    0.543768    17.1978    0.859894    14.9041    28.22
18    0.545813    12.9742    0.853226    15.0389    27.37
19    0.558908     9.0304    0.846511    15.2407    26.66
20    0.581764     5.7068    0.839810    15.5229    26.06
21    0.612362     3.2034    0.833254    15.9028    25.58
```

```
22    0.648378    1.5791    0.827096    16.4020    25.22
23    0.687521    0.7924    0.821782    17.0440    24.96
24    0.727719    0.7487    0.818051    17.8488    24.81
25    0.767189    1.3345    0.817023    18.8181    24.77
26    0.804436    2.4379    0.820197    19.9105    24.89
27    0.838230    3.9573    0.829125    21.0096    25.33
28    0.867579    5.8033    0.844562    21.9131    26.47
29    0.891694    7.8988    0.865313    22.3898    29.02
30    0.909973   10.1765    0.887878    22.3036    33.79
LS=    3.50000nH
    FREQUENCY=   1.400 GHz
    GAMMA(OPT)=0.7848200 @    22.0111 DEGREES
 N     |GAML|      ANG(L)      |GAMS|      ANG(S)      TN
 1    0.904945   12.8951    0.905592    20.2766    41.76
 2    0.908371   14.4972    0.914914    19.7032    46.66
 3    0.907167   16.1100    0.920891    19.0455    50.52
 4    0.901369   17.6887    0.923729    18.3789    52.59
 5    0.891142   19.1877    0.923973    17.7527    52.78
 6    0.876790   20.5603    0.922251    17.1931    51.49
 7    0.858751   21.7580    0.919123    16.7097    49.31
 8    0.837604   22.7304    0.915031    16.3029    46.73
 9    0.814070   23.4261    0.910298    15.9682    44.08
10    0.789013   23.7941    0.905147    15.6997    41.55
11    0.763432   23.7872    0.899728    15.4916    39.23
12    0.738450   23.3673    0.894138    15.3392    37.14
13    0.715277   22.5132    0.888439    15.2389    35.29
14    0.695153   21.2299    0.882674    15.1891    33.65
15    0.679264   19.5583    0.876873    15.1896    32.22
16    0.668626   17.5804    0.871067    15.2418    30.96
17    0.663964   15.4173    0.865295    15.3493    29.88
18    0.665607   13.2170    0.859615    15.5173    28.94
19    0.673439   11.1329    0.854121    15.7525    28.15
20    0.686914    9.3011    0.848957    16.0635    27.50
21    0.705141    7.8235    0.844345    16.4588    26.99
22    0.727002    6.7603    0.840609    16.9456    26.62
23    0.751269    6.1329    0.838202    17.5254    26.40
24    0.776708    5.9313    0.837711    18.1881    26.35
25    0.802150    6.1244    0.839806    18.9034    26.54
26    0.826533    6.6687    0.845096    19.6129    27.07
27    0.848927    7.5145    0.853855    20.2303    28.12
28    0.868541    8.6102    0.865711    20.6568    29.95
29    0.884730    9.9048    0.879475    20.8133    32.84
30    0.896987   11.3489    0.893368    20.6739    36.88
LS=    4.00000nH
    FREQUENCY=   1.400 GHz
    GAMMA(OPT)=0.7783750 @    22.2398 DEGREES
 N     |GAML|      ANG(L)      |GAMS|      ANG(S)      TN
 1    0.841416   13.9925    0.891566    17.7201    37.86
 2    0.841727   14.1421    0.892340    17.6861    38.13
 3    0.841581   14.2929    0.892978    17.6426    38.37
 4    0.840983   14.4384    0.893454    17.5917    38.54
 5    0.839958   14.5726    0.893750    17.5360    38.66
 6    0.838550   14.6897    0.893857    17.4781    38.70
 7    0.836819   14.7847    0.893775    17.4206    38.66
 8    0.834839   14.8534    0.893512    17.3658    38.57
 9    0.832694   14.8925    0.893085    17.3161    38.41
10    0.830477   14.9002    0.892513    17.2732    38.20
11    0.828286   14.8760    0.891823    17.2387    37.95
12    0.826216   14.8205    0.891044    17.2139    37.67
13    0.824360   14.7361    0.890205    17.1997    37.38
```

14	0.822799	14.6263	0.889341	17.1965	37.08
15	0.821605	14.4960	0.888484	17.2044	36.80
16	0.820830	14.3509	0.887667	17.2233	36.53
17	0.820511	14.1975	0.886923	17.2525	36.29
18	0.820661	14.0429	0.886281	17.2910	36.09
19	0.821274	13.8941	0.885771	17.3375	35.93
20	0.822322	13.7577	0.885416	17.3902	35.82
21	0.823757	13.6399	0.885234	17.4470	35.76
22	0.825516	13.5458	0.885240	17.5055	35.76
23	0.827519	13.4795	0.885437	17.5632	35.82
24	0.829677	13.4438	0.885821	17.6172	35.94
25	0.831896	13.4399	0.886379	17.6651	36.12
26	0.834077	13.4679	0.887088	17.7044	36.34
27	0.836128	13.5262	0.887915	17.7329	36.61
28	0.837958	13.6120	0.888822	17.7493	36.91
29	0.839491	13.7217	0.889763	17.7526	37.23
30	0.840660	13.8504	0.890694	17.7426	37.55

Appendix 2.1

Procedure for Etching Gold Pattern on Quartz

1. Clean gold surface with acetone and rinse with deionized water.
2. Coat gold surface with HPR504 photoresist (2-3ml with #18 needle) using Solitec spinner (Acceleration=700, spread 3 seconds @ 400rpm, spin 15 seconds @ 3500rpm).
3. Soft bake at 105°C in vacuum for 50 seconds. Backfill with N_2 gas.
4. Expose using positive artwork (200W uv lamp, ~11 seconds).
5. Develop:

-prewet	5 seconds @ 400rpm
-develop	50 seconds @ 400rpm
-rinse	90 seconds @ 400rpm
-spin	15 seconds @ 3500rpm

6. Etch gold using Aqua-regia ($3HCl+1HNO_3$) then etch chromium using chromium etchant.
7. Re-do #2 to prevent pattern lift-off during cutting and hard bake at 120°C for 60 seconds.